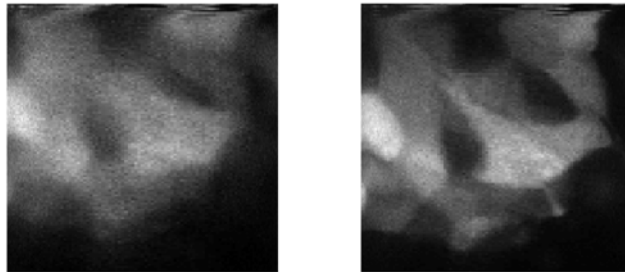


Dissertation
submitted to the
Combined Faculties for the Natural Sciences and for Mathematics
of Ruperto-Carola University of Heidelberg, Germany
for the degree of
Doctor of Natural Sciences

presented by
Dipl.-Phys. Rückel, Markus
born in Bad Neustadt a. d. Saale
Oral examination: 29. November 2006

**Adaptive wavefront correction
in two-photon microscopy
using
Coherence-Gated Wavefront Sensing**



Referees:

Prof. Dr. Winfried Denk

Prof. Dr. Josef Bille

In biologischen Proben kann mit der Zwei-Photonen Mikroskopie sehr häufig nicht das beugungsbegrenzte Auflösungsvermögen erreicht werden, da Inhomogenitäten im Brechungsindex der Proben die Wellenfront verzerren. In dieser Doktorarbeit wird gezeigt, dass mit Hilfe der adaptiven Optik - in diesem Fall der auf „Coherence-Gated Wavefront Sensing“ (CGWS) basierenden Wellenfrontkorrektur - das Auflösungsvermögen und das Fluoreszenzsignal eines Zwei-Photonen Mikroskops in verschiedenen Proben, wie z.B. in lebenden Zebrafischen, erheblich gesteigert werden kann. Der Vorteil von CGWS ist, dass zurückgestreutes Licht an Stelle von Fluoreszenzlicht benutzt wird, um die Wellenfrontaberrationen zu bestimmen. So werden die Fluoreszenzfarbstoffe nicht geschädigt oder gebleicht und Aberrationen können bis zu einer Tiefe von mehreren Streulängen gemessen werden. Weiterhin kann die Wellenfront in weniger als 1 μs mit einer Genauigkeit von $\lambda/50$ korrigiert werden, sogar in stark streuenden Proben.

Ein weiterer Teil der Arbeit beschäftigt sich mit der Abhängigkeit der Wellenfrontmessung mit CGWS von der Kohärenzlänge, Polarisation des Lichts, Streudichte und Position des Kohärenzvolumens. Ein realistisches Model für CGWS zeigt, dass für alle experimentell möglichen Parameter der Speckle-Kontrast beim CGWS voll entwickelt ist. Daher kann die über Speckle gemittelte Wellenfront als die inkohärente Überlagerung von sphärischen Wellen, die vom Kohärenzvolumen ausgehen und durch die Probe verzerrt werden, interpretiert werden.

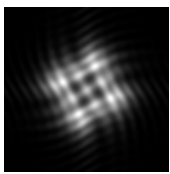
The focus of a two-photon microscope is often degraded by inhomogeneities in the refractive index within biological specimens. In this dissertation it is shown for various specimens, even for living zebrafish, that the resolution and the fluorescence signal of a two-photon microscope can be substantially improved by using adaptive optics, i.e. wavefront correction based on coherence-gated wavefront sensing (CGWS). The advantage of using CGWS relies on the fact that the wavefront distortions are sensed by backscattered instead of fluorescent light. Thus, neither photodamage nor photobleaching occurs and wavefront distortions can be sensed up to several scattering lengths deep within the specimen. Fast wavefront correction can be realized, allowing the measurement of a wavefront in less than 1 μs with an accuracy of $\lambda/50$, even in strongly scattering samples.

Furthermore, CGWS is thoroughly investigated for all relevant parameters affecting the measurement process, such as coherence length, polarization of the light, density of scatterers, and coherence-gate position. A realistic model of CGWS shows that for all experimentally accessible parameters the speckle contrast is fully developed. Thus, the ensemble-averaged wavefront is the incoherent superposition of spherical wavelets that originate from scatterers located within the coherence volume and then propagate through specimen-induced distortions.

This thesis was carried out at the Max Planck Institute for Medical Research in Heidelberg, Germany, in the department of Biomedical Optics under the supervision of Prof. Dr. Winfried Denk. I have conducted the experiments and prepared the dissertation myself; all of the resources used (literature, equipment) are specified.

Parts of this dissertation have been published in:

1. Feierabend, M., Rueckel, M., and Denk, W. (2004). "**Coherence-gated wavefront sensing in strongly scattering samples**", Optics Letters **29**(19): 2255-2257.
2. Lauterbach, M. A., Rueckel, M., and Denk, W. (2006). "**Light-efficient, quantum-limited interferometric wavefront estimation by virtual mode sensing**", Optics Express **14**(9): 3700-3714.
3. Rueckel, M. and Denk, W. (2005). **Polarization Effects in Coherence-gated Wave-front Sensing**. Adaptive Optics: Analysis and Methods/Computational Optical Sensing and Imaging/Information Photonics/Signal Recovery and Synthesis Topical Meetings on CD-ROM (The Optical Society of America, Washington, DC, 2005), AThC4.
4. Rueckel, M. and Denk, W. (2006). "**Coherence-gated wavefront sensing using a virtual Shack-Hartmann sensor**", Advanced Wavefront Control: Methods, Devices, and Applications IV, San Diego, Proceedings of SPIE.
5. Rueckel, M., Mack-Bucher, J., and Denk, W. (2006). "**Adaptive wavefront correction in two-photon microscopy using coherence-gated wavefront sensing**", submitted.
6. Rueckel, M. and Denk, W. "**Theoretical considerations to coherence-gated wavefront sensing**", in preparation.

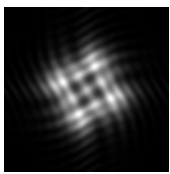


| | | |
|----------|---|-----------|
| 1 | Introduction | 3 |
| 1.1 | Motivation | 3 |
| 1.2 | Two-photon microscopy | 9 |
| 1.3 | Shack-Hartmann sensor | 11 |
| 1.3.1 | Real Shack-Hartmann sensor | 11 |
| 1.3.2 | Virtual Shack-Hartmann sensor | 13 |
| 2 | Coherence-gated wavefront sensing | 17 |
| 2.1 | The principle of CGWS | 17 |
| 2.2 | Implementation of CGWS | 23 |
| 2.2.1 | Experimental implementation | 23 |
| 2.2.2 | Monte-Carlo Simulation | 27 |
| 2.3 | Characterization of vSHS | 30 |
| 2.3.1 | Noise-free characterization | 30 |
| 2.3.2 | Photon-noise | 31 |
| 2.4 | Characterization of the CGWS | 36 |
| 2.4.1 | Coherence volume | 36 |
| 2.4.2 | Speckle characterization | 37 |
| 2.4.3 | Speckle averaging | 48 |
| 2.5 | CGWS-measured wavefront aberrations | 51 |
| 2.5.1 | Influence of the speckle contrast on the measurement of aberrations... 51 | |
| 2.5.2 | Aberrations due to a tilted glass-plate | 54 |
| 2.5.3 | Aberrations close to focus | 58 |
| 2.6 | Polarization effects on CGWS | 60 |
| 2.7 | Discussion | 68 |
| 3 | Wavefront correction using CGWS | 71 |
| 3.1 | Characterization of the deformable mirror (DM) | 71 |
| 3.2 | Principle of wavefront correction | 75 |
| 3.3 | Fluorescence measurements in uniformly fluorescent samples | 78 |
| 3.4 | Correction of glass-capillary induced distortions | 81 |
| 3.5 | Correction of zebrafish-induced distortions | 85 |
| 3.6 | Discussion | 88 |
| 4 | Summary and outlook | 91 |

| | | |
|-------------------|--|------------|
| Appendix A | Zernike polynomials | 94 |
| Appendix B | Computer-controlled setup | 95 |
| Appendix C | Propagation of polarized light in the sample arm..... | 98 |
| Appendix D | Glass capillary induced astigmatism..... | 103 |
| 5 | Literature | 105 |

Abbreviations

| | |
|------|--|
| CG | Coherence-gate |
| CGWS | Coherence-gated wavefront sensing/sensor |
| CV | Coherence volume |
| DM | Deformable mirror |
| MCS | Monte-Carlo simulation |
| OCT | Optical coherence tomography |
| PSI | Phase shifting interferometry |
| SHS | Shack-Hartmann sensor |
| vSHS | virtual Shack-Hartmann sensor |



1 Introduction

1.1 Motivation

With the invention of the first compound microscopes and telescopes at the end of the 16th century, the demand for aberration-corrected high-quality lenses arose. As it was not possible at this time to manufacture high-quality lenses, the compound microscopes were outperformed for a long time by the single-lens microscope manufactured by Antoni van Leeuwenhoek (1632-1723), who could produce lenses with an unparalleled grinding technique. Only in the mid-1800s the collaborative work of the optical technician Carl Zeiss (1816-1888) and the physicist Ernst Abbe (1840-1905) set new standards for optical equipment [Gerth, 2005]. Since Zeiss found his method of trial and error for the manufacture of high-quality microscopes unsatisfactory, Abbe made extensive calculations for the lens design and, thus, paved the way for microscopes with a minimum of chromatic and monochromatic aberrations. At the same time, Philipp Ludwig von Seidel (1821-1896) studied the theory of departures from Gaussian optics (first-order approximation to geometrical optics) and expanded the first-order monochromatic aberrations into five constituent aberrations (the so-called Seidel aberrations): spherical aberration, coma, astigmatism, field curvature, and distortion [Born et al., 1999].

As the optical quality of telescopes improved, astronomers became aware of the limitations imposed on the resolution by the dynamically varying refractive-index inhomogeneities of the atmosphere. The first to perceive the importance of the atmospheric conditions on telescopic images was Christiaan Huygens (1629-1695). Some good advice on where to place telescopes was given by Isaac Newton (1642-1727), who wrote: “The only Remedy is a most serene and quiet Air, such as may perhaps be found on the tops of the highest Mountains above the grosser Clouds” (cited from *Opticks*, 1704). The possibility of compensating atmospheric turbulence was not conceivable in Newton’s time [Hardy, 1998].

More than 200 years later Horace W. Babcock suggested the first method to neutralize aberrations due to the turbulent atmosphere by using a wavefront sensor in combination with a wavefront corrector (Fig. 1.1a, [Babcock, 1953; Born et al.,

1999]). Since fast and light-sensitive wavefront sensors were not available at this time the first experimental realization revealed the full potential of this type of adaptive optics as recently as 1978 [Hardy, 1978]. At the same time a different approach to adaptive optics was pursued, relying on the optimization of the image sharpness function by applying trial phase perturbations to the wavefront corrector (Fig. 1.1b, [Buffington et al., 1977]).

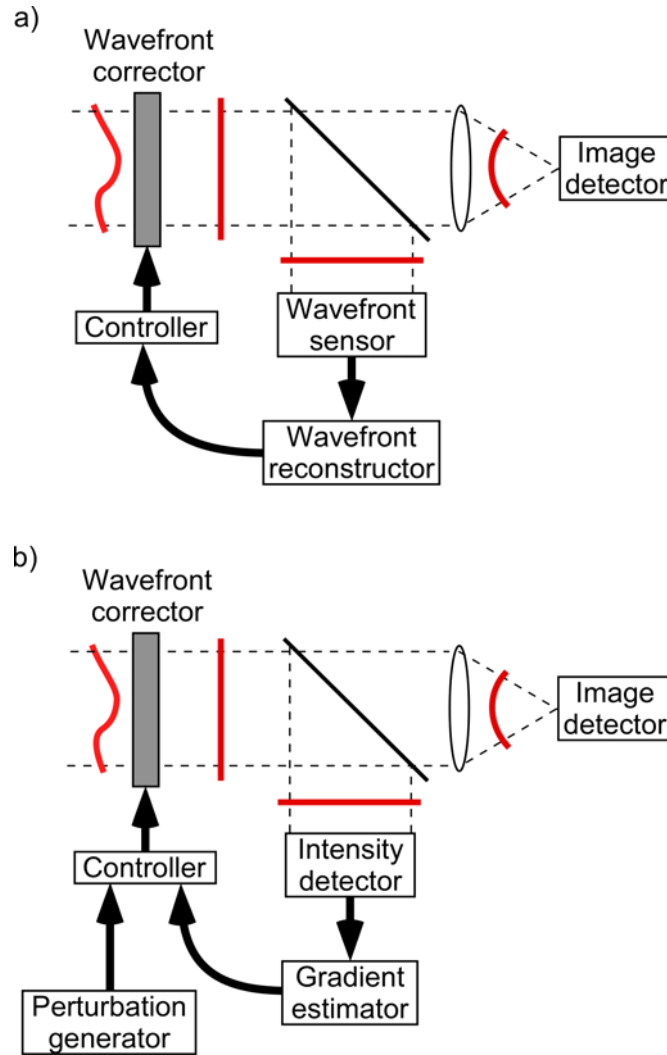
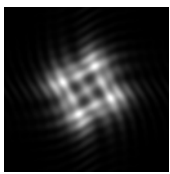


Fig. 1.1. Basic closed-loop adaptive optics schemes. By using a wavefront sensor (a) the wavefront distortions of the incident light can be reconstructed. A wavefront corrector applies the phase conjugate of the reconstructed wavefront on the distorted wavefront and, thus, sharpens the image on the detector. Without wavefront sensing (b) a set of trial phase perturbation on the incident light is applied to estimate the gradient of a merit function. The merit function, relying on an intensity measurement, can be the image sharpness or the maximum intensity. The optimal correction is derived from this set of measurements depending on the chosen search algorithm.



Since then the potential of adaptive optics has been discovered for many other disciplines comprising, e.g. the compensation of thermal effects in high-power laser systems, such as PHELIX (Petawatt High Energy Laser for heavy Ion experiments [Oughstun, 1981; Kuehl et al., 2005]), the correction of the eye's aberrations for supernormal vision and high-resolution retinal imaging [Dreher et al., 1989; Liang et al., 1994; Liang et al., 1997], compensation of the turbulent atmosphere for free-space laser communication [Primmerman et al., 1995], the correction of spherical aberration due to refractive-index mismatch between sample and cover glass for optical trapping [Ota et al., 2003] and the correction of the refractive-index mismatch present in writing and reading optical data storage devices [Booth et al., 2006].

In a similar manner, refractive-index variations in biological specimens often degrade the resolution, signal and contrast of optical imaging, in particular, of multi-photon microscopy [Denk et al., 1990] and confocal microscopy [Minsky, 1961]. Confocal microscopy is strongly compromised by aberrations in the optical path since both the excitation light focused in the specimen and the fluorescence light focused on a pinhole are degraded by heterogeneities within the specimen. In multi-photon microscopy only aberrations imposed on the excitation light affect the resolution. However, due to its quadratic dependence on the excitation intensity, the resolution of a two-photon microscope suffers in a similar manner to a confocal microscope [Schwertner et al., 2004].

Just as the refractive-index variations of the atmosphere exhibit a broad spectrum [Tatarski, 1961], the refractive-index variations observed in biological tissue range from the size of macromolecules over the sizes of cells (2 - 50 μm) to the length of blood vessels [Schmitt et al., 1996]. Predominantly, refractive-index variations on a mesoscopic or macroscopic scale within the specimen and refractive-index transitions, e.g., due to a refractive-index mismatch between the immersion medium and the specimen [Gibson et al., 1991; Sheppard et al., 1991; Sheppard et al., 1997; Diaspro et al., 2002; Westphal et al., 2002] directly affect the quality of the focus. It is expected that imaging through specimens containing, e.g., blood vessels or clusters of cells can be enhanced by pre-compensation of wavefront distortions [Beuthan et al., 1996; Helmchen et al., 2002; Helmchen et al., 2005]. Meanwhile, two techniques are often employed to circumvent inhomogeneities in the refractive index: either removal of the distorting tissue by surgery [Helmchen et al., 2002; Mizrahi et al., 2004] or

optical clearing with biocompatible agents [Cicchi et al., 2005; Tuchin, 2005] but both techniques constitute an encumbering encroachment for living animals.

Therefore, several groups have already identified the usefulness of adaptive optics for confocal and multi-photon microscopy. However, so far only wavefront sensorless adaptive optics was successfully implemented based on either genetic learning algorithms [Sherman et al., 2002], hill-climbing algorithms [Marsh et al., 2003], adaptive random search algorithms [Wright et al., 2005], or on a modal wavefront sensor¹ [Neil et al., 2000; Booth et al., 2002]. All these wavefront correction schemes rely on fluorescence excitation and are restricted to strongly and widely stained specimens. Finding the correction parameters in wavefront sensorless adaptive optics usually requires numerous iterations, during which fluorophores photo-bleach and the tissue is exposed to photodynamic damage.

To circumvent these drawbacks wavefront correction based on coherence-gated wavefront sensing (CGWS, [Feierabend et al., 2004; Rueckel et al., 2006b]) has been developed. This technique is independent of fluorescence generation but is instead based on backscattered light and allows non-iterative wavefront correction. Backscattered light originates from different locations within the specimen but only light scattered in the peri-focal region carries the appropriate information about the distortions to restore a diffraction-limited focus (Fig. 1.2). To select only in-focus scattered light and, thus, to reject the remaining out-of focus scattered light, CGWS is based on coherence-gating by using a low-coherence interferometer, similar to optical coherence tomography [Huang et al., 1991]. In order to center the coherence-gate (CG) position at the focus, the optical path length of the reference light needs to match the optical path length of sample light backscattered at the focus. Using phase-shifting interferometry (PSI) [Malacara, 1992], the phase of the in-focus scattered light is determined but needs to be unwrapped. However, speckle, a granular intensity pattern due to coherent effects [Goodman, 2000], are inevitable in CGWS and complicate the unwrapping process. As a robust and simple unwrapping method a virtual Shack-Hartmann sensor (vSHS, [Feierabend et al., 2004]) can be employed to reconstruct the least mean square error wavefront [Fried, 1998].

¹ Although it is called a wavefront sensor, it was not used to measure a wavefront [Booth; 2006].

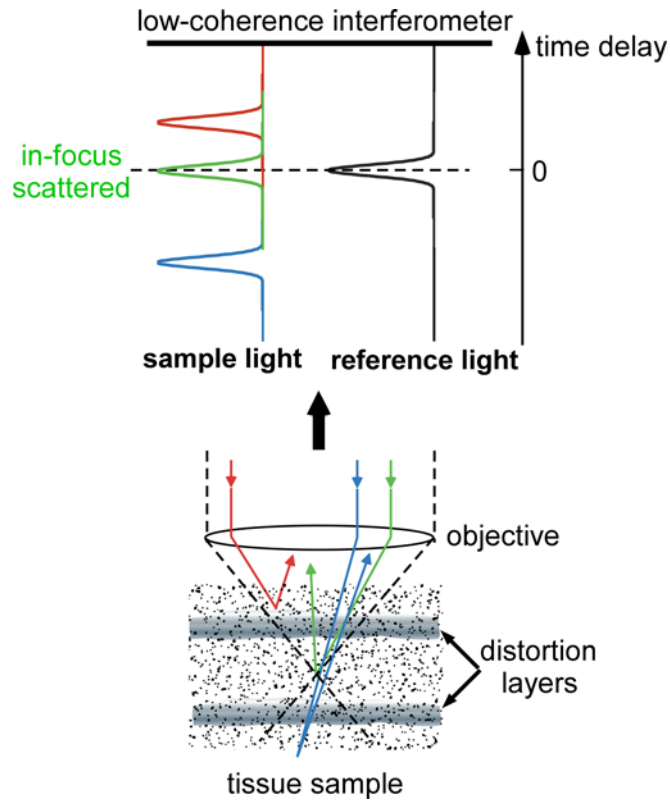
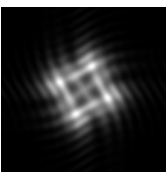
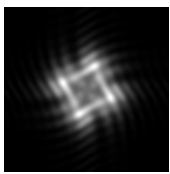


Fig. 1.2. Principle of coherence-gated wavefront sensing. The lower part of the figure shows that backscattering originates from different locations within the focal cone but only in-focus scattered light (green) needs to be selected whereas light scattered above the focus (red) and below the focus (blue) needs to be rejected. A low-coherence interferometer (upper part) employs coherence-gating to select only in-focus scattered light, i.e. only this light portion contributes to the interference with the reference light.

This dissertation is subdivided into two main parts: In the first part a theoretical model is developed to thoroughly characterize CGWS in terms of light properties, such as polarization and coherence length, and sample properties, such as density of scatterers. The emphasis lies on the investigation under which conditions CGWS fails to correctly measure the distortions introduced by the specimen (Chapter 2). In the second part CGWS-based wavefront correction for two-photon microscopy is demonstrated experimentally using various samples, ranging from artificial scattering phantoms to living zebrafish (Chapter 3). A brief introduction of two-photon microscopy and the principle of the Shack-Hartmann sensor (SHS), in particular, the virtual Shack-Hartmann sensor (vSHS), is given in the following (Chapter 1). The dissertation closes with a summary and an outlook of what would be necessary to

advance CGWS-based wavefront correction to make it routinely applicable to a variety of biological specimens (Chapter 4).



1.2 Two-photon microscopy

The invention of multi-photon microscopy by Denk et al. (1990) established a new access to optical fluorescence imaging, particularly in thick tissues and live animals [Denk et al., 1997]. In these specimens multi-photon microscopy is superior to confocal microscopy allowing high-resolution imaging deep within strongly scattering biological specimens [Svoboda et al., 1997]. While confocal microscopy is based on single-photon absorption to excite fluorescent molecules, in two-photon microscopy two photons interact nearly simultaneously ($\approx 10^{-16}$ s) with the molecule, producing an excitation that is similar to the absorption of a single photon, possessing approximately twice the energy [Göppert-Mayer, 1931]. Two-photon absorption cross-sections of the fluorescence dyes commonly used are extremely small ($1 \cdot 10^{-50} \text{ cm}^4 \text{ s}$ to $300 \cdot 10^{-50} \text{ cm}^4 \text{ s}$, [Zipfel et al., 2003]) and, thus, sufficient fluorescence generation requires spatial and temporal confinement of the excitation photons, accomplished by using high numerical aperture objectives and pulsed lasers. Typically, an average laser power of up to a few tens of mW illuminates the specimen while raster scanning a thin plane within the tissue [Theer et al., 2003].

Since two-photon excitation is a nonlinear process, depending quadratically on the intensity of the excitation light, fluorescence generation is restricted to the focus where the intensity is highest. This intrinsic optical sectioning ability leads to major advantages over single-photon techniques (Fig. 1.3): first, photodamage and photobleaching are confined to the focal region; second, even if the fluorescence light is scattered on the way back to the surface of the specimen it can contribute to the detected signal and, thus, allows a higher collection efficiency of useful signal light; third, near-infrared light is typically employed for two-photon absorption, which not only penetrates deeper into the scattering sample but also is less phototoxic [Helmchen et al., 2005].

Using regenerative amplifiers imaging depths up to 1 mm in neocortex can be achieved [Theer et al., 2003]. However, the deeper the light is focused within the specimen the more wavefront distortions are likely to occur, resulting in a blurred focus. By using adaptive optics a diffraction-limited focus can be restored and the maximum resolution should be attainable also very deep within the specimen [Marsh et al., 2003; Rueckel et al., 2006b]. Assuming a uniform illumination of the objective lens the maximum resolution of a two-photon microscope can be defined, for

example, as the full width at half maximum (FWHM) of a Gaussian fit to the intensity point-spread function [Zipfel et al., 2003]. Fitting the lateral and axial profile yields

$$\begin{aligned}\Delta_{xy} &= \frac{0.325\sqrt{2\ln 2} \lambda}{NA^{0.91}}, \quad NA > 0.7, \quad \text{and} \\ \Delta_z &= 0.532\sqrt{2\ln 2} \lambda \cdot \left[\frac{1}{n - \sqrt{n^2 - NA^2}} \right],\end{aligned}\tag{1.1}$$

where λ , NA and n are the wavelength of light, numerical aperture of the objective and the refractive index of the immersion medium, respectively.

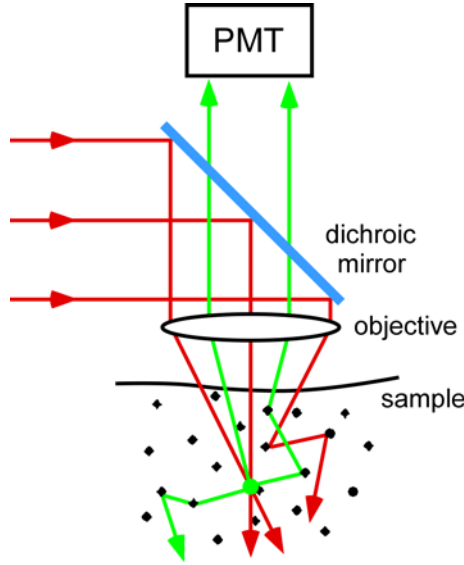
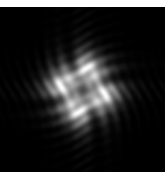


Fig. 1.3. Principle of two-photon microscopy. Near-infrared light (red lines) is reflected from a dichroic mirror and is focused by an objective to a diffraction-limited spot within the sample. Due to scattering, only a fraction of the excitation light generates fluorescence at the focus (green spot) via two-photon absorption; however, scattered light is too diluted to cause two-photon excitation. Ballistic and scattered fluorescent light (green lines) can be detected if collected by the objective.



1.3 Shack-Hartmann sensor

1.3.1 Real Shack-Hartmann sensor

An important device for many adaptive optics schemes is the wavefront sensor. The most familiar types are the Shack-Hartmann sensor [Shack et al., 1971], the shearing interferometer [Wyant, 1974], the curvature sensor [Roddier, 1988], and the pyramidal wavefront sensor [Ragazzoni, 1996].

Due to its simplicity and robustness the Shack-Hartmann sensor (SHS) is probably the most popular one. The SHS is based on the local measurement of the wavefront gradient by inserting a phase mask into the light beam. Such a mask is commonly an array of contiguous sublenses covering the entire aperture (Fig. 1.4). Light passing through these sublenses produces an array of foci in the focal plane. For a flat wavefront the array is regular, i.e. each focus is located on the optical axis of its corresponding sublens. An irregular pattern of foci arises, encoding the local wavefront tilts, if an aberrated wavefront passes the array of sublenses.

The propagation of the electric field of the light through a sublens can be described as a Fourier transformation. It can, therefore, be shown that the displacement of the centroid (g_x, g_y) of the focal intensity distribution from the optical axis is [Primot et al., 1990; Barchers et al., 2002]

$$g_x = \frac{\frac{f\lambda}{2\pi A} \iint_A dx dy I(x, y) \frac{\partial \phi(x, y)}{\partial x}}{\iint_A dx dy I(x, y)} \quad (1.2)$$

$$g_y = \frac{\frac{f\lambda}{2\pi A} \iint_A dx dy I(x, y) \frac{\partial \phi(x, y)}{\partial y}}{\iint_A dx dy I(x, y)},$$

where f and A are the focal length and the area of a single sublens, respectively; λ is the wavelength. The intensity and the phase distribution across the aperture are $I(x, y)$ and $\phi(x, y)$, respectively.

Only if the intensity distribution is nearly uniform, does the displacement of the centroid correspond directly to the wavefront tilt averaged over the area of a single

sublens; otherwise the wavefront measured by a SHS is complicated by intensity scintillation [Barchers et al., 2002].

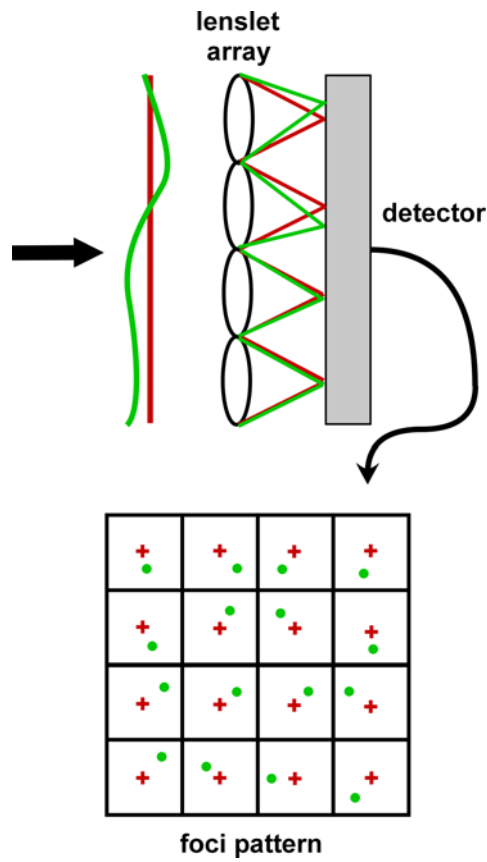
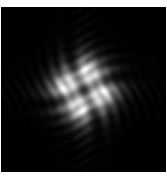


Fig. 1.4. Principle of the Shack-Hartmann sensor. For a flat wavefront the focus for each sublens is located on the optical axis yielding a regular pattern of foci on the detector (red crosses). An irregular foci pattern encodes the information of the local wavefront tilt of an aberrated wavefront (green dots).



1.3.2 Virtual Shack-Hartmann sensor

The virtual Shack-Hartmann sensor (vSHS) simulates numerically the individual steps in a real SHS [Feierabend et al., 2004; Rueckel et al., 2006a]. As an input the vSHS requires the measurement of the electric field across the entire aperture where the wavefront is to be sensed.

The electric field can be measured by using PSI [Malacara, 1992]. Applying a four-step algorithm with phase steps of $\delta_i = 0, \pi/2, \pi, 3\pi/2$ ($i = 1, 2, 3, 4$), introduced into the reference beam, four interferogram intensity patterns $I_i(x, y)$ are recorded:

$$\begin{aligned} I_1(x, y) &= I'(x, y) + I''(x, y) \cos[\phi(x, y)], \\ I_2(x, y) &= I'(x, y) + I''(x, y) \cos[\phi(x, y) + \pi/2], \\ I_3(x, y) &= I'(x, y) + I''(x, y) \cos[\phi(x, y) + \pi], \text{ and} \\ I_4(x, y) &= I'(x, y) + I''(x, y) \cos[\phi(x, y) + 3\pi/2]. \end{aligned} \quad (1.3)$$

The average intensity of both reference and sample beams together is $I'(x, y)$; the intensity modulation is $I''(x, y)$; the wavefront of the sample light is denoted by $\phi(x, y)$. It is assumed that the reference wavefront is flat. The electric field of the sample light is then

$$\begin{aligned} E(x, y) &\propto (I_1(x, y) - I_3(x, y)) + i(I_4(x, y) - I_2(x, y)) \\ &\propto 2I''(x, y) \exp(i\phi(x, y)). \end{aligned} \quad (1.4)$$

As in the real SHS the vSHS divides the entire aperture into a number of sublenses, each performing a discrete Fourier transformation of the electric field $E(r, s)$ over its aperture (x and y are discretized by pixel coordinates r and s, respectively). In order to get an accurate estimation of the centroid, a highly sampled diffraction pattern is produced. Therefore, the electric field of each sublens, sampled by $V \times V$ pixels, is zero-padded to a field of $N \times N$ pixels. The intensity distribution for the diffraction pattern of one sublens is

$$I(m, n) = \left| \sum_{r=0}^{N-1} \sum_{s=0}^{N-1} E(r, s) \cdot \exp(-i \frac{2\pi}{N} \cdot (r \cdot m + s \cdot n)) \right|^2, \quad (1.5)$$

where m and n are the pixel coordinates of the diffraction pattern ($0 < m, n < N-1$), which is, thus, sampled in steps of $\lambda \cdot f / (N \cdot \Delta x)$ and $\lambda \cdot f / (N \cdot \Delta y)$ in x - and y -direction; λ is the wavelength of the light and f the focal length of the sublens; Δx and Δy are the sizes of the pixels in x - and y -direction in the aperture, respectively.

Then, the average slope of the wavefront across one sublens is estimated using the centroid, which is evaluated across a window with a size of S by S pixels centered at the peak of the diffraction pattern.

To expand the wavefront $\phi(x, y)$ over the aperture (circular aperture with radius R) into a series of Zernike modes Z_m ([Noll, 1976], see Appendix A)

$$\phi(x, y) = \sum_m c_m \cdot Z_m(x/R, y/R), \quad (1.6)$$

the linear relationship between the wavefront gradients in x - and y -direction

$$g = \begin{pmatrix} g_x \\ g_y \end{pmatrix} \text{ to the Zernike coefficients } \mathbf{c} = \begin{pmatrix} c_1 \\ \vdots \\ c_M \end{pmatrix} \text{ (M is the maximum Zernike mode}$$

taken into account) is used (see Eq. (1.2)):

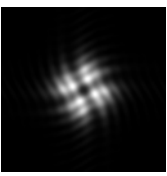
$$\mathbf{g} = \begin{pmatrix} D_x \\ D_y \end{pmatrix} \cdot \mathbf{c} = D \cdot \mathbf{c} \text{ with the matrix elements}$$

$$D_x^{(q,m)} = \frac{f \lambda R}{2\pi A} \frac{\iint_{A_q} dx dy I(x, y) \frac{\partial Z_m(x/R, y/R)}{\partial x}}{\iint_{A_q} dx dy I(x, y)}$$

and

$$D_y^{(q,m)} = \frac{f \lambda R}{2\pi A} \frac{\iint_{A_q} dx dy I(x, y) \frac{\partial Z_m(x/R, y/R)}{\partial y}}{\iint_{A_q} dx dy I(x, y)}. \quad (1.7)$$

The size of both matrices D_x and D_y is Q by M , where Q is the number of sublenses covering the entire aperture. Using the pseudo-inverse of D the wavefront with the least-squares error to the wavefront gradient is obtained by [Cubalchini, 1979]



$$\mathbf{c} = \left(D^T D \right)^{-1} D^T \cdot \mathbf{g}. \quad (1.8)$$

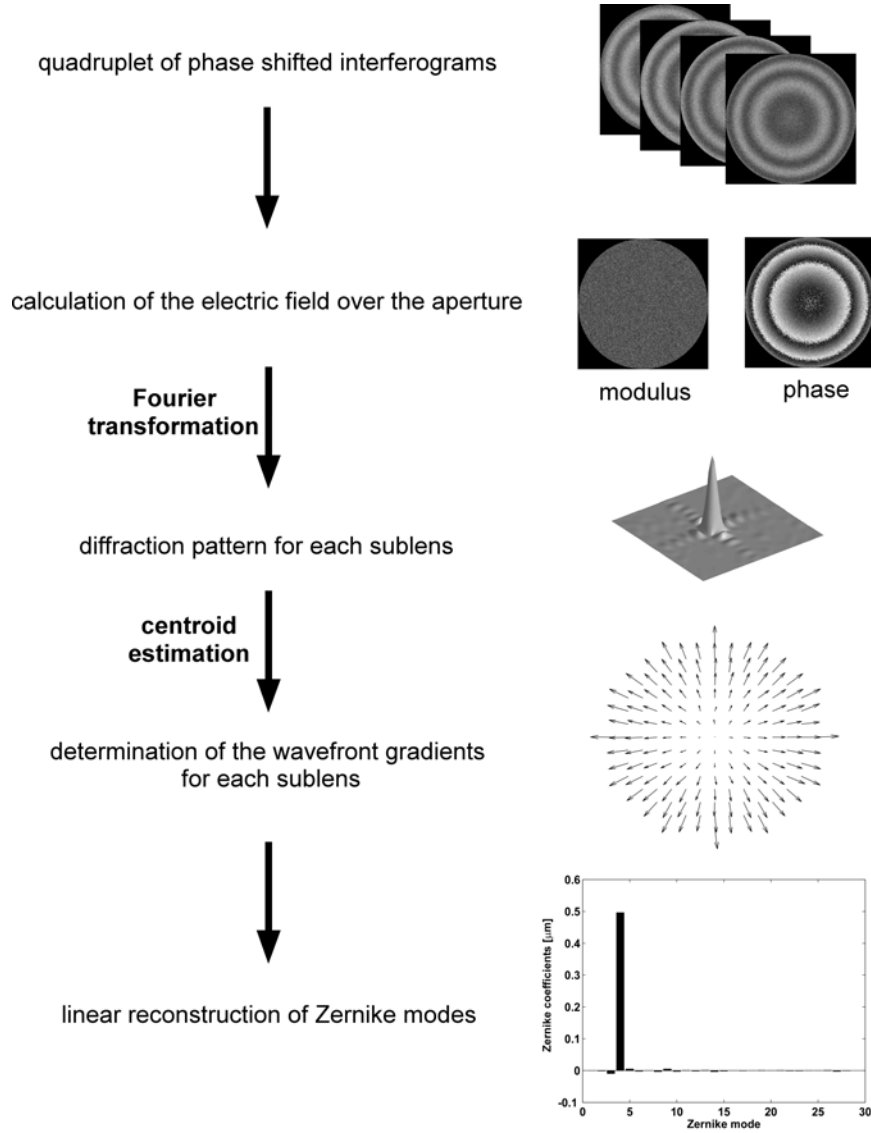
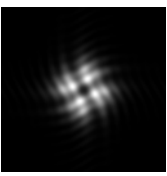


Fig. 1.5. Principle of the vSHS as described in the text. The images are all numerically calculated for a wavefront with a Zernike defocus (mode 4) of $0.5 \mu\text{m}$ and take photon noise into account ($2 \cdot 10^5$ sample arm photons, $4 \cdot 10^7$ reference arm photons, 148 sublenses).

Compared to the real SHS the vSHS has several advantages. First, saturation effects that occur in a real SHS due to focusing of light on the detector are avoided since the electric field for the vSHS is experimentally measured by interferometry where the intensity is rather uniform across the entire aperture. This allows a larger dynamic

range. Second, the number of sublenses can easily be adjusted to the number of expected Zernike modes. Furthermore, the “unwrapping” of the wavefront by the vSHS is very robust in terms of singularities [Nye et al., 1974] and can easily be used to extract the least mean square error phase from interferometric measured data [Fried, 1998].



2 Coherence-gated wavefront sensing

In order to evaluate the performance of CGWS-based wavefront correction a thorough characterization of CGWS is needed, both experimentally and theoretically. Therefore, a comprehensive model for CGWS was developed based on geometrical optics and single-scattering events. To compare it to experimental data, a Monte-Carlo simulation (MCS) was implemented, which provides the statistical predictions of the model. By investigating CGWS while varying parameters of the illumination light and of the tissue, such as polarization, coherence length, and density and sizes of scatterers, this chapter aims to verify that CGWS-measured wavefronts represent actual aberrations. Furthermore, the assumptions used for the model are discussed at the end.

2.1 The principle of CGWS

All parameters needed for wavefront correction are determined by sensing the wavefront of the coherence-gated backscattered light and, thus, the distortions in the optical path. In order to sense all distortions up to the focus, the CGWS needs to select light scattered back near the focus. With low-coherence interferometry such a differentiation between light scattered out-of-focus and in-focus can be accomplished by using the fact that the time travelled by light scattered at different locations within the sample is different and thus allows coherence-gating.

In the following a comprehensive model is developed to derive the characteristic properties of CGWS. The concept of the model is similar to models of optical coherence tomography (OCT, [Huang et al., 1991]) but, of course, focuses on the phase of the backscattered light instead of the intensity [Schmitt, 1999; Fercher et al., 2003; Karamata et al., 2005]. Based on ray-tracing, the model determines the optical distance travelled by scattered light and assumes a distribution of discrete scatterers within the geometrical focal cone. Only singly scattered light will be taken into account whereas multiply scattered light is neglected; the effect of multiple scattering will be discussed later (see section 2.7). An optical arrangement is assumed where the

backscattered sample light \mathbf{E}_S interferes with the reference light \mathbf{E}_{Ref} on a detector, which is parameterized by the two coordinates u and v . The intensity of the interferogram $I(u, v)$ is

$$I(u, v) = I_{Ref}(u, v) + I_S(u, v) + 2 \cdot \overline{\text{Re}\{\mathbf{E}_{Ref}^*(u, v, t) \cdot \sum_k \mathbf{E}_S^{(k)}(u, v, t + \tau^{(k)}(u, v))\}}. \quad (2.1)$$

I_{Ref} and I_S are the intensities for reference and backscattered sample light, respectively, the electric field in the sample arm is $\mathbf{E}_S = \sum_k \mathbf{E}_S^{(k)}(u, v, t + \tau^{(k)}(u, v))$,

where $\tau^{(k)}$ is the difference in time between light scattered at the scatterer k and light traveled in the reference arm. The sum is over all scatterers within the focal cone. Averaging over time t is denoted by the bar.

The temporal correlation between electric fields is related to the complex degree of self coherence $\gamma(\tau)$ (normalized self coherence function, [Goodman, 2000]) of the scalar electric field E

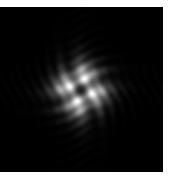
$$\gamma(\tau) = \frac{\overline{E^*(t) \cdot E(t + \tau)}}{\overline{E^*(t) \cdot E(t)}} = |\gamma(\tau)| \cdot \exp(-i\omega\tau). \quad (2.2)$$

Equation (2.1) can then be simplified to

$$I = I_{Ref} + I_S + 2 \cdot \overline{\text{Re}\{A_{Ref} \sum_k (\mathbf{p}_{Ref}^* \cdot \mathbf{p}_S^{(k)}) \cdot A_S^{(k)} \cdot |\gamma(\tau^{(k)})| \cdot \exp(-i\omega \tau^{(k)})\}}. \quad (2.3)$$

The amplitudes of the electric field of the reference and sample light are A_{Ref} and $A_S^{(k)}$, respectively, and the polarization of the reference light and backscattered sample light are \mathbf{p}_{Ref} and \mathbf{p}_S , respectively. For clarity, the dependence on u and v is omitted and in the following the scalar product $\mathbf{p}_{Ref}^* \cdot \mathbf{p}_S^{(k)}$ is replaced by $W_{Pol}^{(k)}$.

The first two terms in Eq. (2.3) are the total intensities of the backscattered sample light and reference light, which include no coherence gating. Therefore, these terms need to be subtracted, which can be done by using phase shifting interferometry (PSI, see section 1.3.2). The third term, however, contains the self coherence function



$|\gamma(\tau^{(k)})|$, whose finite width allows the selection of backscattered light that has traveled a certain time.

In Fig. 2.1 the calculation of $\tau^{(k)}$ for a scatterer at the location $P(x,y,z)$ is illustrated using the propagation of plane waves. Since the analytical expression for $\tau^{(k)}$ can be easily calculated, if the wavefront is determined in the back focal plane of the objective, it is assumed that backscattered sample light and reference light interfere on a detector located in a plane that is optically conjugated to the back focal plane. Further, it is assumed that the wavefront of the reference light is flat. If the coherence-gate (CG) position is at the focus, i.e. the time traveled by the reference light matches the time traveled by the sample light scattered at the focus F , then the optical distance traveled by the reference light corresponds to sample light that has traveled twice the distance from the focus F to the point C on the back focal plane (C-F-C, Fig. 2.1). Thus, $\tau^{(k)}$ is the difference in time for light propagating C-F-C and A-P-B (arbitrarily chosen sample light path):

$$\tau(\mathbf{r}^{(k)}, \mathbf{w}(u, v)) = \frac{n_s}{c} [-\text{sgn}(z) \cdot |\mathbf{r}^{(k)}| - \mathbf{r}^{(k)} \cdot \mathbf{w}(u, v)], \quad (2.4)$$

where $\mathbf{r}^{(k)}$ is the vector connecting the focus F to the location of the scatterer $P(x,y,z)$, \mathbf{w} indicates the direction of the scattered light (unit vector), c is the velocity of light in vacuum, and n_s is the refractive index of the sample. The origin of the coordinate system x, y and z lies at the focus. If the length of the reference arm is changed by the distance L an additional term of L/c has to be inserted in Eq. (2.4), i.e. the CG position is displaced by $L/(2n_s)$. The time $\tau^{(k)}$ determines the contribution of each back-propagating planar wave scattered at the scatterer k to the interference term of Eq. (2.3) via the self coherence function $|\gamma(\tau^{(k)})|$.

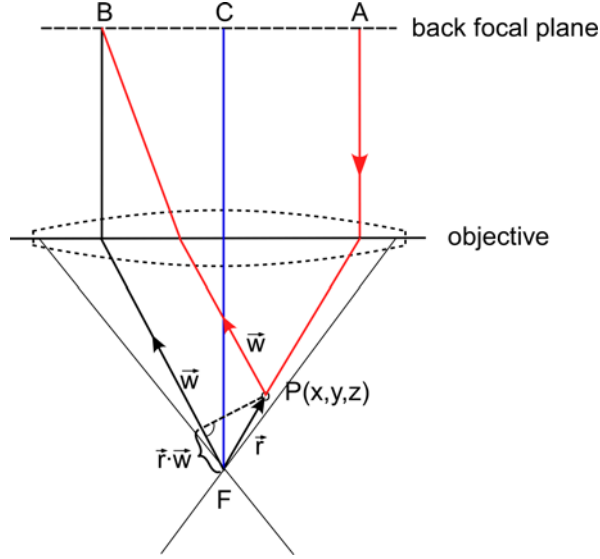
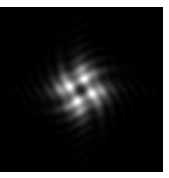


Fig. 2.1. The calculation of $\tau^{(k)}$ for backscattered sample light based on the propagation of plane waves. The illumination wave passes the back focal plane at point A, is refracted by the objective lens towards the focus F, scattered at P (which has the coordinates x , y , and z) in the direction of the vector \vec{w} (unit vector) and crosses the back focal plane at B on the way back (red marked path). For a CG position at the focus the reference light takes an equally long optical path as C-F-C (blue marked path). The optical path length A-F-B is equal to C-F-C.

The phase of the coherence-gated backscattered light $\Phi(u, v)$ (reference wavefront is flat) can now be directly obtained by taking the argument of the interference term in Eq. (2.3)

$$\Phi(u, v) = \arg \left\{ \sum_k W_{pol}^{(k)}(u, v) \cdot A_S^{(k)}(u, v) \cdot \left| \gamma(\tau^{(k)}(u, v)) \right| \cdot \exp(-i\omega \tau^{(k)}(u, v)) \right\}, \quad (2.5)$$

but is only known modulo 2π (for example in the interval $[0; 2\pi[$). Therefore, $\Phi(u, v)$ needs to be unwrapped to reconstruct the actual wavefront. All available phase unwrapping methods are encumbered by path inconsistencies due to noise, singularities [Ghiglia et al., 1987], and discontinuities [Gens, 2003] and may not be solvable with the desired L^0 norm in polynomial time [Chen et al., 2000]. However, singularities due to speckle noise, which is unavoidable with scattering samples, are intrinsic to CGWS (see section 2.4.2) and, thus, a method has to be used that is able to reconstruct reliably the wavefront in the presence of speckle. It will be shown that the



virtual Shack-Hartmann sensor (vSHS) fulfills this requirement (see section 1.3.2). The vSHS propagates the electric field $\exp(i\Phi(u, v))$ (here with uniform amplitude) numerically through a virtual lenslet array onto a virtual spatially resolved detector, where the wavefront is then reconstructed as in a real SHS. Since singularities due to speckle noise occur only at points of zero amplitude [Nye et al., 1974] and are, therefore, weighted by zero intensity, the propagation of the amplitude together with the complex phase $\exp(i\Phi(u, v))$ should have a lower distorting effect on the diffraction patterns of the vSHS. The complete coherence-gated electric field is

$$E_{CGWS}(u, v) \propto \sum_k W_{Pol}^{(k)}(u, v) \cdot A_S^{(k)}(u, v) \cdot |\gamma(\tau^{(k)}(u, v))| \cdot \exp(-i\omega \tau^{(k)}(u, v)). \quad (2.6)$$

The uniform amplitude of the reference light A_{Ref} (Eq. (2.3)) does not change the diffraction patterns and is replaced by 1. However, Monte-Carlo simulations (see section 2.2.2) showed that propagating $\exp(i\Phi(u, v))$ or $E_{CGWS}(u, v)$ led to almost the same reconstructed wavefront. Nevertheless, the propagation of the amplitude-weighted coherence-gated electric field $E_{CGWS}(u, v)$ was used for the vSHS to determine the wavefront, both experimentally and numerically.

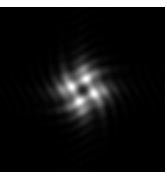
The CGWS-measured electric field E_{CGWS} at the position (u, v) is the superposition of plane waves, scattered from all scatterers in the considered direction. The self coherence $|\gamma(\tau^{(k)}(u, v))|$ weights each scattered wave in such a way that almost only that light portion that is scattered close to the focus is weighted and selected (see section 2.4.1).

For a sublens of the vSHS the diffraction pattern detected by a virtual detector (parameterized by r and q) is

$$\begin{aligned} I(r, q) &\propto \left| \iint_A E_{CGWS}(u, v) \exp\left[-i \frac{2\pi}{\lambda \cdot f} (u \cdot r + v \cdot q)\right] dudv \right|^2 = |\mathcal{E}_{CGWS}(r, q)|^2 \\ &= \sum_k |\mathcal{E}_S^{(k)}(r, q)|^2 + \sum_m \sum_{n \neq m} [\mathcal{E}_S^{(m)}(r, q)]^* \cdot \mathcal{E}_S^{(n)}(r, q), \end{aligned} \quad (2.7)$$

where λ is the wavelength of the light, f is the focal length of the sublenses, and A is the area of the sublens. The Fourier transformation of the CGWS-selected electric field is $\mathcal{E}_{CGWS}(r, q) = \sum_k \mathcal{E}_S^{(k)}(r, q)$.

The first term in Eq. (2.7) represents the incoherent and the second term the coherent superposition of the individual electric fields, which together yield the total diffraction pattern. The properties of these two terms and their influence on the CGWS-measured wavefront will be discussed in section 2.4.



2.2 Implementation of CGWS

CGWS was investigated and implemented both experimentally and numerically. The experimental setup consisted not only of a CGWS but also included CGWS-based wavefront correction using a deformable mirror and a two-photon microscope. Numerically, a Monte-Carlo simulation based on the model derived in section 2.1 was implemented to obtain predictions to be compared to experimental data.

2.2.1 Experimental implementation

Optical setup

The optical setup was designed not only to determine the aberrations introduced in the optical path by CGWS but also to correct for these aberrations using a deformable mirror (DM, gold-coated electrostatically-deflected membrane, Oko Technologies, Fig. 2.2). For microscopic imaging it also contains a two-photon microscope. For CGWS a low-coherence interferometer consisting of sample arm and reference arm selects that portion of the backscattered sample light that was scattered in the peri-focal region. To select the proper time delay, the length of the reference arm has to be adjusted by displacing a right-angle prism mounted on a computer-controlled translation stage (for electronic control see Appendix B). The low coherent light is provided by a mode-locked Ti:Sapphire Laser (Coherent, Mira 900 pumped with Verdi V18) with a wavelength of 930 nm and a spectrum width of 15 nm (FWHM) corresponding to a coherence length of 51 μm .

For CGWS the wavefront is measured at the back aperture of the objective (IR-Achroplan, 63x/0.90 W, Zeiss) imaged by two telescopes (L3/L4 and L5/L6), which ensure that the CCD camera (Sony, XC-77, pixel size: 13 μm x 13 μm , standard monochrome video camera based on the RS-170 standard), the DM, and the back aperture of the objective are optically conjugated. A magnification of two for both telescopes was chosen to sample the back aperture with a sufficient number of pixels (see section 2.4.3) and to use only the well controllable center area of the deformable mirror with a diameter of 9.7 mm (total diameter of DM is 15 mm) for wavefront

correction [Paterson et al., 2000]. In order to overfill the back aperture of the objective, the beam entering the interferometer is expanded by a factor of 1.6 to 6.3 mm ($1/e^2$ width) horizontally and 5.6 mm ($1/e^2$ width) vertically using two lenses (L1/L2). Thus, the fill factor is 1.25.

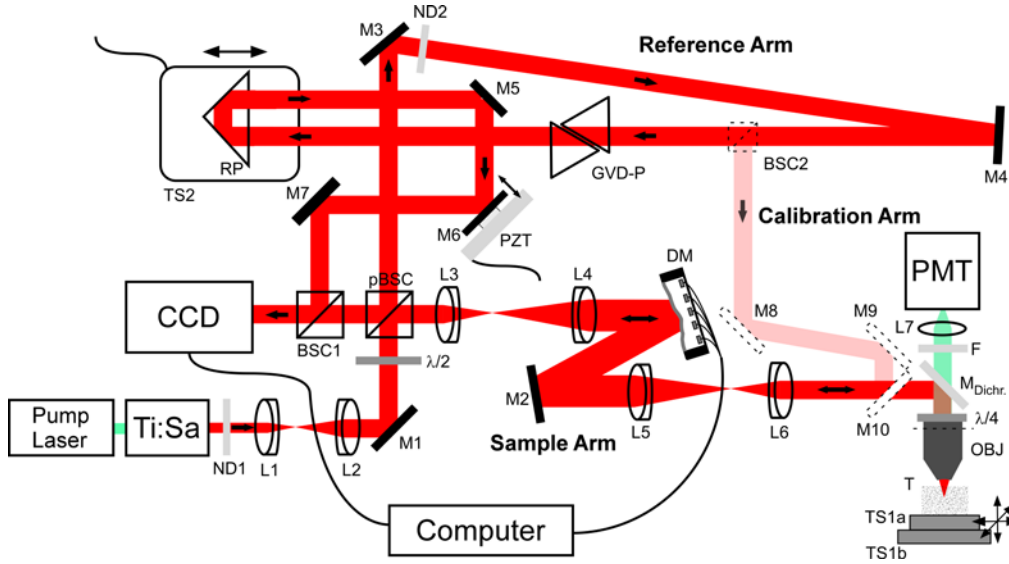
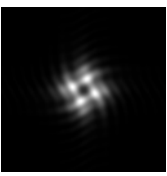


Fig. 2.2. Experimental Setup. The components used are: Ti:Sapphire Laser (Coherent Mira, center wavelength 930 nm, coherence length 51 μ m), neutral density filters ND1 (Edmund Optics, filter wheel 0.04-3 D, NT54-081) and ND2 (1.7 D, Linos, 371144), near-infrared achromatic doublets L1 (focal length 5 cm, Edmund Optics, NT45-803), L2 (focal length 8 cm, Linos, 322393), L3 (focal length 7.5 cm, Thorlabs, AC254-075-B), L4 (focal length 15 cm, Thorlabs, AC254-150-B), L5 (focal length 20 cm, Thorlabs, AC254-200-B), L6 (focal length 10 cm, Edmund Optics, NT45-806), silver-coated mirrors M1-7 (Linos, 340525), $\lambda/2$ wave-plate (Newport Corp., 10RP42-3), polarizing beamsplitter cube pBSC (Linos, 335523), non-polarizing beamsplitter cube BSC1 (Thorlabs, BS011), deformable mirror DM (Oko Technologies, 37 ch), dichroic mirror $M_{Dichr.}$ (designed to reflect infrared light (800 to 1050 nm) but to transmit the fluorescent light around 525 nm, Chroma), $\lambda/4$ wave-plate (Newport Corp., 10RP44-3), objective OBJ (IR-Achroplan 63x/0.90W, Zeiss), piezo-driven translation stage TS1a (Piezosystem Jena, Tritor 102 SG), motorized translation stage TS1b (MP 285, Sutter Instrument Company) blue-green filter F (Linos, BG38, 370043), lens L7 (focal length 2.5 cm, Linos, 063021), photomultiplier tube PMT (Hamamatsu, R3896), CCD chip (Sony, XC-77), group velocity-dispersion compensation prisms GVD-P (BK7, Linos, 336615), right-angle prism RP (Thorlabs, PS908), piezo-driven translation stage TS2 (Piezosystem Jena, PX 400), and tissue sample T. For the calibration arm are used: non polarizing beamsplitter cube BSC2 (Thorlabs, BS011) and silver-coated mirrors M8-10 (Linos, 340525). The light-propagation directions are indicated by arrows.



The intensities for both interferometer arms are adjusted by a polarizing beamsplitter cube in combination with a $\lambda/2$ -waveplate. Neutral density filters in the reference arm reduce the intensity further so that backscattered sample light and reference light have approximately the same intensities, which results in a proper use of the dynamic range of the CCD camera.

The $\lambda/4$ -waveplate in the sample arm has two functions: first, it changes the linear polarization of the illumination light into circular polarization, which is essential to avoid spurious aberrations sensed by CGWS (see section 2.6), second, it rotates the polarization of the returning sample light by 90° and, therefore, allows a polarizing beamsplitter to redirect the backscattered sample light into the CGWS, resulting in a highly efficient use of the backscattered light.

Since several cm of glass in the sample arm (due to four achromats and the objective) lead to group-velocity dispersion and, thus, to a broadening of the coherence gate, BK7 glass prisms were inserted into the reference arm to minimize the coherence gate length. For almost all measurements 6 cm of glass were used, which is much less than needed for optimal compensation and resulted in a coherence-gate length of $32\ \mu\text{m}$ (measured as the FWHM width of the interference contrast vs. CG position using a mirror sample, [Feierabend, 2004]) within an aqueous sample. Nearly full compensation (gate length of $22\ \mu\text{m}$) was achieved with 20 cm of BK7 glass and was used for imaging in zebrafish (see section 3.5).

To reconstruct the electric field of the CGWS-selected backscattered light and to subtract the intensities of the reference and sample light (see Eq.(2.3)), a four-step algorithm is employed to implement PSI (see section 1.3.2). The necessary phase steps of $\lambda/4$ are introduced by the mirror M6 glued to a piezo element. The motion of the piezo element is synchronized to the frame rate of the video camera (see Feierabend (2004) for a detailed description).

For two-photon microscopy a dichroic mirror in the sample arm separates the infrared illumination light used for two-photon excitation from the fluorescence light, which is focused onto a photomultiplier tube. While CGWS, as it is implemented here, needs only a light power of some tens of nW, for two-photon absorption, typically, a few mW [Denk et al., 1990] are needed at the focus. Therefore, the intensity of the laser light was adjusted between CGWS-based wavefront correction and two-photon imaging, which was done using a filter wheel. Images were recorded with a digital resolution of 128×128 pixels. The specimen was mounted on the piezo-driven

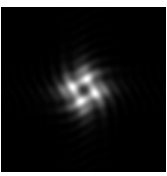
translation stage that is used for scanning and which, in turn, is mounted on a motorized stage for coarse displacements. For scanning in x- and y-directions sinusoidal and saw-tooth signals with periods of 30 ms and 3.8 s, respectively, were applied to the translation stage. The drive voltages were controlled by a program called CFNT (see Appendix B).

Reconstruction of the wavefront

In this section the prevalent parameters used experimentally for the wavefront reconstruction are discussed. Since the reconstruction is based on the vSHS, the processing steps closely follow those given in section 1.3.2.

To reduce the effect of speckle, interferograms were recorded for 20 slightly different focus positions (using the motorized translation stage TS1b to change positions, Fig. 2.2), placed on a lateral grid with 1 μm spacing. For each position 5 of the quadruplets needed for four-step PSI were recorded in order to reduce photon shot noise. Then, the interferograms were averaged over the 5 quadruplets for each focus position and the electric field of the coherence-gated sample light was reconstructed using the PSI algorithm. For the vSHS the circular aperture was subdivided into 441 sublenses (15 sublenses across the diameter), each sublens contained 15 by 15 pixels of the reconstructed electric field with a pixel size in x- and y-direction of 13.0 μm and 13.17 μm , respectively. While the manufacturer specifies the pixel size of the CCD camera as 13 μm by 17 μm (incorrect specification, [Feierabend, 2004]), the sizes used here are those for which focus-dependent spurious astigmatism (Zernike mode 6) was minimal.

For an accurate estimation of the centroid a highly-sampled diffraction pattern was produced. Therefore, the measured electric field was zero-padded to a size of 65 by 65 pixels before Fourier transformation and, then, the centroid was determined inside a window with a size of 15 by 15 pixels centered on the peak intensity. The wavefront, described in terms of the first 28 Zernike modes (up to the 6th radial order, [Noll, 1976]), was reconstructed by least-squares fitting to the wavefront gradients and, then, averaged over the 20 different focus positions.



Sample preparation

Only sample preparations are described that were used for experiments presented in this chapter.

Scattering samples

The scattering samples contained polystyrene beads of 110 nm (15 beads/ μm^3 , Polysciences, 00876) and had a mean free path of $\approx 550 \mu\text{m}$. The beads were immobilized in an aqueous agarose gel (1% low-melting point A9414, Sigma). The samples contained either 100 μM fluorescein (fluorescein-sodium salt 46960, Fluka) or, alternatively, fluorescent beads (93 nm, 0.2 beads/ μm^3 , yellow-green FluorSpheres, Invitrogen, F8803). Fluorophores were added since these samples were also used to test CGWS-based wavefront correction (see section 3.3).

Further scattering samples were prepared to investigate polarization effects of CGWS and contained polystyrene beads comparable in size with the wavelength (1 μm diameter, 0.005 beads/ μm^3 , Polysciences, 07310) and fluorescent beads (93 nm, 0.2 beads/ μm^3 , yellow-green FluorSpheres, Invitrogen, F8803) embedded again in 1% agarose gel. These samples had a mean free path of $\approx 100 \mu\text{m}$.

Hippocampus-slice sample

Rat hippocampal organotypic slice cultures [Zhu et al., 2000] were fixed with 4% PFA (paraformaldehyde) in PBS (phosphate buffered saline).

2.2.2 Monte-Carlo Simulation

The Monte-Carlo simulation (MCS) is based on a randomly sampled distribution of discrete scatterers. It closely mimics the experimentally applied steps using the model derived in section 2.1 and follows a similar approach of Lu et al. (2004) that followed to analyze optical coherence tomography (OCT).

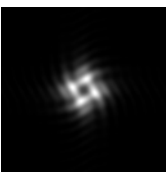
Since the time delay τ depends only on the location of the scatterer \mathbf{r} and on the direction of scattering \mathbf{w} (see Eq. (2.4)), the sum in Eq. (2.6) was calculated separately for each pixel on the detector for one ensemble of scatterers, which were distributed uniformly over the focal cone assuming a certain density (of scatterers).

By tracing the propagation of the polarization in the sample arm, taking into account the polarization of the illumination light and the change of polarization due to a generic objective and due to Mie scattering [Bohren, 1983], the weight function $W_{Pol}^{(k)}$ was calculated for each scattering event (implemented as a Matlab code, The MathWorks, Inc., for a detailed description see Appendix C). Since it is computationally very expensive to trace the polarization for all light rays, a simplified version of the MCS was also implemented that assumed that the weight function $W_{Pol}^{(k)}$ can be approximated by 1, i.e. the polarization of light was neglected. Also, the characteristic Mie-scattering phase functions were replaced by an isotropic scattering function. It will be demonstrated in the sections 2.4 and 2.5 that this simplified version of the MCS (implemented as a C-code) yields results that are consistent with experimental data as long as circularly polarized light is used (section 2.6). Therefore, this MCS was always employed unless the polarization dependence of CGWS was investigated.

No phase-shifting algorithm is required for the MCS to subtract the first two intensity terms in Eq. (2.3), since E_{CGWS} (see Eq. (2.6)) can be calculated directly. For the calculation of E_{CGWS} some further simplifications were made. First, in the geometrical optics limit the amplitude of the backscattered light depends only on the axial location z (the origin of the coordinate system is at the focus) of the scatterer and is $\propto 1/|z|$. Second, the lateral intensity profile was assumed to be uniform across the focus cone. Although a Gaussian profile with a fill factor of 1.25 (over the back aperture of the objective) was used experimentally (see section 2.2.1), MCSs showed the same results both for a uniform profile and the Gaussian profile experimentally used. Further, for the self coherence a Gaussian distribution was assumed:

$$|\gamma(\tau)| = \exp(-4 \ln(2) \cdot (c \cdot \tau / l_c)^2) \quad (2.8)$$

The coherence length is l_c (FWHM) and the velocity of light in vacuum is c . Usually the autocorrelation function of passively mode-locked laser is described by the squared hyperbolic secant function [Siegman, 1986], to which a Gaussian function is a good approximation (secant function has stronger wings).



For all MCSs narrowband light ($\Delta\nu \ll \bar{\nu}$) was assumed. Thus, all electric fields associated with all incoming light rays had the mean frequency $\bar{\nu}$. However, this is not strictly fulfilled for MCSs implemented for short coherence lengths, where the relative bandwidth can be as much as 10 %, even close to 100%. Therefore, MCSs where the incoming light rays had frequencies distributed over the complete width of the spectrum $\Delta\nu$ were implemented to determine deviations from the use of narrowband light. These simulations showed that the CGWS-measured wavefronts were the same whether narrowband light or broadband light was used, even for coherence lengths comparable to the wavelength.

To save computational time, some other deviations from the experimental parameters were used. Whereas the detector used experimentally samples the aperture by 375 pixels over the diameter, only 105 pixels were used for the MCS. As long as the speckle size is larger than 2 pixels, this assumption will not lead to significant deviations (see section 2.4.3). Furthermore, scatterers were distributed uniformly but only within $\pm 4l_c$ from the center of the CG position in axial direction. Due to the Gaussian profile of the self coherence function with a finite width of l_c , scatterers outside of this selected volume would have a weight very close to zero anyway.

After the coherence-gated electric field of the backscattered light was calculated, the wavefront was reconstructed using the vSHS. The same steps, as described in section 2.2.1 and 1.3.2, were used, except for the division of the aperture into 37 sublenses (instead of 441 sublenses), each comprising 15 by 15 pixels. In addition to the centroid estimation, the peak of the diffraction patterns was also estimated by least-squares fitting a Gaussian distribution to the central part of each diffraction pattern. In general, only the centroid estimation was used to reconstruct the wavefronts (see section 2.4.2).

2.3 Characterization of vSHS

2.3.1 Noise-free characterization

The performance of the vSHS for noise-free wavefronts was investigated numerically to determine implementation-dependent systematic errors in the wavefront sensing. Therefore, the average reconstruction error (RMS), calculated both for all 28 Zernike modes (piston excluded) and for all Zernike modes from 5 to 28, was determined for 15 random wavefronts with a certain, known deviation. Up to a deviation of $0.3 \mu\text{m}$ the reconstruction error increased almost linearly and then reached a plateau of 5 nm (all Zernike modes) and of 3.5 nm (Zernike modes 5-28), respectively (Fig. 2.3).

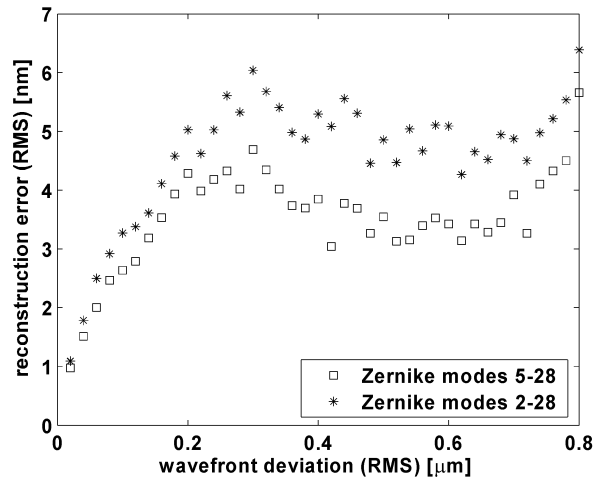


Fig. 2.3. Implementation-dependent reconstruction error for a vSHS using the centroid estimation as a function of wavefront deviation (RMS). The deviation was distributed uniformly over all Zernike modes.

The increase of the error for small wavefront deviations is due to the finite sampling of the diffraction pattern. Since the window (inside which the centroid is estimated) is centered on the pixel with the largest intensity in the diffraction pattern, it remains at the same position for a small (sub-pixel) change of the average wavefront tilt, while at the same time the diffraction pattern is slightly displaced. This causes an (sub-pixel) error for the centroid



estimation. Furthermore, since the derivatives of the Zernike modes, which were fitted to the wavefront gradients (see section 2.2.1), are not orthogonal, cross-talk between Zernike modes can occur, resulting in a systematic reconstruction error. The maximum error of about 5 nm ($\approx \lambda/200$) is, however, all but irrelevant in most situations, e.g. in the presence of photon or speckle noise (see below and section 2.4.3).

2.3.2 Photon-noise

Often the wavefront needs to be reconstructed when only a small number of backscattered photons is available. Then, photon shot noise is expected to be dominant since camera dark noise can be neglected if the reference beam is sufficiently intense (see below). In this section, speckle noise is neglected also and the effect of photon noise is considered in isolation.

Lauterbach et al. (2006) give as a lower boundary of the wavefront reconstruction error $\Delta\varphi$ (in μm , RMS) for electric fields calculated by the four-step PSI-algorithm

$$\Delta\varphi = \frac{\lambda}{2\pi\sqrt{2}} \left[\frac{M}{n_s} \left(1 + \frac{n_s}{n_r} + \frac{4n_c}{n_r} \right) \right]^{\frac{1}{2}}, \quad (2.9)$$

where n_r and n_s are the total photon numbers in the reference and sample arm for a quadruplet of interferograms, respectively, n_c is the camera dark noise, modeled as a Poisson process, and M is the number of (Zernike) modes used for the reconstruction. The error approaches an asymptotic lower (quantum) limit ($\Delta\varphi_\infty = \lambda\sqrt{M} / (2\pi\sqrt{2} n_s)$) for large numbers of reference arm photons, which depends on neither the reference arm intensity nor the camera dark noise.

The error in the local wavefront-tilt estimate of the SHS or the vSHS is proportional to the uncertainty of the centroid estimation, which scales as [Welsh et al., 1989]

$$\sigma \propto \frac{1}{d \cdot \sqrt{n_{\text{sublens}}}}, \quad (2.10)$$

where n_{sublens} is the number of photons passing through one sublens of diameter d . Note, that the width of the diffraction pattern and, thus, the uncertainty of the centroid estimation does not depend on the size of the aberration if the wavefront is sufficiently sampled by the sublenses. Even though the wavefront gradient for each sublens can be measured at the quantum limit, if the optimal centroid estimator is chosen [Thomas, 2004], the wavefront reconstruction error for the complete wavefront is not quantum limited and depends on the number of sublenses. For example, if the number of sublenses covering the aperture is increased by L^2 , the width of the diffraction pattern for each sublens increases by L and the number of photons decreases by a factor of $1/L^2$, together resulting in an increase in the centroid uncertainty for each sublens by a factor of L^2 ; averaging all sublens tilts reduces the error by $\sqrt{L^2} = L$, resulting in an increase in the total wavefront error by a factor L . This suggests the use of fewer sublenses, but then high-order aberrations might not be sufficiently sampled anymore and a systematic error is introduced.

By numerically simulating the four-step PSI algorithm, the reconstruction error of the vSHS due to photon noise was calculated. Two configurations for the vSHS were investigated: one with 148 sublenses (each 25 pixels wide) and the other with 441 sublenses (each 15 pixels wide), in both cases tiling the complete circular aperture. For each sublens the electric field was zero-padded to a field of 128x128 pixels before Fourier transforming. The window sizes for the centroid estimation were 20x20 and 35x35 pixels for the 148 and 441 sublens configurations, respectively.

To determine the reconstruction error 10 random wavefronts with a RMS deviation of 0.1 μm , distributed uniformly over all 28 Zernike modes, were generated. For each wavefront 10 quadruplets of interferograms with independent photon-noise distributions were calculated for a varying number of photons from the sample. The number of photons in the reference arm was 200 times higher than the number of photons from the sample to eliminate the dependence on the camera noise (see above).

It was found that down to photon numbers of about 10^4 the dependence of the reconstruction error on the number of photons is proportional to $1/\sqrt{n_s}$ (Fig. 2.4). For lower photon numbers wavefront reconstruction fails since the centroid estimation becomes erroneous for a fixed window size, which contains then not only the diffraction peak but also emerging side maxima due to photon noise. However, for



the lower number of sublenses measurement is still possible for a smaller number of photons. For photon numbers above 10^4 the ratios between the numerical calculated data and the quantum limit were 12.7 ± 1.8 and 24.2 ± 2.7 for the 148 and 441 sublenses, respectively, close to the expected values of 12.2 and 21.0. Thus, for these numbers of sublenses possible systematic errors due to sparse sampling of high-order aberrations can be neglected.

Further, it can be concluded that the described centroid estimation is close to the optimal estimator. For 28 Zernike modes 148 sublenses are sufficient for an accurate wavefront reconstruction.

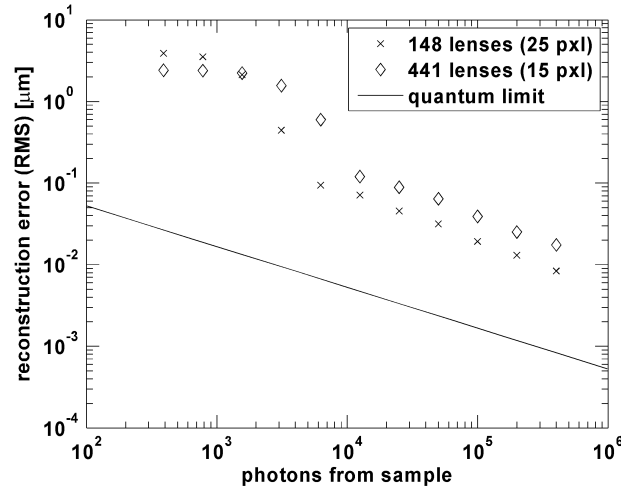


Fig. 2.4. Reconstruction error of the vSHS in the presence of photon noise for two different numbers of sublenses within a circular aperture. 28 Zernike modes were sensed and the generated wavefronts had a deviation of $0.1 \mu\text{m}$ (RMS).

The experimental investigation of the vSHS in terms of photon noise yields also information about other relevant noise sources that influence the wavefront measurement. Using the interference between light from the calibration and reference arms, the interference contrast

$$\Gamma = \frac{I''}{I'} \text{ with } I = I' + I'' \cos(\phi) \quad (2.11)$$

varies as the length of the reference arm is changed (I is the intensity of the interferogram per pixel and ϕ the phase to be measured). The quantum limit in

dependence on the interference contrast can be obtained by a transformation of $\Delta\varphi$ (Eq. (2.9)) into

$$\Delta\varphi_\gamma = \frac{\lambda}{2\pi\sqrt{2}} \sqrt{\frac{M}{(n_r + n_s)}} \frac{1}{\Gamma}. \quad (2.12)$$

Since the total energy detected for one interferogram was about 0.2 nJ ($n_r + n_s \approx 10^9$), the quantum limit was about $2 \cdot 10^{-5} \mu\text{m}/\Gamma$ (RMS).

The average reconstruction error for various interference contrasts was measured (Fig. 2.5) and the linear fit to the data confirmed the $1/\Gamma$ behavior (measured: $\Gamma^{-1.03}$). The proportionality factor was $6 \cdot 10^{-4}$, which was about 30 times higher than the quantum limit. This is roughly consistent to the factor of 21, which is theoretically expected due to photon noise for 441 sublenses used for the vSHS (see above). Thus, it can be concluded that experimentally the wavefront measurement is limited by photon noise and other noise sources like vibration of the interferometer can be neglected.

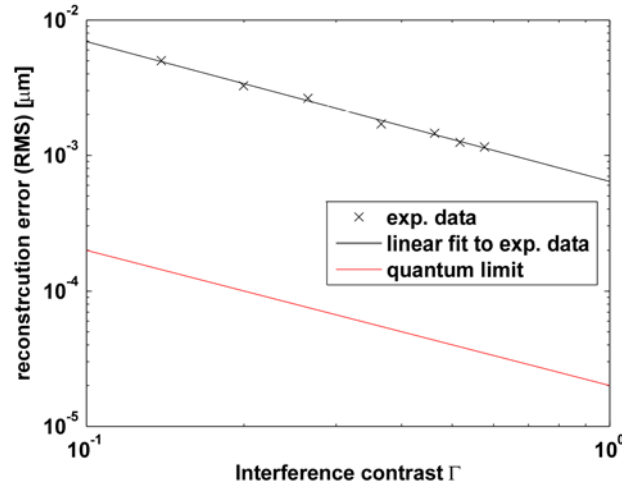


Fig. 2.5. The reconstruction error of the vSHS in relation to the interference contrast Γ using the calibration arm. For each data point the wavefront was measured 12 times using only one quadruplet for each wavefront measurement. From the variation between these, the reconstruction error was determined. A linear fit was used to obtain the slope and the proportionality factor of the reconstruction error, which was compared to the quantum limit (Eq. (2.12)).



As seen in Fig. 2.5, the measured interference contrast does not reach 100 %. In the ideal case when the lengths of the reference and the calibration arms are the same and all light contributes to the interference, the maximum interference contrast of 100 % is expected. However, since several back reflections from optical elements occur, the highest measured interference contrast was at about 60 %. For scattering phantoms (110 nm beads) the typical interference contrast was at about 20 % in a depth of 200 μm .

2.4 Characterization of the CGWS

Using theoretical investigations together with MCSs, the properties of the CGWS were comprehensively explored with respect to first-order and second-order speckle statistics. This section is restricted to situations where no aberrations in the optical path were considered. In a succeeding section the influence of aberrations on the CGWS will be investigated (see section 2.5).

2.4.1 Coherence volume

The main distinguishing characteristic of CGWS is its light-selection property. Mainly light scattered within a certain region of the focal cone, defined as the coherence volume (CV), is sensed by the CGWS. The CV depends on the width of the self coherence function and can, for example, be defined as the region where the self coherence weight of a scatterer's contribution is: $|\gamma(\tau(\mathbf{r}, \mathbf{w}))| > 0.5$. Since $\tau(\mathbf{r}, \mathbf{w})$ depends on the direction \mathbf{w} of the scattered light, the CV is differently shaped for different detection points (Fig. 2.6).

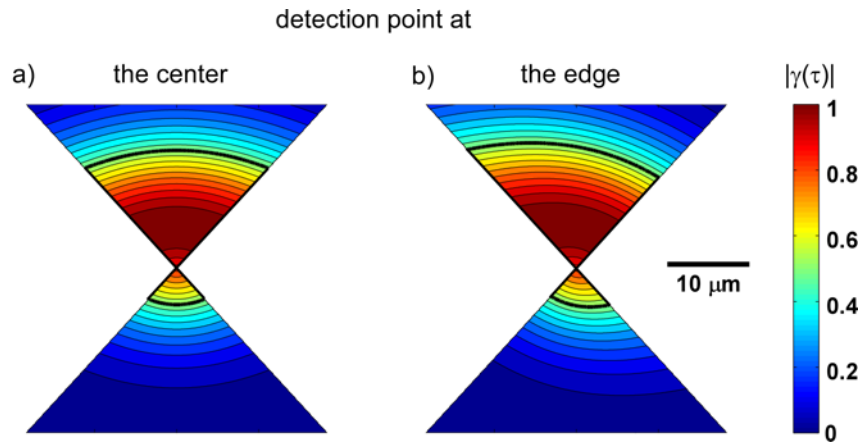
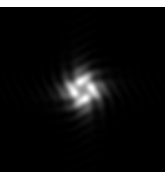


Fig. 2.6. The coherence volume, determined by the self coherence function $|\gamma(\tau)|$, shown as a cross-section through the focal cone along the optical axis. The detection points are at the center (a) and at the edge (b) of the back aperture of the objective. The black lines delineate the coherence volume ($|\gamma(\tau)| > 0.5$, see text). The coherence length used was 50 μm (FWHM), which corresponds to a CG length of 18.8 μm and the coherence-gate position was +5 μm .



2.4.2 Speckle characterization

Due to the temporal coherence of the coherence-gated backscattered light, the associated electric field is affected by speckle noise. Characterization of the first-order and second-order properties of speckle for CGWS-measured electric fields allows also the characterization of the measured wavefronts. At first, speckles are investigated analytically for special cases and, then, MCSs are employed to verify the analytical approach and, further, to characterize speckles and wavefronts of CGWS-measured electric fields for different coherence lengths, densities of scatterers, and coherence-gate positions. In the following it is assumed that the scatterers are uniformly distributed over the focal cone. Deviations from a uniform distribution will be discussed later (see section 2.7).

First-order statistical properties

For first-order statistics the contrast C is often used to characterize speckle [Goodman, 1976]. Two extreme cases can be distinguished: first, the speckles at each detection point are fully developed and show a contrast $C = 1$ and, second, no speckle occur at all and the contrast is $C = 0$. Whether the speckles are fully or partially developed is determined mainly by two parameters: the phase distribution $\phi = \omega \cdot \tau^{(k)}$ over all scatterers within the CV and the number of scatterers N (see below).

The speckle contrast, observed at the CGWS, can be analytically described if two assumptions for the scattering events are made: first, the amplitude of the backscattered light $A_s^{(k)}$ does not vary over the CV and, second, the phase distribution ϕ is a zero mean Gaussian distribution with standard deviation $\sigma_\phi = \pi / (\sqrt{2 \log 2}) \cdot l_c / \lambda \approx 0.85\pi \cdot l_c / \lambda$ over the interval $]-\pi; \pi]$. Although these simplifications are approximately fulfilled only for short coherence lengths l_c , the principle of speckle formation does not depend significantly on the exact function describing the phase distribution or the amplitude distribution [Goodman, 2005] and, thus, should be also valid for longer coherence lengths (see also MCSs in this section). For the given assumptions the contrast C in dependence of the number of scatterers N is [Goodman, 2005]

$$C = \frac{\sigma_I}{\langle I \rangle} = \frac{\sqrt{8N^2(1 - \frac{1}{N}) \cdot \exp(-2\sigma_\phi^2) \cdot [N - 1 + \cosh(\sigma_\phi^2)] \cdot \sinh^2(\frac{\sigma_\phi^2}{2})}}{N + N(N-1) \cdot \exp(-\sigma_\phi^2)}, \quad (2.13)$$

where the standard deviation and the mean of the intensity of the speckle is σ_I and $\langle I \rangle$, respectively. With an increasing number of scatterers N , the speckle contrast becomes fully developed, although the phase distribution for a certain σ_ϕ is not uniform (Fig. 2.7). If the second term for $\langle I \rangle$ begins to dominate ($\propto N^2$), which is the case for a sufficiently large number of scatterers (e.g., $> 10^4$ for $\sigma_\phi = 2\pi$, Fig. 2.7), the speckle contrast begins to fall again and converges towards zero, independently of σ_ϕ . This surprising dependence of the speckle contrast on the standard deviation and on the number of scatterers has been thoroughly studied in the literature [Fujii et al., 1974; Goodman, 1975; Uozumi et al., 1981; Apostol et al., 2005].

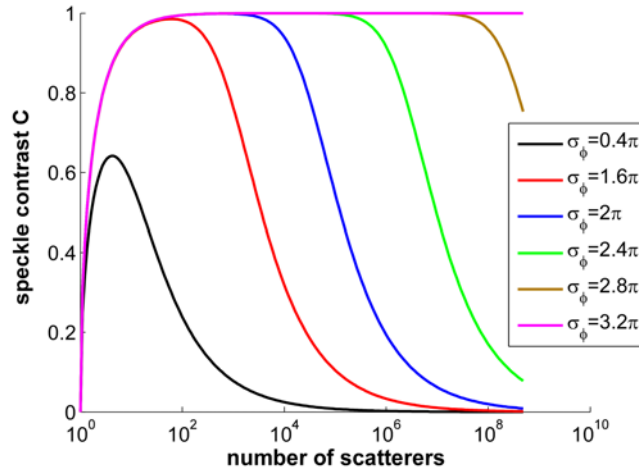
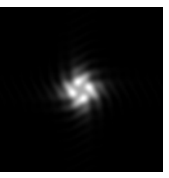


Fig. 2.7. Speckle contrast C vs. number of scatterers N , calculated by Eq. (2.13), for different widths σ_ϕ of a Gaussian phase distribution.

Applied to the speckle statistics for the CGWS, it can be concluded that for coherence lengths much larger than the wavelength ($\sigma_\phi \gg 2\pi$), the speckles are fully developed up to extremely high numbers of scatterers within the CV. Only for small coherence lengths, e.g. $l_c = 2\lambda$ ($\sigma_\phi \approx 1.7\pi$), partially developed speckle can be observed already



for numbers of scatterers at about 10^3 . Of course, an exception exists for very small numbers of scatterers (< 100), where the speckles are still partially developed, even for large coherence lengths (Fig. 2.7).

Second-order statistical properties

An investigation of the second-order statistics of the coherence-gated electric field with respect to the speckle contrast is required to determine the actual influence of speckle on the wavefront measurement. A common measure to characterize the second-order statistics is the ensemble-averaged complex degree of mutual coherence μ_{12} (spatial coherence, [Goodman, 2000]):

$$\mu_{12} = \frac{\langle E_1^{tot} E_2^{tot*} \rangle}{\sqrt{\langle |E_1^{tot}|^2 \rangle \langle |E_2^{tot}|^2 \rangle}}, \quad (2.14)$$

where the total electric fields E_1^{tot} and E_2^{tot} are measured at two different points, 1 and 2, respectively; the ensemble average is denoted by $\langle \rangle$. The width of the ensemble-averaged mutual coherence μ_{12} , also called spatial coherence length, is a measure for the characteristic grain size observed for an intensity speckle pattern [Klinger et al., 2001].

Since the coherence-gated electric field does not change with time, the time-averaged coherence γ_{12} (equal to the time-averaged complex degree of (self) coherence as described in section 2.1, but for two different points) is not reduced by the superposition of the backscattered light. However, the ensemble-averaged coherence μ_{12} is, in general, not equal to 1 (see below), indicating a lack of ergodicity.

The numerator \mathcal{G}_{12} of Eq. (2.14) can be modified to:

$$\begin{aligned}
 \mathcal{G}_{12} &= \langle E_1^{tot} E_2^{tot*} \rangle = \sum_k \langle E_1^{(k)} E_2^{(k)*} \rangle + \sum_m \sum_{n \neq m} \langle E_1^{(m)} E_2^{(n)*} \rangle \\
 &= \sum_k \langle E_1^{(k)} E_2^{(k)*} \rangle + \sum_m \sum_{n \neq m} \langle E_1^{(m)} \rangle \langle E_2^{(n)*} \rangle \\
 &= N \cdot \langle E_1 E_2^* \rangle + N(N-1) \cdot \langle E_1 \rangle \langle E_2^* \rangle \\
 &= N \cdot \alpha + N(N-1) \cdot \beta,
 \end{aligned} \tag{2.15}$$

where E_i ($i=1,2$) is the electric field due to a single scattering event at the detection point 1 or 2, respectively, and N is number of scatterers within the CV; α and β are parameters that depend on the coherence length, on the coherence gate, and on the two detection points. The second term of Eq. (2.15) begins to dominate if the number of scatterers is sufficiently high and, simultaneously, the speckle contrast falls towards zero (see above).

For the denominator η_{12} of Eq. (2.14) similar calculation steps yield

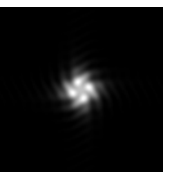
$$\eta_{12} = \sqrt{N \cdot \langle E_1 E_1^* \rangle + N(N-1) \cdot \langle E_1 \rangle \langle E_1^* \rangle} \sqrt{N \cdot \langle E_2 E_2^* \rangle + N(N-1) \cdot \langle E_2 \rangle \langle E_2^* \rangle}. \tag{2.16}$$

For a sufficiently large number of scatterers N so that the speckle contrast is close to zero, both \mathcal{G}_{12} and η_{12} scale as N^2 and the mutual coherence μ_{12} becomes

$$\mu_{12} \approx \exp(i\varphi_1) \cdot \exp(-i\varphi_2) \approx 1, \tag{2.17}$$

where $\varphi_i = \arg(\langle E_i \rangle)$ for $i=1,2$. Therefore, the modulus of μ_{12} is 1 and the phase should be approximately zero, since the phase distribution $\phi = \omega \cdot \tau^{(k)}$ (see above) at two different detection points is very similar (see also MCSs in this section) and, thus, also φ_1 and φ_2 .

If \mathcal{G}_{12} and η_{12} scale as N , $N > 100$ (see above), and the width of the phase distribution σ_ϕ is higher than π (Fig. 2.7), the speckles are fully developed. Then, by using Eq. (2.15) and (2.16) the mutual coherence μ_{12} is



$$\mu_{12} \approx \frac{\langle E_1 E_2^* \rangle}{\sqrt{\langle E_1 E_1^* \rangle} \sqrt{\langle E_2 E_2^* \rangle}}. \quad (2.18)$$

Using the Cauchy-Schwarz inequality, the mutual coherence is $|\mu_{12}| \leq 1$ and approaches zero with increasing distance between the two detection points. The width of the mutual coherence μ_{12} depends only on the lateral extent of the CV (see spatial coherence, e.g., in [Goodman, 2000]). The larger the lateral size of the CV is the shorter is the width of the mutual coherence μ_{12} .

The intensity of the diffraction patterns $I(r, q)$ of the vSHS (Eq. (2.7)) is given by

$$\langle I(r, q) \rangle = \mathcal{F} \left\{ \int_{-\infty}^{+\infty} \int_{-\infty}^{+\infty} \mathcal{G}(\varepsilon, \eta; u - \varepsilon, v - \eta) d\varepsilon d\eta \right\}, \quad (2.19)$$

where \mathcal{F} denotes the Fourier transformation (from the back focal plane of the objective, parameterized by u and v , to the detection plane of the sublenses, parameterized by r and q); $\mathcal{G}(\varepsilon, \eta; u - \varepsilon, v - \eta)$ is equal to \mathcal{G}_{12} for detection point 1 at (ε, η) and point 2 at $(u - \varepsilon, v - \eta)$ in the back aperture. The aperture function for a sublens is included in \mathcal{G}_{12} .

Using Eq. (2.15) the contribution of the incoherent and coherent terms to the diffraction patterns of the vSHS (Eq. (2.7)), the CGWS-measured wavefront can be quantified as follows. The first term in Eq. (2.7) is determined by the Fourier transformation of the first term of Eq. (2.15) and accordingly for the second term. Therefore, the ensemble average of the intensity of the incoherent and coherent superposition for the diffraction patterns scales as N and N^2 , respectively. Thus, for fully developed speckle the coherent superposition can be neglected and the incoherent superposition determines the shape of the CGWS-measured wavefront. If the number of scatterers is sufficiently large so that the speckle contrast decreases, the intensity of the coherent superposition increases with N^2 and exceeds that of the incoherent superposition. In the limit of zero speckle contrast, the intensity of the coherent superposition determines completely the wavefront. In this case, the CGWS-

measured wavefront will be almost flat, since the mutual coherence μ_{12} across the complete aperture becomes ≈ 1 .

In the limit of a very small number of scatterers (<100 , see Fig. 2.7), the speckles are far from fully developed irrespective of the coherence length. However, the diffraction patterns are dominated by the intensity of the incoherent superposition since the second term of Eq. (2.15) is still very small.

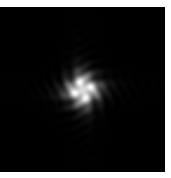
Monte-Carlo simulation (MCS)

Although the speckle statistics could be derived analytically for special cases of the speckle contrast, a MCS allows the investigation of the CGWS-measured wavefronts for an almost complete parameter space, e.g. for the coherence length and for the density (number) of scatterers within the CV. Since the effects due to speckle can be studied if only the Zernike defocus c_4 of the wavefronts is investigated (see below), here, the MCSs are restricted to cases where the optical path is aberration-free.

First, the influence of the coherent superposition of the backscattered light on the wavefront is demonstrated. Therefore, MCSs were implemented where fully developed speckle became partially developed when the number of scatterers was increased. However, it is computationally very expensive to use long coherence lengths ($\gg \lambda$), since then an extremely high number of scatterers would be needed to show this effect (see first-order speckle statistics). Instead, coherence lengths comparable to the wavelength were studied although coherence lengths smaller than the wavelength are physically not realizable. However, from a mathematical point of view these simulations can verify the analytical approach (see above) that is not restricted only to long coherence lengths. Further, the results for coherence lengths comparable to the wavelength should be transferable to longer coherence lengths as the analytical approach predicts.

For the physically impossible case of an infinitesimal short coherence length, at finite wavelength, the phase distribution is equal to a delta distribution and so is the same for all detection points, i.e. the CGWS-measured wavefront is flat, independent of the density of scatterers.

The MCSs, investigated in relation to the speckle contrast, showed the expected behavior: with increasing coherence lengths the density of scatterers needed to



observe the transition to partially developed speckle increased also (Fig. 2.8a). For a coherence length of $1.5 \mu\text{m}$ up to a density of scatterers of $1000 \mu\text{m}^{-3}$ the speckle contrast remains 1. However, this is true only for a Gaussian shape of the self coherence function. For a different shape, such as a rectangular function, the transition in speckle contrast can be observed for a lower density of scatterers (data not shown).

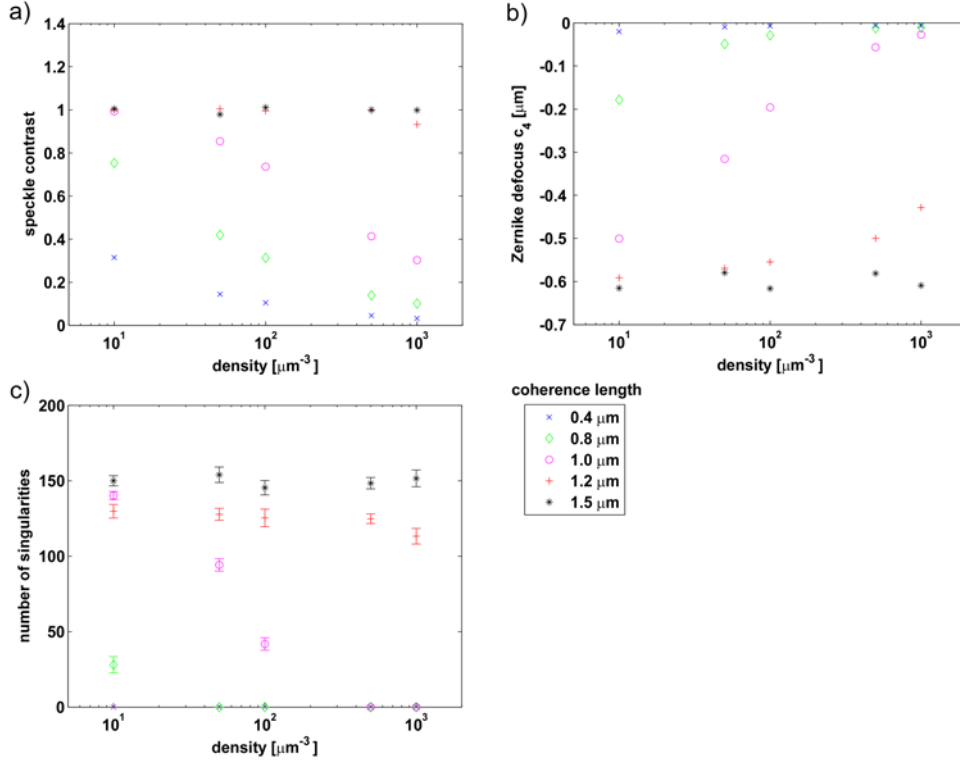


Fig. 2.8. Coherent effects on the CGWS-measured wavefront due to the transition of the speckle contrast towards zero. MCSs investigated the speckle contrast (a), the Zernike defocus c_4 (b), and the number of singularities (c) in dependence on the density of scatterers for 5 short coherence lengths ($0.4 \mu\text{m}$ to $1.5 \mu\text{m}$) and a CG position of $+5 \mu\text{m}$. The mean relative error for c_4 and for the speckle contrast was about 3% and 1%, respectively. The wavelength of the light was $1 \mu\text{m}$.

As predicted by the analytical approach, if the speckles become partially developed, the wavefront converges towards a flat wavefront, i.e. the Zernike defocus c_4 tends to zero (Fig. 2.8b). To quantify also the degree of spatial coherence of the CGWS-measured electric field, the number of phase singularities [Fried, 1998] for the intensity of the coherence-gated electric field was determined. The number of

singularities scales inversely with the speckle size [Shvartsman et al., 1994], which is proportional to the width of the mutual coherence (see above). Therefore, a low (high) number of singularities indicate a long (short) spatial coherence length. The MCSs showed that if the Zernike defocus converges to zero, simultaneously, the number of singularities converge to zero (Fig. 2.8c), otherwise not. Thus, if the speckles are fully developed, the number of singularities remains constant with an increasing number of scatterers (see below). At the transition to partially developed speckle the number of singularities starts to decrease and the spatial coherence raises.

For longer coherence lengths ($\gg \lambda$) the transition to partially developed speckle was not observable. For coherence lengths of about 50 μm , as they are typical for our experiments, MCSs showed that coherent effects are undetectable, even for as much as 60000 scatterers per μm^3 . In conclusion, the MCSs for short coherence lengths confirmed the analytical approach and demonstrated the coherent effects as predicted.

For a coherence length of 30 μm the CGWS-measured wavefronts were investigated by MCSs in terms of CG position and density of scatterers. Furthermore, MCSs were implemented for different coherence lengths varied from 2 μm to 30 μm (Fig. 2.9). For the investigated parameter space the speckles were always fully developed (data not shown). For fully developed speckle the number of singularities depends on the solid angle under which the scatterers within the CV are seen from the detector (see above). Thus, the lateral size of the CV, which is determined by the coherence length and the CG position but not by the number of scatterers, affect the number of singularities (Figs. 2.9a,c,e). Therefore, when the CG position approaches the focus or when the coherence length is shortened, the lateral extent of the CV reduces and the number of singularities decreases.

The wavefront was determined either by the peak or by the centroid estimation applied to the diffraction patterns [Larichev et al., 2001]. The Zernike defocus c_4 determined by centroid estimation remained constant if the coherence length or the density of scatterers were altered (Fig. 2.9d,f). Interestingly, the defocus determined by the peak estimation was always smaller than that of the centroid estimation. This is due to the fact that the speckle-averaged diffraction patterns, in particular for outer sublenses, are asymmetric (Fig. 2.10), presumably due to broadened point-spread functions for scatterers far away from the focus. Therefore, the centroid and the peak of the diffraction pattern diverge more for higher CG positions and longer coherence



lengths (Fig. 2.9b,d). However, if the density of scatterers is varied, the difference in Zernike defocus for both estimations remained constant.

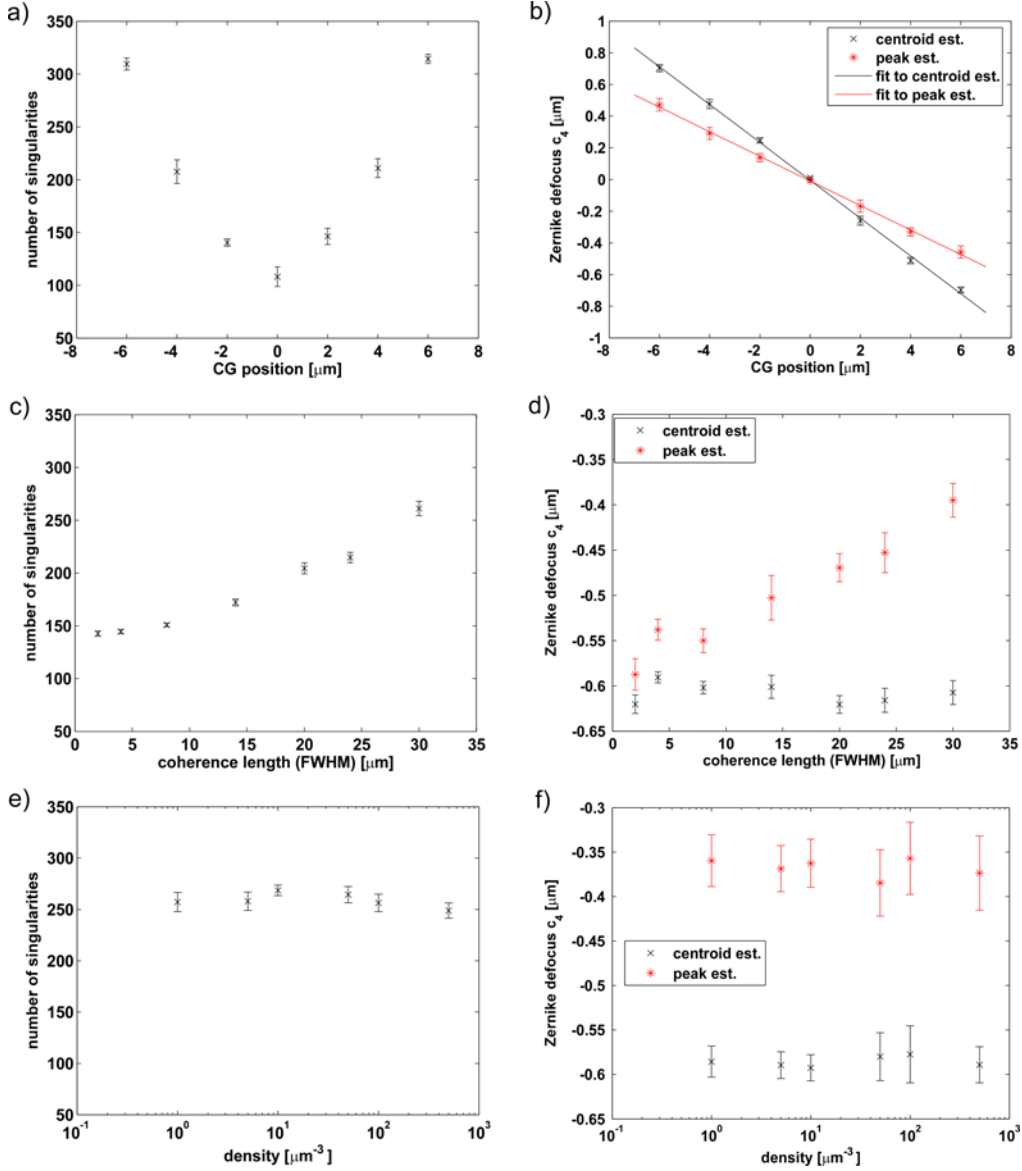


Fig. 2.9. CGWS-measured Zernike defocus c_4 and the number of singularities on the wavefront for different parameters. The number of singularities (a, c, e) and the Zernike defocus c_4 (b, d, f) is depicted in dependence on CG position, coherence length, and density of scatterers. The Zernike defocus c_4 was determined either by estimating the centroid or by fitting the peak by a Gaussian distribution. When not varied, the CG position, the density of scatterers, and the coherence length were $+5 \mu\text{m}$, $100 \mu\text{m}^{-3}$, and $30 \mu\text{m}$ (FWHM), respectively.

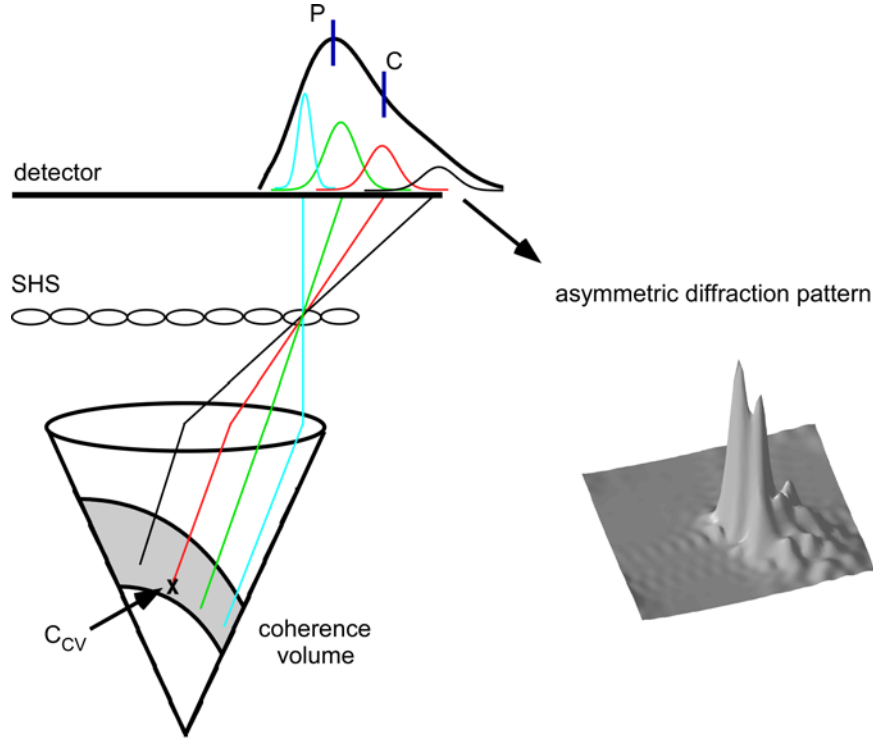


Fig. 2.10. Asymmetric diffraction pattern for a sublens of the vSHS located off the optical axis. The ray originating from the centroid C_{CV} of the coherence volume (delineated by the black lines) determines the centroid of the diffraction pattern. Peak (P) and centroid (C) estimation of the diffraction pattern differ. On the right hand side a typical asymmetric diffraction pattern, numerically calculated and already averaged over speckle noise, is shown. Note that the coherence volume is oversized compared to the focal cone.

For the centroid estimation the change of Zernike defocus per $1 \mu\text{m}$ displacement of the CG position was $-0.119 \pm 0.002 \mu\text{m}/\mu\text{m}$, whereas the slope of defocus was $-0.078 \pm 0.003 \mu\text{m}/\mu\text{m}$ if the peak was estimated. The defocus slope calculated for a single scatterer located at the CG position on the optical axis is $-0.102 \mu\text{m}/\mu\text{m}$ and lies between the measured slopes for centroid and peak estimation. The higher value for the centroid estimation is due to the fact that the centroid of the CV, weighted by the intensity distribution $1/z^2$, is displaced laterally compared to the CG position for sublenses located off the optical axis (Fig. 2.11). For a sublens of the vSHS close to the optical axis the displacement is small, whereas sublenses near the edge of the aperture see a significant displacement, leading to a higher Zernike defocus for a collection of scatterers within the CV.

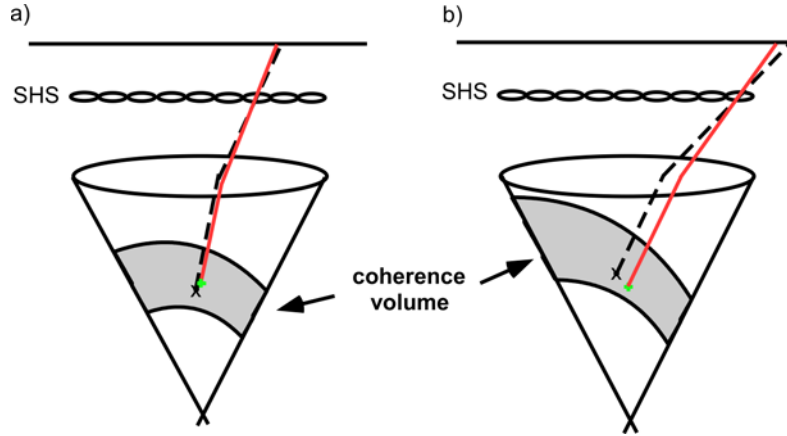
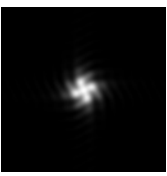


Fig. 2.11. Average wavefront tilt for a single scatterer at the center of the CG position (on the optical axis, green point) and for a collection of scatterers uniformly distributed across the CV for sublenses close to the optical axis (a) and near the edge of the aperture (b). The average wavefront tilt for a collection of particles can be represented by the ray coming from the centroid of the CV (black cross). Note that the CV is oversized compared to the focal cone.

The defocus slope for the centroid estimation (obtained by MCS) is in good agreement to experimental measurements, which were $-0.117 \pm 0.001 \mu\text{m}/\mu\text{m}$ and $-0.101 \pm 0.001 \mu\text{m}/\mu\text{m}$ for a scattering phantom containing 110 nm scattering beads and for a fixed hippocampus slice, respectively (Fig. 2.12). In conclusion, the centroid estimation is independent on the degree of asymmetry of the diffraction patterns, in contrast to the peak estimation (Fig. 2.9d). Therefore centroid estimation was generally used.

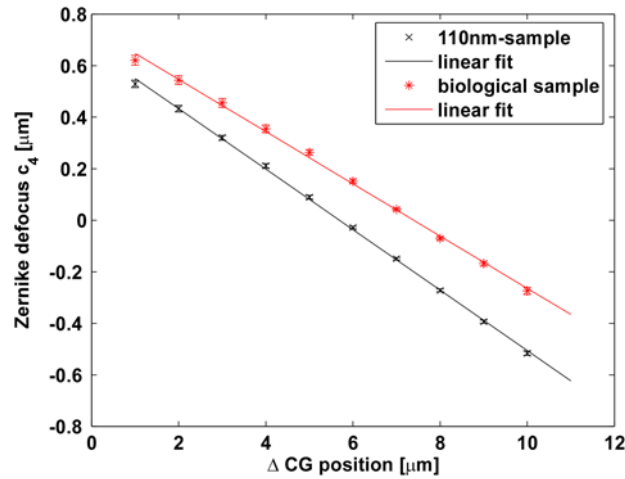


Fig. 2.12. Experimentally measured change of the Zernike defocus c_4 as a function of the CG position for a scattering sample with 110 nm scattering beads (black) and for a fixed organotypic hippocampus slice (red). Since no absolute CG position was measured, the two data series are displaced.

2.4.3 Speckle averaging

When the speckle contrast for the CGWS is fully developed, then, the measured wavefront for a single ensemble of scatterers is significantly degraded by speckle noise, caused by the coherent superposition of the backscattered light (see Eq.(2.19)). Therefore, the wavefront needs to be averaged over a number M of independent ensembles of scatterers to obtain an accurate wavefront that is determined only by the incoherent superposition of the backscattered light. When the diffraction patterns of the vSHS are averaged over independent ensembles, the speckle (noise) contrast scales as $1/\sqrt{M}$ [Goodman, 2005]. The wavefront error should, therefore, scale similarly as σ_0/\sqrt{M} , where σ_0 is the proportionality constant, which depends on the speckle size (see below). To average speckle, almost uncorrelated speckle patterns are required. Experimentally, such uncorrelated speckle patterns can be obtained by displacing the focus within the sample, both axially and laterally. How large the correlation between speckle patterns of the coherence-gated electric field at different focus positions is, can be measured by cross-correlating the speckle patterns. For a lateral and an axial focus displacement the measured cross-correlations did not vanish for displacements of up to 2 μm and 3 μm , respectively, presumably since there was still substantial overlap of displaced CVs (Fig. 2.13).

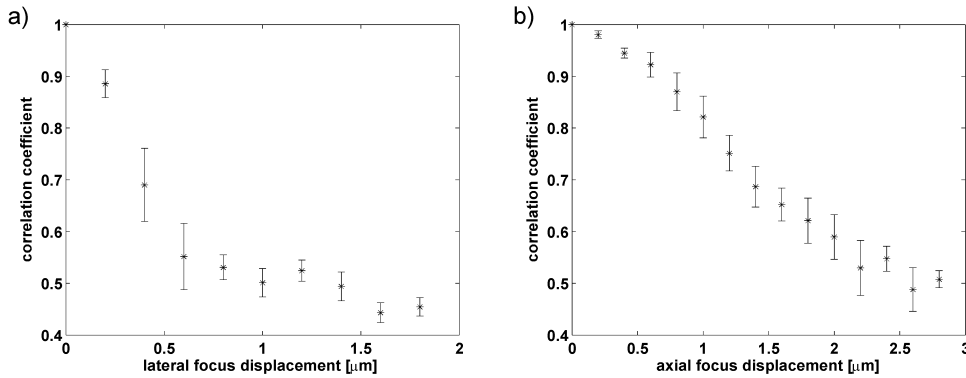
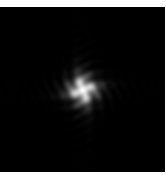


Fig. 2.13. Correlation coefficients for speckle patterns experimentally measured at different lateral (a) and axial (b) displacements of the focus within a scattering sample containing 110 nm beads.

The dependence of the wavefront error on M was verified experimentally as well as numerically by the MCS (Fig. 2.14). The linear fits to the logarithmic plots yielded



slopes of -0.53 and -0.52 for the numerical and experimental data, respectively, which were in good agreement with the expected value of -0.50.

Experimentally, the wavefront error after 20 averages was typically $\sigma_s \approx 0.02 \mu\text{m}$ and, therefore, $\sigma_0 = \sigma_s \cdot \sqrt{20} = 0.085 \mu\text{m}$ (RMS, calculated including Zernike mode 5 to 28 with data from Fig. 2.14). The numerical value for σ_0 was slightly higher ($\approx 0.11 \mu\text{m}$), since the speckle size was smaller for the chosen parameters (see caption of Fig. 2.14 and see below).

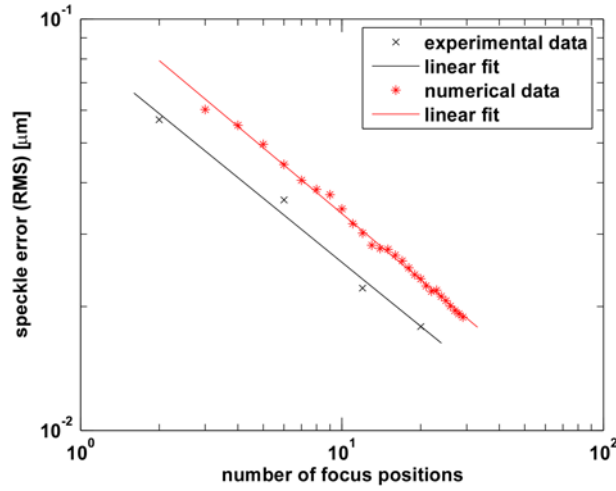


Fig. 2.14. Speckle error after speckle averaging over a number of focus positions (experimentally) and a number of independent ensembles (numerically). For the MCS a CG position of $+5 \mu\text{m}$, a density of scatterers of $100 \mu\text{m}^{-3}$, and a coherence length of $8 \mu\text{m}$ was chosen. For the experimental data the focus was laterally displaced on a grid with $1 \mu\text{m}$ spacing within a scattering sample containing 110 nm beads.

To determine the dependence of the proportionality constant σ_0 on the speckle size, speckled wavefronts were generated numerically by the superposition of spherical wavelets emitted from a random ensemble of point-sources confined to a certain volume. Due to the random locations of the point-sources, the detected intensity showed a typical speckle pattern with a characteristic grain size, which can be varied by changing the lateral size of the volume over which the point-sources are distributed. This variation of the grain size corresponds to a situation for CGWS where the coherence-gate position is displaced from the focal plane or where the coherence length is increased (see section 2.4.2). The volume of point-sources was chosen large enough to ensure that the speckles were fully developed. The average

speckle size was calculated by using the normalized auto-covariance function of the intensity speckle pattern [Piederriere et al., 2004]. The error due to speckle was determined using the RMS variation in the wavefront for different ensembles of point-sources. Photon noise was neglected.

It was found that σ_0 increases as the speckle size decreases (Fig. 2.15). This is due to the fact that if the speckle size and, thus, the spatial coherence length of the coherence-gated electric field becomes shorter, side maxima in the diffraction patterns will occur (see Eq. (2.19)). Thus, the centroid estimation error increases. This is in agreement with Larichev et al. (2001), who found a similar dependence of the speckle error on the speckle size for a real SHS.

If the sampling rate of the detector is less than two per speckle size (Nyquist rate), the wavefront can not be reconstructed anymore. However, since an imaging system is used for CGWS (not used for the numerical simulation here), the minimum achievable speckle size is given by the numerical aperture of this system and not by the lateral size of the CV.

Experimentally, the ratio for speckle size vs. size of sublens was about 0.8 for CG positions close to the focus, leading to a numerical value for σ_0 of about $0.08 \mu\text{m}$ (Fig. 2.15), which is in agreement to the experimentally measured value (see above).

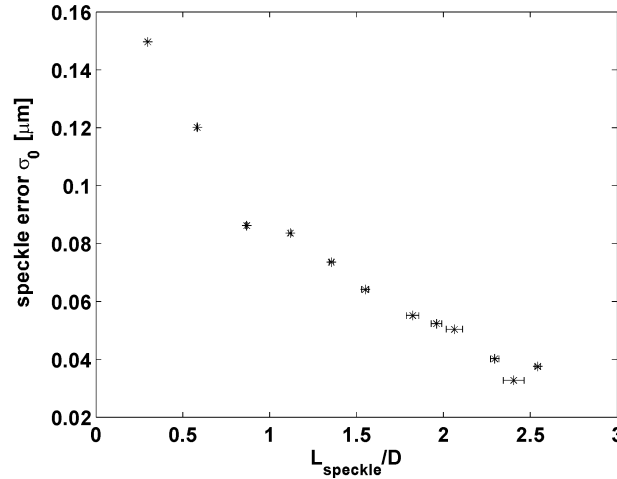
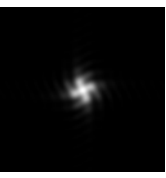


Fig. 2.15. The proportionality constant σ_0 as a function of the ratio between speckle size L_{speckle} and the size of a sublens D . The wavefront error was calculated over the Zernike modes 5 to 28 (corresponding to aberrations).



2.5 CGWS-measured wavefront aberrations

2.5.1 Influence of the speckle contrast on the measurement of aberrations

After having estimated the wavefront reconstruction error due to photon and speckle noise, now the question will be addressed whether aberrations are correctly sensed or whether, for example, a bias exists that depends on aberration size. This is particularly important when CGWS is to be used as the sensor in an adaptive wavefront correcting system. Such systematic bias might occur, for example, because the light encounters the aberrations in the sample arm twice, on the way to the focus and on the way back. For the preemptive correction of wavefront distortions the information about aberrations on the way to the focus is needed. The behavior of the CGWS depends strongly on the sample properties: if the sample acts like a mirror, aberrations with an even symmetry, such as astigmatism or defocus appear twice as large in double pass than single pass, whereas odd aberrations, such as coma cancel and cannot be detected at all; if the sample contains only a single scatterer, from which a spherical wavelet emanates, the aberrations of the illumination light are lost completely and only inhomogeneities encountered during back-propagation are seen. As a result, the single pass aberrations are correctly detected and due to the optical reciprocity theorem [Born et al., 1999] they are equal to the aberrations distorting the incoming light on the way to the focus. Therefore, CGWS needs to be investigated under which prerequisites single pass aberrations are correctly sensed if the illumination light is scattered back from multiple randomly distributed scatterers.

Distortions can be described in terms of how much they add to the time needed for the light to travel to the CGWS:

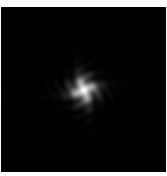
$$\tau_{aberr.}(\mathbf{r}, \mathbf{w}) = \tau(\mathbf{r}, \mathbf{w}) + \tau_{illum.}(\mathbf{r}) + \tau_{scatt.}(\mathbf{r}, \mathbf{w}), \quad (2.20)$$

where $\tau(\mathbf{r}, \mathbf{w})$ is the time calculated by Eq. (2.4), $\tau_{illum.}(\mathbf{r})$ and $\tau_{scatt.}(\mathbf{r}, \mathbf{w})$ are the times added to the incoming and back-propagating light, respectively, due to aberrations. Note that the shape of the CV will be distorted, albeit only little for typically aberrations, because it depends on the traveling time (Fig. 2.16a).

Again, attention needs to be paid to the degree to which speckles are developed, because (see preceding section) if the density of scatterers is sufficiently large and speckles become partially developed, the CGWS-measured wavefronts converges towards a flat wavefront. Although this fact was derived for the case where no aberrations are present, this is even true if aberrations affect the measured wavefront, since phases added by aberrations change only slightly the phase distribution ϕ (see section 2.4.2) of the coherence-gated backscattered light for a certain detection point. This fact is also easily apparent when the coherence length approaches zero: then only scattered light with exactly the same time traveled contributes to the CGWS-measured wavefront, i.e. the phase of the CGWS-selected light is invariant over the detector. Thus, the measured wavefront is flat. The shrunken CV is deformed in such a way that it compensates for the additional time introduced by the distortions.

This was verified by MCSs, where aberrations in the optical path (astigmatism: $c_6 = -0.3 \mu\text{m}$ and coma: $c_8 = -0.5 \mu\text{m}$) were inserted at the back focal plane of the objective (Fig. 2.16b). Below a coherence length of $2 \mu\text{m}$ the measured Zernike coefficients tended all towards zero and became indistinguishable from zero below a coherence length of $0.6 \mu\text{m}$. For coherence lengths higher than $2 \mu\text{m}$ the single-pass aberrations were correctly measured (with an accuracy limited by speckle noise). This can be explained by the fact that for these coherence lengths the speckles are fully developed and, thus, only the incoherent superposition of the backscattered light contributes to the wavefront (of course, after speckle averaging, see section 2.4.2). Therefore, all spherical wavelets emanating from the scatterers (Huygen's principle) can be assumed to be independent from each other and information about aberrations of the illumination light is lost. Of course, the intensity distribution near the focus is changed by aberrations, which might have a marginal effect on the backscattered light (this effect was not included in the MCS). However, experiments, which include this effect, confirmed that information about aberrations in the incoming light is completely lost (see below). In conclusion, only if the speckles are not fully developed, the measurement of aberrations can become biased.

To put it on a firm footing, also a MCS was performed where only the incoming light was distorted by aberrations (same distortions as above) and the path of the scattered light was aberration-free (Fig. 2.16c). Although this situation is experimentally not realizable, the simulation showed that aberrations of the incoming light were lost



completely, both if the speckles were partially and fully developed (accuracy limited by speckle noise). This confirms the argument from above that the CGWS-measured wavefronts are independent of the incoming wave-shape. However, the assumption of randomly distributed scatterers is essential, since, for example, the backscattered light from a sufficiently large number of scatterers in a single plane (as for a mirror) would not be insensitive to aberrations in the incoming light path.

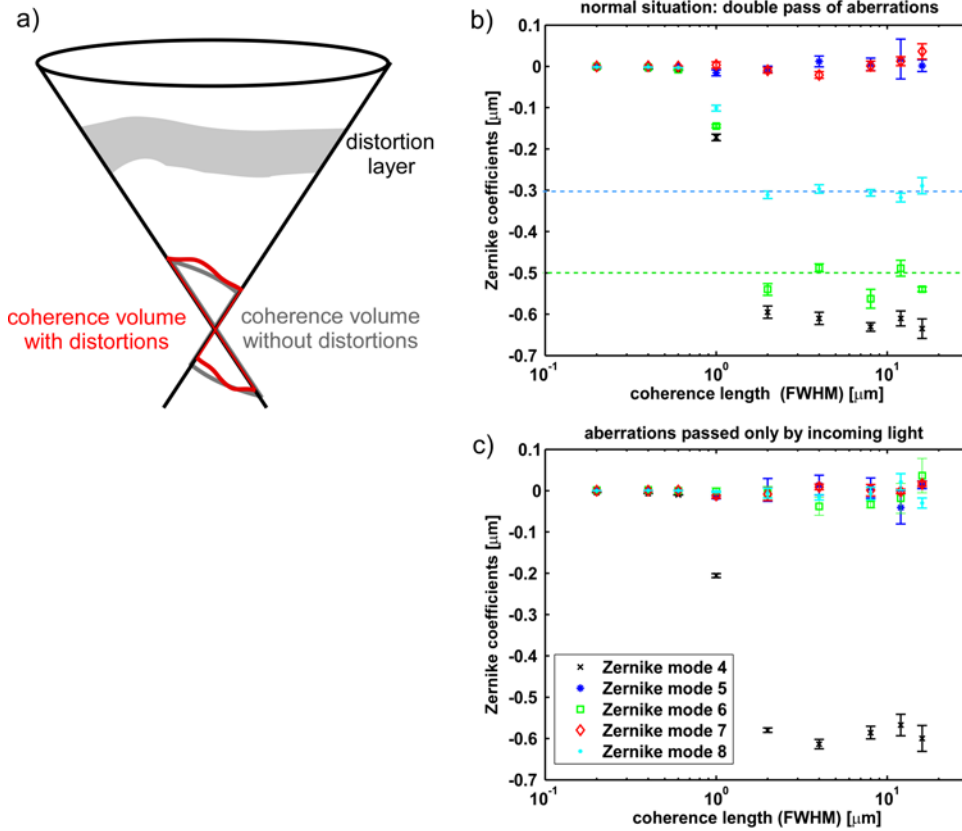


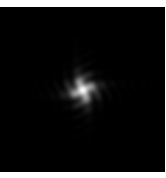
Fig. 2.16. Monte-Carlo simulations showing the influence of aberrations on the CGWS-measurement process. Illustration (a) of how the coherence volume is deformed by aberrations. The measured aberrations (and Zernike defocus) in dependence on the coherence length were sensed by both the incoming and the backscattered light (b). To verify that aberrations of the illumination light are lost, MCSs was generated for a physically not possible situation where only the illumination light passes through the distortions (c). The blue and green dotted lines in (b) show the expected aberrations due to a single pass of a phaseplate with Zernike modes 6 ($c_6 = -0.5 \mu\text{m}$) and 8 ($c_8 = -0.3 \mu\text{m}$), located in the back focal plane of the objective. The legend in (c) is valid also for (b). The density of scatterers was $100 \mu\text{m}^{-3}$ (homogeneous distribution) and the CG was placed at $+5 \mu\text{m}$. To reduce speckle noise up to 5 ensembles were generated for each coherence length.

The influence of aberrations on CGWS was also tested experimentally where only the regime of fully developed speckle was experimentally accessible (coherence length of 51 μm , see section 2.2.1). Using a scattering sample (containing 110 nm beads) the incoming wavefronts were varied (by at most 0.35 μm , RMS) using the deformable mirror. The variation in the CGWS-measured wavefronts (after, of course, correcting for the influence of the deformable mirror on the back-propagating wavefront) was 0.017 μm , as large as the error expected from speckle noise, thus, indicating this to be the only significant error source.

So far, only actual aberrations (Zernike modes higher than 5) were considered, but can the remaining Zernike modes like tip, tilt, and defocus also be measured? In contrast to the other Zernike modes, tip/tilt and defocus produce only a displacement of the focus within the specimen without changing the shape of it. However, a varying displacement within the specimen can cause unwanted geometric distortions in the acquired images. To correct also for these distortions, information about the focus displacement is required. However, in an episcopic illumination scheme focus displacements due to tip/tilt can not be sensed [Booth et al., 2005], since a conjugate displacement is introduced on the way back to the objective. A special case occurs if only a single scatterer is present in the focal cone. Then, tip/tilt changes can be measured since the light is scattered back always from the same point. In general, an axial displacement of the focus due to an introduced defocus in the optical path can also not be detected for an episcopic arrangement [Booth et al., 2005]. However, since CGWS is sensitive to the time needed for the scattered light to travel to the detector, an axial focus displacement should be measurable.

2.5.2 Aberrations due to a tilted glass-plate

A further verification that CGWS provides the true distortions is based on the measurement of aberrations due to a tilted glass-plate (thickness 145 μm , 10° tilt angle, BK7) inserted between scattering sample and objective. To model this situation realistically, the additional time delays for the illumination and the scattered light due



to refraction at the glass interfaces need to be taken into account (Fig. 2.17). The time delay for the illumination light is

$$\begin{aligned}\tau_{illum.} &= \frac{1}{c}(n_G \cdot L_G - n_W \cdot L_W) \\ &= \frac{1}{c} \left(\frac{n_G \cdot D}{\cos(\beta)} - \frac{n_W \cdot D}{\cos(\beta)} \cos(\alpha - \beta) \right),\end{aligned}\quad (2.21)$$

where c is the velocity of light in vacuum, n_G and n_W are the refractive indices of glass (BK7, $n_G=1.51$) and water, respectively, and D is the thickness of the glass-plate. The length L_G and L_W are indicated in Fig. 2.17. Snell's law relates the angle of refraction β to the incident angle α (angle between \mathbf{v} and \mathbf{n}).

The displacement \mathbf{p} (Fig. 2.17) of the incident light ray after it has been refracted twice at the glass interface is

$$\mathbf{p} = -\frac{D \sin(\alpha - \beta)}{\cos(\beta) \sin(\alpha)} \mathbf{n} + \frac{D}{\cos(\beta)} \left(-\frac{\sin(\beta)}{\sin(\alpha)} + \cos(\alpha - \beta) \right) \mathbf{v}, \quad (2.22)$$

using straightforward geometrical considerations. Note, that \mathbf{p} lies in the plane defined by the vector \mathbf{n} that is normal to the glass-plate and the vector \mathbf{v} pointing along the incident light ray.

Since the refraction of a transmitted light ray by the plate does not depend on the position of the plate, the time delay for the scattered light $\tau_{scatt.}$ depends only on \mathbf{w} (Fig. 2.17) and can be calculated as $\tau_{illum.}$ in Eq. (2.21) by replacing the incident angle α by the angle between \mathbf{w} and \mathbf{n} . This also means that a displacement of the CG position will not change the measured aberrations. Exceptions are all rotationally symmetric aberrations like Zernike mode 4 (defocus) or Zernike mode 11 (spherical aberration 1th order), which vary with CG position also when no aberrations are present. This can be easily seen when a spherical wavefront, sent out by a point-source located on the optical axis in a distance d to the focus, is traced through the objective lens to the back focal plane. Using the sine condition [Born et al., 1999] for a generic objective lens, it can be shown with straightforward geometrical considerations that the wavefront gradient at the back focal plane is

$$\frac{dW}{dr} \propto \frac{2d}{f} \tan\left(\arcsin\left(\frac{r}{nf}\right)\right), \quad (2.23)$$

where r is the radial coordinate parameterizing the back focal plane, f is the focal length, and n is the refractive index of the immersion medium. Since the wavefront gradient does not only depend on the lowest order of r if the term in Eq. (2.23) is expanded in a Taylor series, also spherical aberration changes with an axial displacement of the focus or with a change of the CG position.

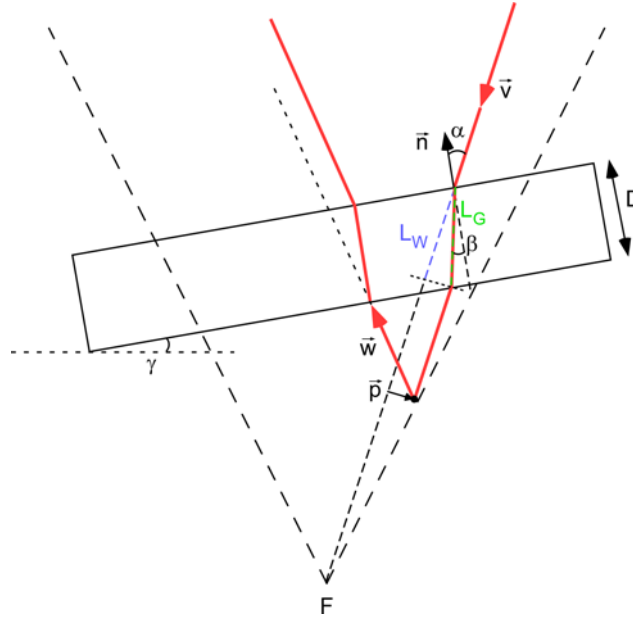
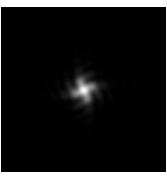


Fig. 2.17. Time delays caused by a tilted glass-plate (tilt angle γ , thickness D , normal vector \mathbf{n}) in the incoming and the scattered light, whose directions are denoted by \mathbf{v} and \mathbf{w} , respectively. The angles of incident and refracted rays are described by α and β , respectively. The displacement of the incoming light by the glass-plate is denoted by \mathbf{p} .

The additional time delays due to the glass-plate were incorporated in the MCS. The aberrations found were mainly Zernike mode c_6 (astigmatism), c_8 (coma), and c_{11} (spherical aberration). As expected, astigmatism and coma remains constant when the CG position was varied (Fig. 2.18a). Deviations are due to speckle noise, which was at about $0.01 \mu\text{m}$. If averaged over all shown CG positions, Zernike mode c_6 and c_8 were $0.10 \pm 0.02 \mu\text{m}$ and $0.22 \pm 0.01 \mu\text{m}$. The Zernike mode for spherical aberration c_{11} changed linearly with a slope of $-0.006 \mu\text{m}/\mu\text{m}$ for each $1 \mu\text{m}$ change in CG position



(see above) as did the Zernike defocus c_4 (slope of $-0.11 \mu\text{m}/\mu\text{m}$); the value for c_{11} if the CG is at the focus was $0.167 \pm 0.005 \mu\text{m}$. No other aberrations (except for tip/tilt) were seen, with modes up to c_{11} tested.

Using a scattering sample with 110 nm beads (see section 2.2.1), the experimentally measured aberrations for a tilted glass-plate averaged over all measured CG positions were (Fig. 2.18b): $c_6 = 0.09 \pm 0.02 \mu\text{m}$ and $c_8 = 0.23 \pm 0.01 \mu\text{m}$. The spherical aberration at a CG position near the focus was $c_{11} = 0.12 \pm 0.01 \mu\text{m}$. The slope of the Zernike defocus c_4 was $-0.12 \mu\text{m}/\mu\text{m}$ and that for spherical aberration (c_{11}) $-0.004 \mu\text{m}/\mu\text{m}$. These slopes are in good agreement with those found with the MCS; only for the value of spherical aberration the deviation is higher, probably due to additional spherical aberration caused by the interface between scattering sample and water (immersion medium). Experimentally, astigmatism changed slightly with CG position, possibly due to deviations from the circular polarization of the illumination light (see section 2.6).

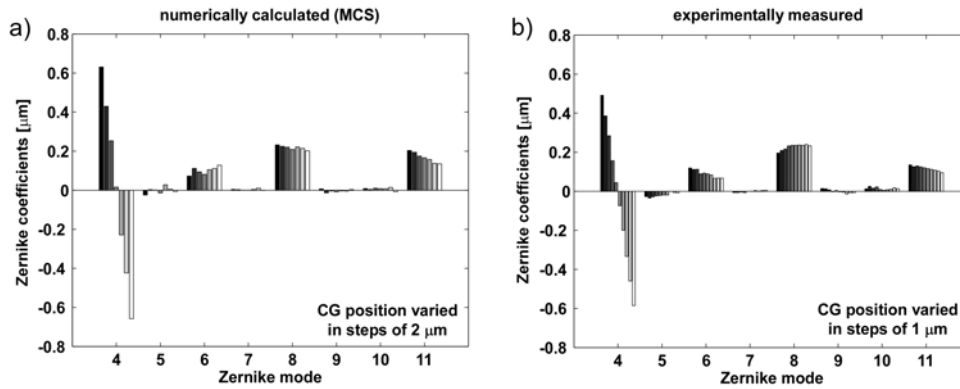


Fig. 2.18. Aberrations due to a tilted glass-plate (10° -tilted, $145 \mu\text{m}$ thick) measured by a MCS (a) for a coherence length of $6 \mu\text{m}$ and a density of scatterers of $1 \mu\text{m}^{-3}$. Experimentally measured aberrations (b) for the tilted glass-plate with the same parameters. The differently gray-scaled bars indicate different CG positions, which were varied in steps of $2 \mu\text{m}$ and $1 \mu\text{m}$ for the MCS and the experiment, respectively.

2.5.3 Aberrations close to focus

At the beginning of section 2.5 the influence of aberrations, introduced at the back focal plane of the objective, on the CGWS-measured wavefront was investigated by MCSs. Here, the influence of distortion layers close to the focus will be explored, which might introduce a bias on the measured wavefront.

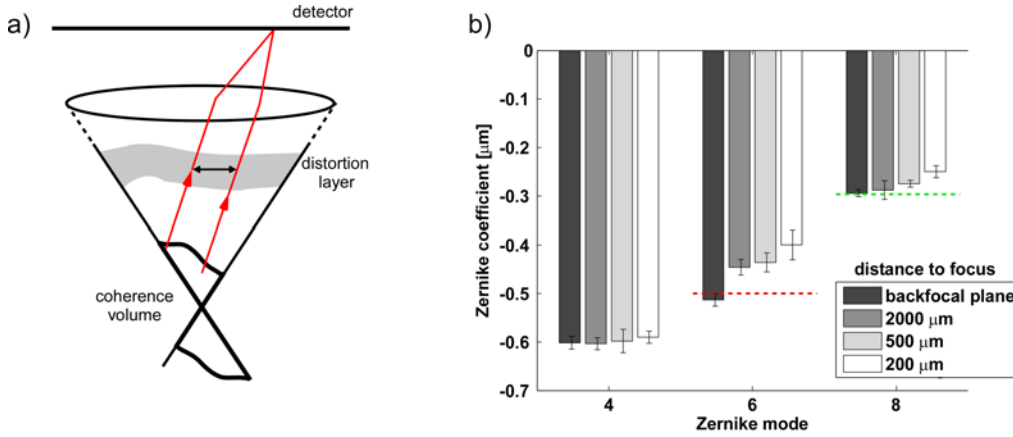
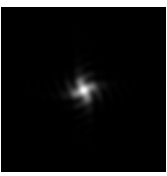


Fig. 2.19. Dependence of the CGWS-measured aberrations on the location of the distortion layer using MCSs. Illustration (a) of how, due to the lateral extent of the coherence volume, aberrations are averaged when located close to the focus. Measured Zernike modes (b) for a phaseplate with $c_6 = -0.5 \mu\text{m}$ and $c_8 = -0.3 \mu\text{m}$ located at various distances to the focus (indicated by the gray scale). The CG position was at $+5 \mu\text{m}$ and the coherence length was $6 \mu\text{m}$ (FWHM). The measured Zernike modes were averaged over different densities of scatterers of 1, 10, 50, 100, $500 \mu\text{m}^{-3}$ since no variations were observed (for all fully developed speckle). Other Zernike modes were not detected. The red and green dotted lines indicate the expected single-pass aberrations for the Zernike mode 6 and 8, respectively.

Due to the lateral extent of the CV, light scattered in the same direction but at different locations senses different parts of the distortions, resulting in spatial averaging of the aberrations (Fig. 2.19a). Therefore, MCSs with a phaseplate ($c_6 = -0.5 \mu\text{m}$ and $c_8 = -0.3 \mu\text{m}$) located at various distances above the focus were implemented. The phaseplates were confined only to within the focal cone with the same Zernike coefficients, thus, phaseplates close to the focus contained aberrations with higher frequencies than phaseplates further away. Such phaseplates were chosen since a single scatterer at the focus would measure always the same aberrations independent



of the location of the phaseplate. However, this is unlike the situation encountered in a real specimen where aberrations do not get confined when they come closer to the focus but also in this situation a spatial averaging effect is expected.

The MCSs showed that the correct aberrations were measured only when the phaseplate was located in the back focal plane, but as the aberrations came closer to the focus the measured values declined (Fig. 2.19b). This is due to the fact that the averaging effect due to the lateral extent of the CV is enhanced if the aberrations come closer to the focus, since then the aberrations get more confined.

However, the bias of the measured wavefronts should be reducible if the wavefront is measured not in a conjugate plane to the back focal plane of the objective but in a conjugate plane to the distortion layer within the sample. Further, if several distortion layers are present the principle of multi-conjugated adaptive optics can be applied [Beckers, 1988].

2.6 Polarization effects on CGWS

The phase and the amplitude of coherence-gated backscattered light is not only affected by the self coherence function $\gamma(\tau^{(k)}(u, v))$ and the intensity distribution across the focal cone $A_S^{(k)}(u, v)$ but also by the polarization-dependent scattering of the incoming light $W_{Pol}^{(k)}(u, v)$ (see Eq. (2.6)). The rigorous theory of Mie scattering [Mie, 1908], which is valid for all spherical scatterers, provides polarization resolved amplitudes and phase delays for all scattering angles. Here, the dependence of the CGWS-measured wavefronts on the polarization of the incoming and the reference light is investigated [Rueckel et al., 2005].

The first optical setup for CGWS [Feierabend et al., 2004] was based on linearly polarized light to illuminate the sample. Two different scattering phantoms (beads with either 110 nm or 1 μm diameter, see section 2.2.1) with distinct polarization-dependent scattering properties (see below) were used to measure wavefronts by CGWS. By changing the CG position, it was observed for the 1 μm diameter beads that not only the Zernike defocus but also astigmatism (Zernike mode 6) changed linearly (Fig. 2.20b). The slope for c_6 was measured as $+0.037 \pm 0.003 \mu\text{m}/\mu\text{m}$. Since no aberrations were introduced, the measured astigmatism was spurious. For the smaller beads of 110 nm diameter also spurious astigmatism occurred but with a lower slope of $+0.008 \pm 0.003 \mu\text{m}/\mu\text{m}$ (Fig. 2.20a). Other varying Zernike modes, such as mode 11 (spherical aberration), could not be detected.

The occurrence of spurious astigmatism can be illustrated by using the model derived in section 2.4.2 for fully developed speckle. Thereby, independent spherical wavelets emanate from the CV and the incoherent superposition forms the speckle-averaged wavefront. Due to scattering, different phase delays for different scattering angles can cause aberrated spherical wavelets (Fig. 2.21a,b). As MCSs showed (see below), these aberrations can be neglected and are not responsible for the occurrence of spurious astigmatism. In particular, this is obvious for scatterers small compared to the wavelength (Rayleigh scatterers). In this case the phase delays are almost constant for the relevant scattering angles, which are determined by the acceptance cone of the

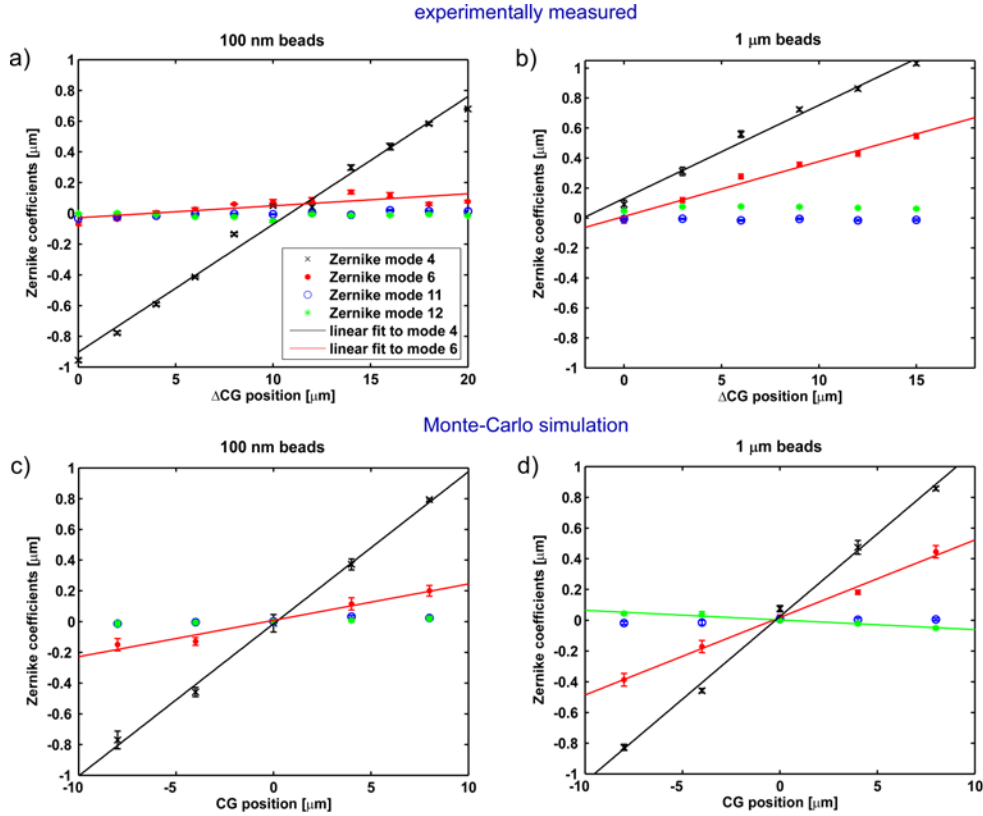
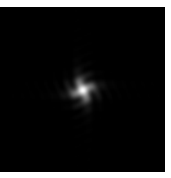


Fig. 2.20. CGWS-measured wavefronts for linearly polarized light. Experimentally measured wavefronts using a scattering sample with 110 nm sized beads (a) and 1 μm sized beads (b). The CG position was varied in steps of 2 μm and 3 μm , respectively. No absolute CG position was determined. For comparison, wavefronts were determined by MCSs using 110 nm sized beads (c) and 1 μm sized beads (d). To save computational time, a density of scatterers of 1 μm^{-3} and a coherence length of 2 μm were used for the calculation. The CG position was varied from -8 μm to 8 μm in steps of 4 μm . Only relevant Zernike modes are shown: mode 4 (defocus), mode 6 (astigmatism), mode 11 (spherical aberration), and mode 12; all others did not vary with CG position. By linear fitting, the slopes of Zernike modes 4, 6, and 12 (only for (d)) were determined. The legend in (a) is valid for all figures.

objective (Fig. 2.21a). However, the amplitude variation of the scattered light for different scattering angles (Fig. 2.21c,d) and, in addition, the change of the polarization due to both Mie scattering and objective weight the contribution of each emanating spherical wavelet to the incoherent superposition at a certain detection point. The weight is expressed by $W_{Pol}^{(k)}(u, v)$, which can be written also as $W_{Pol}(x/F(z), y/F(z); u, v)$, where x , y and z are the coordinates of the scatterer k and $F(z)$ is the radius of the focal cone in a distance z to the focus. For a simultaneous

rotation of the position of the scatterer (x, y) and the detection point (u, v) around the optical axis, the angles of refraction due to the objective and the scattering angles remain the same but the linear polarization of the incoming light does not rotate simultaneously (Fig. 2.22a). Therefore, $W_{Pol}(x/F(z), y/F(z); u, v)$ is not rotational invariant if the incoming light is linearly polarized and the amplitude of the Mie-scattering functions is different. If such a rotation by an arbitrary angle α is described by the operator R_α , then this fact can be expressed by

$$W_{Pol}(R_\alpha[x/F(z), y/F(z)]; R_\alpha[u, v]) \neq W_{Pol}(x/F(z), y/F(z); u, v). \quad (2.24)$$

In contrast, $\tau^{(k)}(u, v) = \tau(x, y, z; u, v)$ is rotationally invariant independent from the polarization of the light used:

$$\tau(R_\alpha[x, y], z; R_\alpha[u, v]) = \tau(x, y, z; u, v). \quad (2.25)$$

Therefore, in the case of linearly polarized illumination light the rotational symmetry is broken by W_{Pol} and rotationally symmetric wavefronts are not expected. However, W_{Pol} shows two axial symmetries: one is along the direction of the linear polarization and the other is perpendicular to that. Assuming that the linear polarization is either along the x- or the y-axis, the axial symmetries are (Fig. 2.22b):

$$\begin{aligned} W_{Pol}(-x/F(z), y/F(z); -u, v) &= W_{Pol}(x/F(z), y/F(z); u, v) \\ W_{Pol}(x/F(z), -y/F(z); u, -v) &= W_{Pol}(x/F(z), y/F(z); u, v), \end{aligned} \quad (2.26)$$

where the u-axis is along the x-axis. Therefore, the CGWS-measured wavefronts should also have these two axial symmetries, since the other quantities that determine the CGWS-measured wavefront are all rotationally invariant (see Eqs. (2.6) and (2.25)). Aberrations that have such axial symmetries are Zernike mode 6 (astigmatism) and higher-order Zernike modes, such as 12 and 14 (see Appendix A).

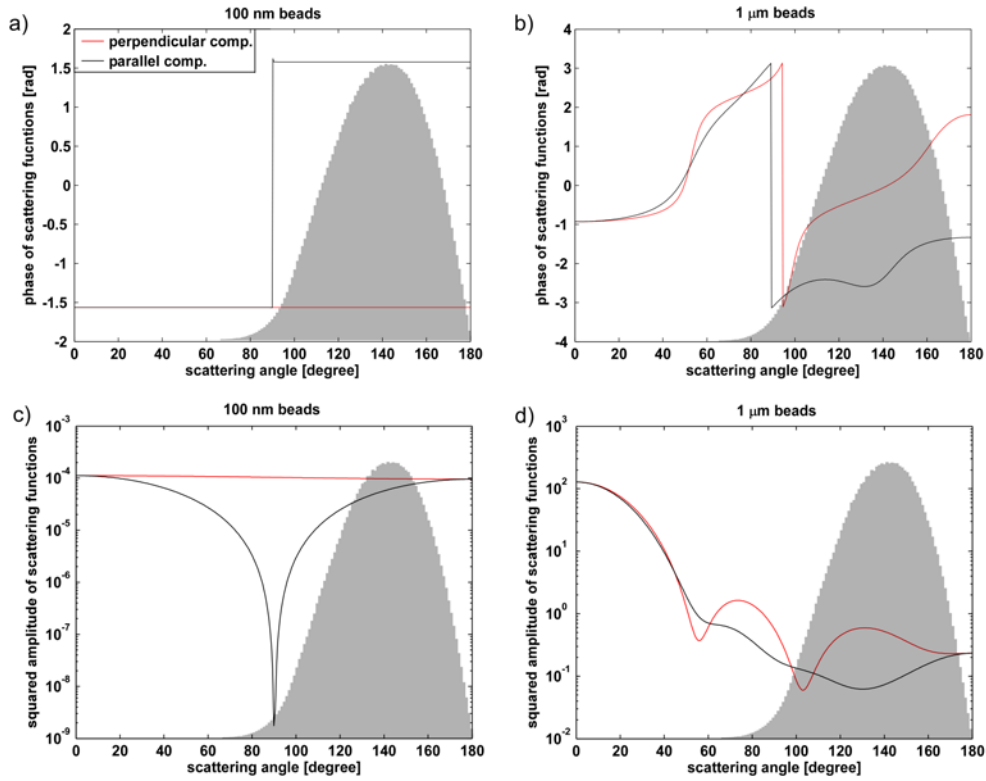
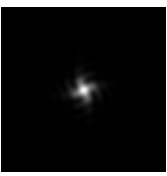


Fig. 2.21. The phase (a), (b) and the squared amplitude (c), (d) of the Mie scattering functions for polystyrene particles (refractive index: 1.6) with diameters of 110 nm and 1 μm , respectively, surrounded by water (refractive index: 1.33) for a wavelength of 0.93 μm . The distribution of the accessible scattering angles for the objective (63x/0.9W) used, indicated by the gray histogram, was calculated numerically assuming isotropic scattering.

A MCS was implemented to verify the observed spurious astigmatism. Both illumination and reference light were linearly polarized. To model the properties of a generic objective lens in terms of polarization, the refraction by a prism was used, which happens to be the simplest diffraction grating [Mansuripur, 1986]. Further, Mie scattering was implemented assuming spherical scatterers of a certain size. The exact steps performed to trace the polarization state are given in Appendix C. Since the tracing of the polarization for each scattered light ray is computationally very expensive, a coherence length of 2 μm and a density of scatterers of 1 μm^{-3} were chosen to keep the number of scatterers small. As was shown in section 2.4.2, for these two parameters the speckles are already fully developed and the results of these MCSs should not be different from other coherence lengths or densities of scatterers as long as the speckles remain fully developed. For example, MCSs with a coherence length of 8 μm yielded similar results (data not shown).

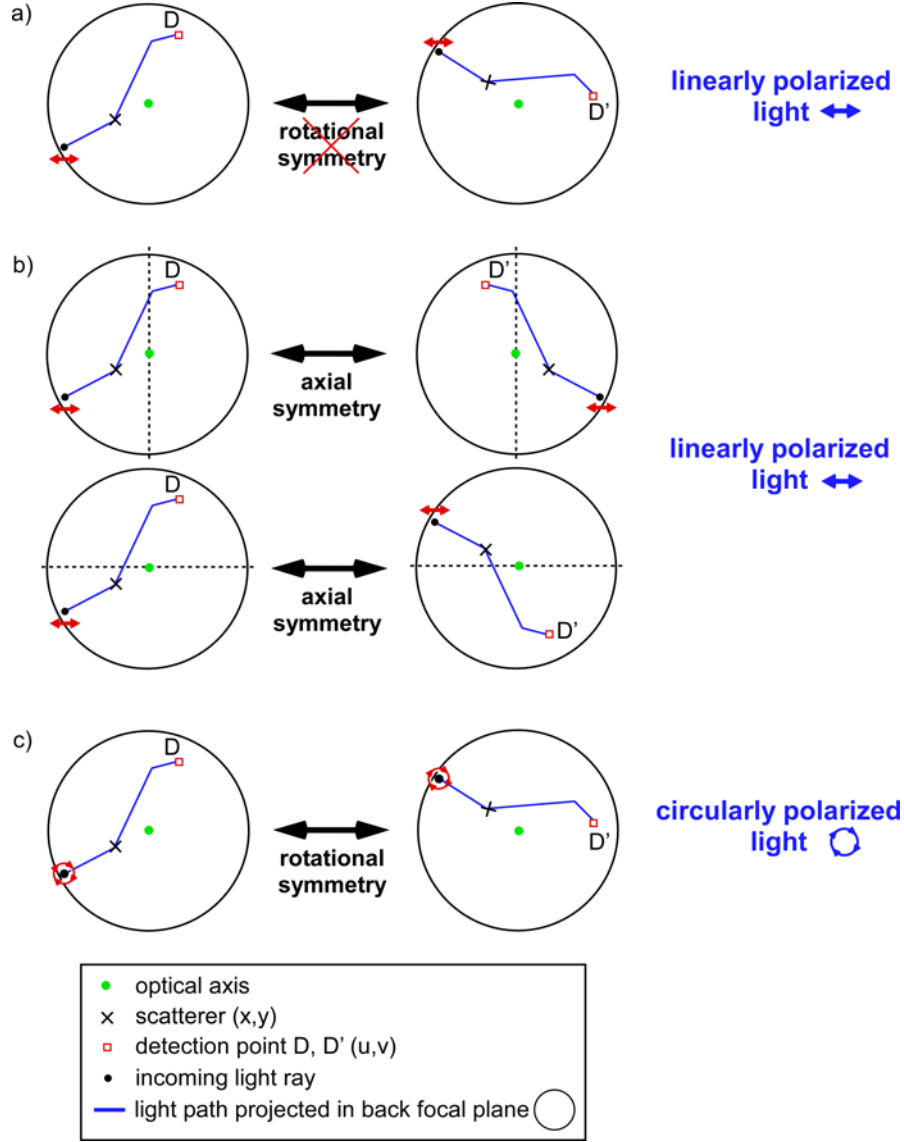


Fig. 2.22. Symmetry properties of W_{Pol} (see text) for a polarized plane wave scattered back to the back focal plane of the objective. The light path for a single scattering event is projected onto the back focal plane. For linearly polarized incoming light the rotational symmetry around the optical axis is violated (a), but two symmetry axes exist (b), which are determined by the direction of the linear polarization. If circularly polarized light is used, the rotational symmetry of W_{Pol} is maintained (c).

The MCSs for 110 nm and 1 μm diameter scatterers showed a linear change of astigmatism (Zernike mode 6) when the CG position was also linearly changed (Fig. 2.20c,d). However, the determined slopes of $+0.024 \pm 0.004 \mu\text{m}/\mu\text{m}$ and



$+0.050 \pm 0.005 \mu\text{m}/\mu\text{m}$ for the 110 nm and 1 μm beads, respectively, were significantly larger compared to the experimental values.

Two reasons can be asserted to explain the discrepancy. First, since a spatial filter (inserted at the focus between the two imaging lenses, not indicated in [Feierabend et al., 2004]) was used experimentally to reject back-reflections from the objective, also some fraction of otherwise useful backscattered light from the sample was rejected. Therefore, the wavefront was slightly spatially filtered [Medecki et al., 1996] and the measured slopes for Zernike mode 4 and 6 were reduced (slopes for c_4 were $+0.083 \pm 0.003 \mu\text{m}/\mu\text{m}$ (100 nm beads) and $+0.062 \pm 0.003 \mu\text{m}/\mu\text{m}$ (1 μm beads) compared to the slopes determined by MCS of $+0.10 \pm 0.01 \mu\text{m}/\mu\text{m}$ (100nm beads) and $+0.11 \pm 0.01 \mu\text{m}/\mu\text{m}$ (1 μm beads)). Furthermore, the simple model of an objective lens does presumably not apply correctly to the objective experimentally used, which contains not only one single lens but several optical elements that are cemented together. In spite of these facts, qualitatively similar results for MCS and experiment were found.

Besides spurious astigmatism also spurious Zernike mode 12 was measured for 1 μm beads by MCS with a slope of $-0.006 \pm 0.001 \mu\text{m}/\mu\text{m}$. Experimentally, no varying spurious Zernike mode 12 could be detected for these beads. Both experimentally and numerically, the expected slope for Zernike mode 11 (see section 2.5.2) was too small and limited by speckle noise.

Spurious aberrations can be avoided if circularly polarized illumination and reference light is used instead, since then also $W_{pol}(x/F(z), y/F(z); u, v)$ exhibits rotational symmetry (Fig. 2.22c):

$$W_{pol}(R_\alpha[x/F(z), y/F(z)]; R_\alpha[u, v]) = W_{pol}(x/F(z), y/F(z); u, v). \quad (2.27)$$

Experimentally, the optical setup described in section 2.2.1 was used where the illumination sample light was changed into circular polarization by a $\lambda/4$ wave-plate but the reference light remained linearly polarized. However, since the backscattered light passes again the $\lambda/4$ wave-plate (Fig. 2.2) on the way back to the CGWS, this experimental situation is the same as if the reference light is circularly polarized and

the backscattered light does not pass the $\lambda/4$ wave-plate. The latter situation is used for the MCSs.

For this setup, the measured slopes for spurious astigmatism were very low. For scattering samples containing either 110 nm or 1 μm beads, the slopes found were $+0.002 \pm 0.003 \mu\text{m}/\mu\text{m}$ and $+0.006 \pm 0.003 \mu\text{m}/\mu\text{m}$, respectively. For the MCS with circularly polarized light the determined slopes were $+0.001 \pm 0.003 \mu\text{m}/\mu\text{m}$ (100 nm beads) and $-0.002 \pm 0.003 \mu\text{m}/\mu\text{m}$ (1 μm beads). Other spurious aberrations were not found.

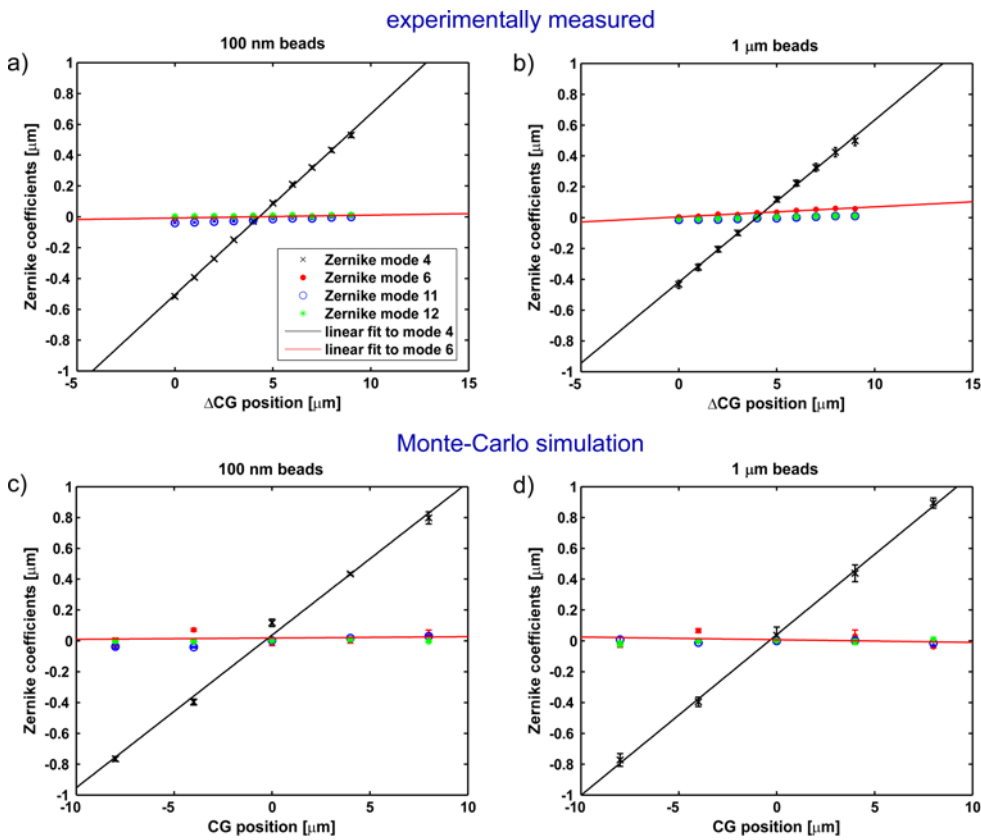
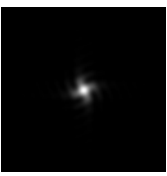


Fig. 2.23. CGWS-measured wavefronts for circularly polarized light. Experimentally measured wavefronts using a scattering sample with 110 nm sized beads (a) and 1 μm sized beads (b). The CG position was varied in steps of 1 μm . No absolute CG position was determined. For comparison, wavefronts were determined by MCSs using 110 nm sized beads (c) and 1 μm sized beads (d). To save computational time, a density of scatterers of $1 \mu\text{m}^{-3}$ and a coherence length of 2 μm were used. The CG position was varied from -8 μm to 8 μm in steps of 4 μm . Only relevant Zernike modes are shown: mode 4 (defocus), mode 6 (astigmatism), mode 11 (spherical aberration), and mode 12; all others did not vary with CG position. By linear fitting, the slopes of Zernike mode 4 and 6 were determined. The legend in (a) is valid for all figures.



The MCSs based on circularly polarized light were comparable to the MCSs where polarization effects were neglected and point-like scatterers were assumed (see section 2.2.2). Although the slopes for the Zernike defocus of $+0.099 \pm 0.004 \mu\text{m}/\mu\text{m}$ (100nm beads) and $+0.104 \pm 0.004 \mu\text{m}/\mu\text{m}$ (1 μm beads) were slightly smaller than $+0.12 \mu\text{m}/\mu\text{m}$ for the MCS without polarization effects, significantly different results in terms of the accurate measurement of aberrations are not expected. The model of independent spherical wavelets emanating from the CV is valid even if polarization effects are included as long as the speckles are fully developed (see section 2.4.2).

2.7 Discussion

Experimentally measured wavefronts using CGWS were compared to wavefronts obtained by Monte-Carlo simulations (MCS). All experimentally observed properties of CGWS-measured wavefronts, such as the change of the Zernike defocus with the variation of the CG position (see section 2.4.2), the independence of the measured wavefront on aberrations of the incoming light when the speckles are fully developed (see section 2.5.1), and the correct measurement of aberrations in the optical path (see sections 2.5.1 and 2.5.2), were consistent with the predictions of the MCSs. Only for the dependence of the CGWS-measured wavefronts on the polarization of the incoming light (see section 2.7), the discrepancy between experiment and MCS was higher. Presumably, the assumed simple model of an objective led only to qualitative agreements (see section 2.7). However, some further assumptions were made for the model of CGWS (see section 2.1), which needs to be discussed and should reveal some new interesting facts.

First, the attenuation of the illumination intensity with depth due to scattering was ignored. Such attenuation, in particular if the attenuation length is comparable to the coherence-gate length, will result in more weight being given to scatterers near the surface of the specimen and, thus, will result in a shift of the centroid of the coherence volumes towards the surface. However, this should significantly affect only the measured rotationally symmetric Zernike modes, such as defocus c_4 and spherical aberration c_{11} .

Second, a major assumption of the CGWS-model is to consider only ballistic light while neglecting multiply scattered light within the coherence gate. In general, this assumption can be justified only for low probing depths in strongly scattering specimens. To quantify at which focus depth coherence-gated multiply scattered light will dominate over coherence-gated ballistic light, observations from optical coherence tomography (OCT) can be used. For OCT the maximum probing depth is restricted to several (5-8) mean free path lengths, depending on the scattering properties of the tissue [Schmitt, 1999; Lu et al., 2004]. Since confocal detection is predominately used for OCT [Fercher et al., 2003; Karamata et al., 2005], CGWS should achieve about the same probing depth if a pinhole is inserted in the sample arm in order to reject some part of the coherence-gated multiply scattered light.



However, the pinhole can also act as a spatial filter and should lead to an underestimation of aberrations present. In the case of a sub-resolution pinhole size, the measured wavefront would even be aberration-free [Medeck et al., 1996]. Therefore, the size of the pinhole has to be adjusted to the expected strength of aberrations.

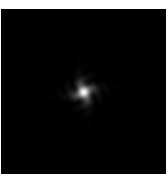
Since the coherence-gated portion of the multiply scattered light is predominantly scattered above the coherence volume (CV of the single-scattered light) and originates from a laterally more extended volume, three effects on CGWS-measured wavefronts can be expected. First, the spatial coherence of the CGWS-selected backscattered light will be reduced (see section 2.4.3). Therefore, the proportionality constant σ_0 (see section 2.4.3) will rise, but by averaging over more ensembles of scatterers the speckle error can be reduced to the required level. Second, the measured defocus will not be zero anymore if the CG position is at the focus. This means that to correct for all aberrations in the optical path to the focus, the correction to zero defocus might lead to an erroneous detection of the relevant aberrations. Third, the effect of lateral averaging of aberrations located within the specimen will be enhanced (see section 2.5.3).

A third assumption of the model was the use of discrete, randomly located particles to describe the scattering of light within tissue. This assumption is funded on investigations of scattering properties that revealed that the refractive index variations within biological specimens can be realistically modeled as discrete, differently sized particles [Schmitt et al., 1998; Mourant et al., 2002; Wilson et al., 2005]. It was found that the particle distribution responsible for the scattering extinction peaks at sizes of about $2-4\lambda$ [Schmitt et al., 1998; Mourant et al., 2002; Wilson et al., 2005], whereas high-angle scattering is mainly due to particles with sizes in the range from $\lambda/4 - \lambda/2$ [Mourant et al., 1998; Schmitt et al., 1998]. Cellular organelles, in particular mitochondria (0.5-1.5 μm), lysosomes (0.5 μm), and structures within the nucleus (3-10 μm), contribute most to backscattering [Dunn, 1997; Mourant et al., 1998; Drezek et al., 1999]. Depending on the type of tissue collagen and elastin fibers enhance the backscattering efficiency [Drezek et al., 1999]. Under the assumption that particles with sizes of $\lambda/4 - \lambda/2$ dominate the backscattering, the density of scatterers can be maximally about $100 \mu\text{m}^{-3}$. Therefore, the coherent effects observed due to the transition of fully developed speckle into partially developed (see Fig. 2.7

and 2.8) will likely not occur for biological specimens, independent of which coherence length is experimentally chosen.

A further assumption of the MCS concerns the homogenous distribution of scatterers inside the focal cone, which is, in general, not homogenous in real tissues. An inhomogeneous distribution, however, will hardly alter the CGWS-measured wavefront since each scatterer contributes independently to CGWS (see section 2.4.2) unless abnormal distributions, such as scatterers located only in a thin layer, are present (see section 2.5.1).

In conclusion, it was shown that the ensemble-averaged CGWS-measured wavefronts correspond to the actual aberrations in the optical path as long as the speckles are fully developed, which should be the case for all experimentally accessible coherence lengths (larger than $4\text{ }\mu\text{m}$, [Drexler, 2004]) and realistic densities of scatterers (see above). In this regime the CGWS-measured wavefront corresponds to the incoherent superposition of originally spherical wavelets emanating from each of the individual scatterers and then altered by the aberrations while propagating back through the sample and the optical system. Polarization-induced spurious aberrations, which depend on the coherence-gate position, can be avoided by using circularly polarized light. However, the circular polarization of the light can not be strictly maintained, since most tissues are to some extent birefringent. For strongly birefringent tissues, such as cartilage and connective tissue fibers, the CG position-dependence of spurious aberrations and the fact that they vanish when the CG position is at the focus can be used to discriminate against spurious aberrations.



3 Wavefront correction using CGWS

Closed-loop CGWS-based wavefront correction will be demonstrated on several samples, even on living biological organisms. Wavefront correction was combined with two-photon microscopy to verify and demonstrate the improvement in image quality. As a measure of image quality the point-spread function, the fluorescence signal for uniformly stained specimens, and the peak fluorescence for point-like structures within a specimen were investigated before and after wavefront correction.

3.1 Characterization of the deformable mirror (DM)

As a wavefront correction element an electrostatically-deflected membrane mirror (DM, Oko Technologies, [Vdovin et al., 1995]) was employed (Fig. 3.1a). By means of bulk micromachining the gold-coated membrane (diameter 15 mm) was mounted approximately 45 μm above 37 actuators arranged in a hexagonal shape driving the membrane shape (Fig. 3.1b). The maximum achievable deflection of the membrane is, typically, about 7 μm for the maximum voltage of 300 V applied to all actuators. Only the well-controllable region of the membrane with a diameter of 9.7 mm was used for wavefront correction [Paterson et al., 2000].

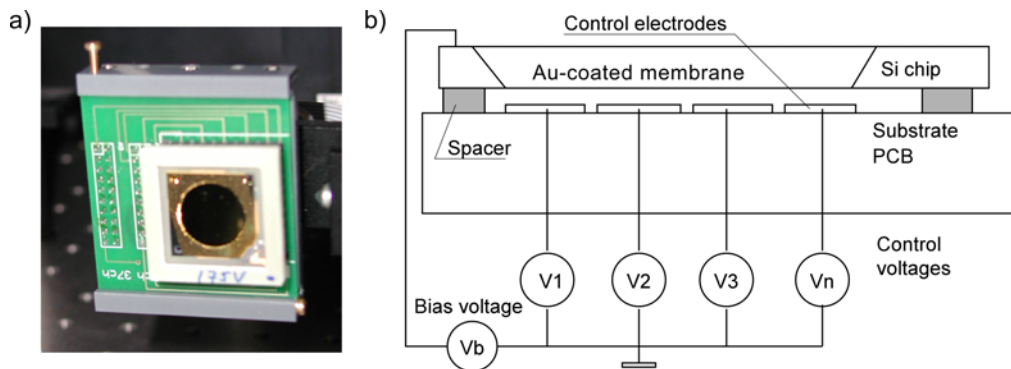


Fig. 3.1. Photograph (a) and schematic drawing of a cross section (b) of the gold-coated deformable mirror (from OKO Technologies).

The optical setup contains a calibration arm that extracts a portion of the reference light by means of a beamsplitter cube in order to characterize the DM (Fig. 2.2). Therefore, the length of the reference arm was adjusted so that the optical path lengths for light travelling in the calibration and in the reference arms were the same.

The shape of the DM, described in terms of 28 Zernike polynomials using a set of coefficients \mathbf{c}_s , depends roughly quadratically on the set of voltages (the deflection due to the voltage distribution can be described by the Poisson equation, [Fernandez et al., 2003]). Therefore, a set of variables $\mathbf{s} = (s_1, \dots, s_{37}) = (v_1^2, \dots, v_{37}^2)$ is used, whereby for each voltage $0 < v_i < v_{\max}$, and the deflection of the DM can be described by

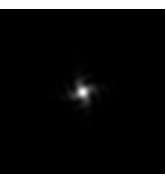
$$\mathbf{c}_s \approx M \cdot \left(\mathbf{s} - \frac{\mathbf{s}_{\max}}{2} \right) + \mathbf{c}_{ini}, \quad (3.1)$$

where M is the "characteristic" matrix describing the response of the DM [Zhu et al., 1999b] and \mathbf{c}_{ini} the initial deviation from a flat wavefront. In order to allow deflections for the DM in both directions, all actuator voltages are initially set to $v_{\max}/\sqrt{2}$, i.e. $s_i = s_{\max}/2$, with the resulting defocus compensated by adjusting the position of a lens in the sample arm (L6, Fig. 2.2).

The matrix M was determined by measuring the difference in the response to a voltage of $\sqrt{3}/2 \cdot v_{\max}$ and $v_{\max}/\sqrt{2}$ applied to each of the 37 actuators using the calibration arm.

For the generation of different shapes of the membrane an iterative scheme was chosen, which is insensitive to nonlinearities of the DM and the vSHS (see below and section 2.3.1). Equation (3.1) would suggest that the voltage needed to generate the desired shape of the membrane $\mathbf{c}_{desired}$ simply can be obtained by multiplying $\mathbf{c}_{desired} - \mathbf{c}_{ini}$ with the (pseudo) inverse of M [Zhu et al., 1999a; Paterson et al., 2000]. Because this frequently would call for voltages outside the available range, quadratic programming (implemented using the Matlab function quadprog, [Gill, 1995]) is applied, which, like the (pseudo) inverse, minimizes

$$\left\| \beta \cdot (\mathbf{c}_{desired} - \mathbf{c}^{(n-1)}) + M \cdot (\mathbf{s}^{(n)} - \mathbf{s}^{(n-1)}) \right\|, \quad (3.2)$$



while, unlike the pseudo inverse, maintaining $0 < v_{(i)} < v_{\max}$; $\mathbf{c}^{(n-1)}$ is the measured wavefront with $\mathbf{s}^{(n-1)}$ applied to the DM for the n -th iteration step; $\| \cdot \|$ indicates the L_2 norm. The parameter β determines the convergence rate and was between 0.8 and 1. Unless a reference wavefront was specified (see below) the wavefront correction was started from $\mathbf{s}^{(0)} = \mathbf{s}_{\max} / 2$.

Besides its limited capability of changing the membrane shape with a maximum frequency of 500 Hz, a further technical limit of the DM concerns the correction of high-order aberrations. Therefore, the maximum amplitude for all Zernike modes from 4 to 28 was determined both for positive and negative deflections of the membrane. By using Eq. (3.2) wavefronts with a single Zernike mode, where the coefficients were changed in steps of $\pm 0.02 \mu\text{m}$, were tried to produce. To define a criterion when the maximum coefficient for a certain Zernike mode was reached, the RMS deviation to the desired wavefront (calculated over Zernike mode 4 to 28) had to be smaller than $0.02 \mu\text{m}$ after 3 iteration steps. The measured maximum coefficient for the Zernike defocus c_4 in total (positive and negative deflection combined) was about $1.4 \mu\text{m}$, corresponding to a maximum deflection at the center of the membrane of about $5 \mu\text{m}$ (Fig. 3.2). This is smaller than the expected $7 \mu\text{m}$ stated by the manufacturer, presumably due to an unspecified stress-induced displacement of the membrane. For high-order aberrations the maximum Zernike coefficient decreases rapidly but, in particular, the coefficients for astigmatism (mode 5 and 6) and coma (mode 7 and 8) were sufficiently large to demonstrate CGWS-based wavefront correction (see below). Note that the maximum Zernike coefficients for positive and negative deflections were slightly different for the low-order Zernike modes although the deflection of the DM was biased to half of its maximum deflection (see above, Fig. 3.2).

Another important characteristic of the DM is its deviation from linear performance (see Eq. (3.1)). Since the deviation depends on the strength and on the type of aberration, only a rough estimation can be given. For the wavefront correction experiments presented in this chapter the deviation from linearity was not higher than $0.01 \mu\text{m}$ (RMS) if the voltages applied to the actuators were not at the limit of their range.

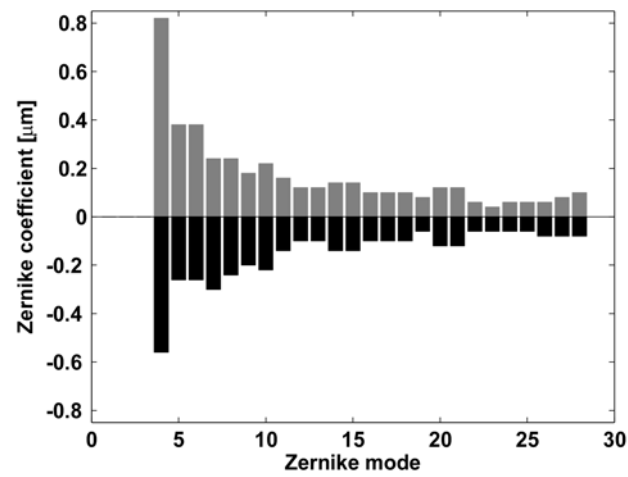
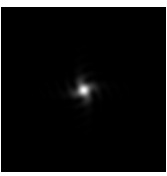


Fig. 3.2. Deflection limit of DM for different Zernike modes. Maximum possible Zernike coefficients for positive (gray bars) and negative (black bars) deflections of the membrane.



3.2 Principle of wavefront correction

Scattering at inhomogeneities in the refractive index within turbulent media, such as the atmosphere or biological specimens, corrupt the propagation of the light, resulting in speckle patterns (scintillation) and associated phase singularities [Fried et al., 1992; Roggemann et al., 2000]. Thus, the phase function of the distorted electric field is not continuous anymore but is instead composed of a vortex phase (also called hidden phase [Fried, 1998]) caused by the singularities and a potential phase that describes a continuous phase function [Aksenov et al., 1998]. The potential phase can be extracted from the phase function by least-squares fitting and is that part of the phase that is widely used for adaptive wavefront correction [Fried, 1998; Roggemann et al., 2000]. However, wavefront correction of the potential phase part is complete only if the light propagation through the media can be described in the geometrical optics approximation [Hardy, 1998; Roggemann et al., 2000]. If the media is strongly turbulent, high-angle scattering can occur and the geometrical optics approximation is not valid anymore. In this case, the performance of adaptive wavefront correction can be improved by using the complete phase function [Tyler, 2000].

Speckles and associated phase singularities are intrinsic for CGWS, even if the specimen is not turbulent at all. This is due to the fact that the coherence-gated light, which is scattered back from an extended CV, coherently superimpose at the CGWS (see section 2.4.2). A turbulent layer in the optical path can alter the speckle pattern and, thus, the vortex phase. Only that part of the vortex phase that is caused by the turbulent layer needs to be corrected [Vorontsov et al., 2002; Vorontsov et al., 2005]. However, no method exists so far to distinguish between these two contributions of the vortex phase [Vorontsov et al., 2005]. To make it clear: using the principle of optical reciprocity [Born et al., 1999], the focus would be as large as the CV if the complete vortex phase together with the potential phase of the CGWS-measured electric field is pre-compensated.

To restore a diffraction-limited focus, the electric field sent out from a single Rayleigh-scatterer located at the focus needs to be sensed. In this case, the vortex phase is caused only by the turbulent layer and the time-reversed electric field would result in a diffraction-limited focus (optical reciprocity theorem). Since the speckle-averaged CGWS-measured wavefronts are the incoherent superposition of spherical waves emanating from the CV, the aberrations of the potential phase of light scattered

from a single scatterer can be reconstructed by CGWS, except for tip/tilt and defocus (see section 2.5). By shaping the DM in such a way that it generates the phase-conjugated potential phase of the speckle-averaged CGWS-measured wavefront, a diffraction-limited focus can be restored (Fig. 3.3). If it were possible to compensate also for the turbulence-induced vortex phase, the scattering within the turbulence would be compensated and more incoming light would be directed to the focus, allowing, e.g., a higher two-photon fluorescence excitation. However, this exceeds the scope of this thesis and needs be addressed in the future (see chapter 4).

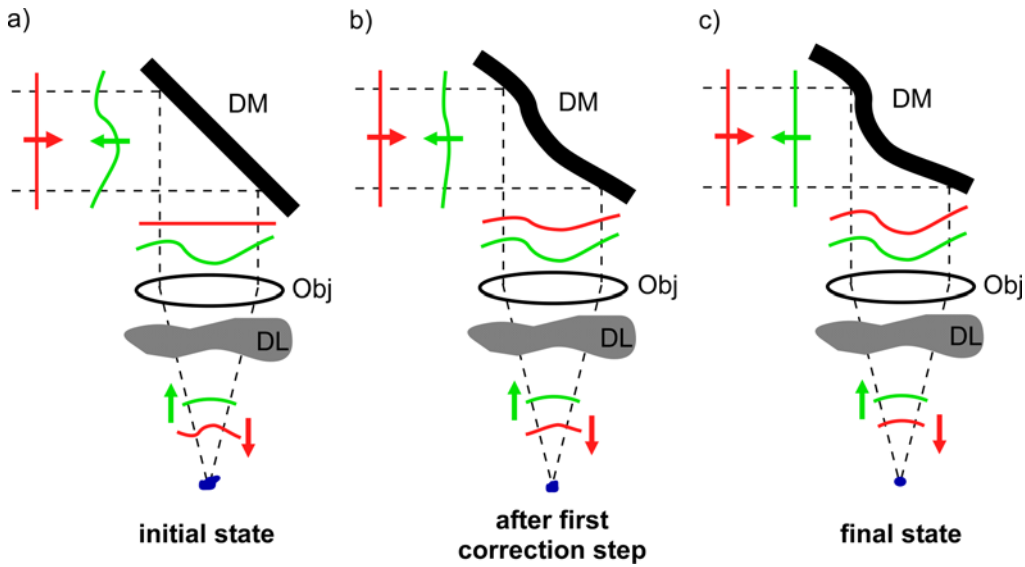
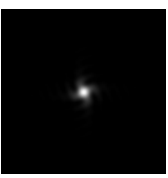


Fig. 3.3. Iterative wavefront correction to a flat speckle-averaged CGWS-measured wavefront. A simplified setup (deformable mirror DM, objective Obj, distortion layer DL) was assumed to illustrate the principle of wavefront correction based on the optical reciprocity theorem. In the initial state, where the DM is flat (a), the potential phase is measured and, then, the DM applies the phase conjugation (b). Because of nonlinearities of DM and vSHS, the distortions are not yet completely cancelled. By correcting iteratively to a flat wavefront the final state (c) of a diffraction-limited focus is reached. Red and green wavefronts indicate the ingoing and returning potential phase functions, respectively.

While an accurate shaping of the membrane is possible without iteration (open-loop), if the response properties of DM and vSHS are sufficiently well known, the more robust closed-loop operation (with iteration), which is insensitive to nonlinearities of DM and vSHS, was chosen instead. Therefore, not only the wavefront of the illumination light but also the wavefront of the backscattered light were deformed by the DM (Fig. 2.2).



Only Zernike modes 5 to 28 were corrected by the DM because these correspond to aberrations that change the focus shape; tip/tilt (modes 2 and 3) and defocus (mode 4) only shift the focus laterally or axially (see section 2.5.1). However, to sense all distortions in the path to the focus, CGWS needs to select backscattered light that originates from the focal region, i.e. the measured defocus should be zero. Although the DM can correct for defocus, the dynamic range would be then reduced. A better way is to iteratively adjust the length of the reference arm on which the defocus depends linearly (slope of about $0.12 \mu\text{m}/\mu\text{m}$ per $2.66 \mu\text{m}$ change of the arm length, which corresponds to $1 \mu\text{m}$ displacement of the CG position, see section 2.4.2).

In most cases the deviation of the measured wavefront from the flat wavefront no longer decreased significantly beyond 3 iterations (Fig. 3.4).

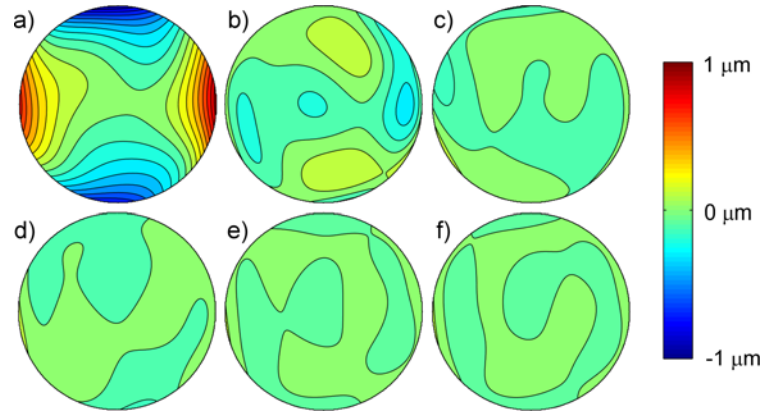


Fig. 3.4. Exemplary sequence of wavefronts during a 5 step iterative correction of the distortions introduced by a glass capillary (see section 3.4). The initial deviation (a) was $0.283 \mu\text{m}$ (RMS), which was measured as the mirror was set to its reference shape. With the subsequent steps the deviation was reduced to $0.092 \mu\text{m}$ (b), $0.040 \mu\text{m}$ (c), $0.030 \mu\text{m}$ (d), $0.018 \mu\text{m}$ (e) and $0.017 \mu\text{m}$ (f). Some actuators of the DM reached their deflection limit already after the first iteration step. At the end of the sequence more than half of the actuators were at the limit. Contour lines are spaced by $0.1 \mu\text{m}$.

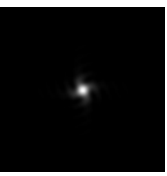
3.3 Fluorescence measurements in uniformly fluorescent samples

Since focus distortion leads to a reduction in the efficiency of two-photon excitation and hence fluorescence generation the total amount of fluorescence is sensitive to wavefront aberrations. Therefore, it was tested whether the experimentally determined dependence of the fluorescence signals on the strength and on the type of aberration matches what is theoretically expected. For the experiment and theory uniformly fluorescent samples were used and assumed, respectively. The expected two-photon excited fluorescence was calculated by numerically integrating the square of the intensity distribution (in the non-paraxial Debye approximation [Born et al., 1999] over the focal region):

$$F \propto \iiint du dv dw \left| \iint_A dx dy E(x, y) e^{i\phi(x, y)} e^{\frac{2\pi \cdot n}{\lambda} \cdot w \cdot \sqrt{1 - (x^2 + y^2)/f^2}} e^{\frac{2\pi \cdot n}{\lambda \cdot f} (x \cdot u + y \cdot v)} \right|^4, \quad (3.3)$$

with the origin of the u , v , and w coordinate system placed at the focus point and the optical axis oriented along w ; x and y parametrize the back focal plane; λ denotes the wavelength of the light, f the focal length of the objective, and n the refractive index of water; $\phi(x, y)$ is the wavefront and $E(x, y)$ is the intensity profile of the illumination light across the aperture A located in the back focal plane; $i = \sqrt{-1}$. The integration volume (centered at the focus) was $16.1 \mu\text{m} \times 16.1 \mu\text{m} \times 20 \mu\text{m}$ and was sampled at intervals of $0.06 \mu\text{m}$ for u and v and $0.05 \mu\text{m}$ for w . All theory/experiment comparisons were between values normalized to those for a flat wavefront. The non-paraxial Debye approximation is to a high degree of accuracy the solution to the Helmholtz equation [Wolf et al., 1981] and since the Fresnel number $N = R_A^2 / \lambda f$ is sufficiently larger than 1 for the objective used (see section 2.2.1), the vectorial aspect of the illumination light can be neglected [Hsu et al., 1994].

The numerical calculations for a uniform illumination of the aperture show that the efficiency in fluorescence generation decreases almost equally for different wavefront aberrations (Fig. 3.5). For example, for a deviation of $0.2 \mu\text{m}$ (RMS) the excitation efficiency is roughly a factor of 2 smaller than for an aberration-free system.



Experimentally, however, the intensity profile was Gaussian over the back focal plane (fill factor 1.25, see section 2.2.1), which reduces slightly the effect of aberrations on the excitation efficiency (Fig. 3.6).

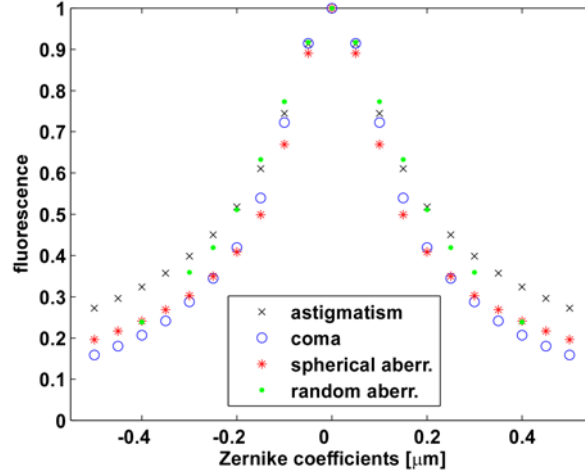


Fig. 3.5. Numerically calculated fluorescence intensity (normalized to maximum intensity) vs. Zernike coefficients for a uniformly illuminated aperture (Eq. (3.3)). The investigated aberrations were astigmatism (Zernike mode 5 or 6), coma (Zernike mode 7 or 8), spherical aberration (Zernike mode 11), and a randomly aberrated wavefront. For the latter the deviation was distributed uniformly over Zernike modes 5 to 28.

The experimental measurements were performed as follows. First, a diffraction-limited focus, having the highest excitation efficiency, was generated as described by Eq. (3.2) using the scattering sample (correction to a flat CGWS-measured wavefront $\mathbf{c}_{desired} = \mathbf{0}$). Then foci with known aberrations were generated using only the DM by correcting to a CGWS-measured wavefront with the desired aberrations. In this case, by reciprocity the ingoing wavefront converges to the desired aberrations. After 3 iterations a deviation of typically $0.01 \mu\text{m}$ (RMS) was reached. Different sets of aberrated foci, each containing only a single Zernike mode (5, 6, 7 or 8) but of different strength ($\pm 0.1 \mu\text{m}$, $\pm 0.14 \mu\text{m}$ and $\pm 0.18 \mu\text{m}$) were thus generated.

For each aberrated focus and also for the non-aberrated focus the fluorescence excited by two-photon absorption within a “uniformly” fluorescent sample (see below) was recorded by averaging the fluorescence signal while scanning the sample laterally over an area of $3 \mu\text{m} \times 3 \mu\text{m}$. For an aberration of $-0.140 \pm 0.006 \mu\text{m}$ in c_5 , for example, the values varied by 3.5 % between repeated correction cycles (Fig. 3.6).

This fluctuation is probably not only due to speckle, which should cause only a variation of about 2 %. Theoretical and experimental data agree within the error limits (Fig. 3.6). This also shows that neither significant astigmatism nor coma was present in the reference arm, because such an aberration would lead to a laterally shifted fluorescence vs. aberration curve.

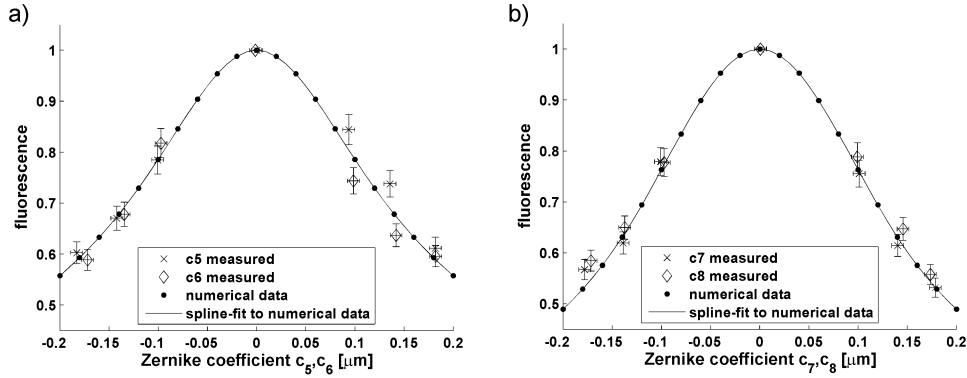
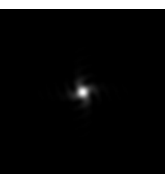


Fig. 3.6. Experimentally measured fluorescence intensities (normalized to maximum intensity) in a “uniformly” stained specimen as a function of astigmatism (a) and coma (b). The solid curves are spline fits to numerical calculations of the Debye Integral (Eq. (3.3)) with a Gaussian intensity profile.

Sample preparation

The scattering sample (mean free path $\approx 550 \mu\text{m}$) used for these experiments contained polystyrene beads (110 nm diameter, 15 beads/ μm^3 , Polysciences, 00876) embedded in an aqueous agarose gel (1% low-melting point A9414, Sigma) and also contained 100 μM fluorescein (fluorescein-sodium salt 46960, Fluka).



3.4 Correction of glass-capillary induced distortions

In order to test CGWS-based wavefront correction on a sample that contains a known, well quantifiable distortion a cylindrical glass capillary was used, which was filled with a scattering sample containing fluorescent beads (see below and Fig. 3.7a). Before introducing the capillary sample, first a reference shape for the DM was established by correcting (using 5 iterations) all aberrations introduced by the optical elements of the microscope (of which are due to DM with all $v_i = v_{\max} / \sqrt{2}$: $c_5 = -0.03 \mu\text{m}$, $c_6 = 0.06 \mu\text{m}$, $c_7 = -0.02 \mu\text{m}$, $c_8 = -0.01 \mu\text{m}$; and due the objective: $c_{11} = -0.025 \mu\text{m}$, $c_{22} = 0.025 \mu\text{m}$) using a scattering sample (same as used for the experiments in section 3.3) without capillary. Then, the capillary sample was introduced and images without correction were taken (Fig. 3.7b), which show a strongly astigmatic point spread function (see below).

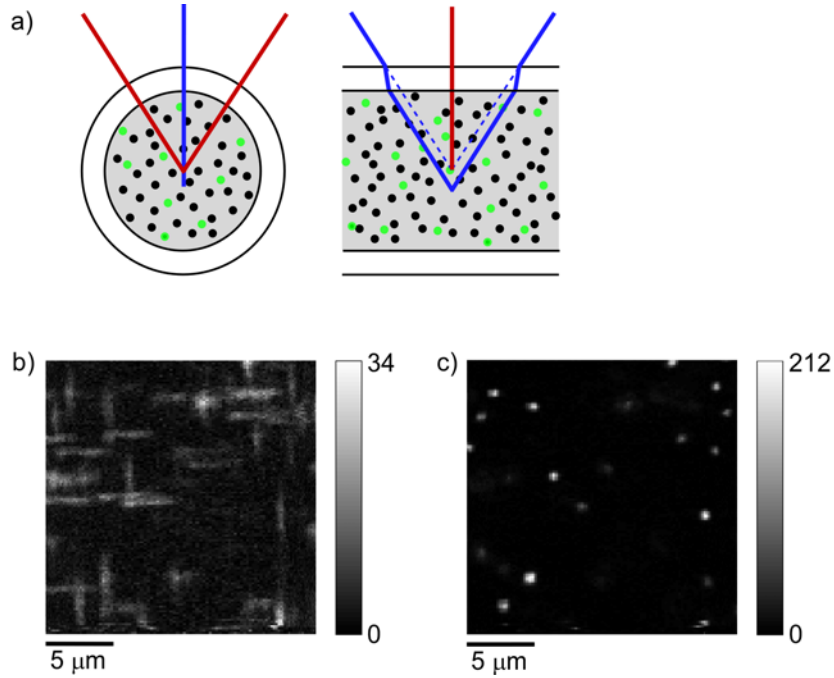


Fig. 3.7. CGWS-based correction of glass-capillary induced wavefront distortion. Rays (a) in the planes orthogonal and parallel to the capillary axis form foci in different depths leading to an astigmatic distortion. Scattering and fluorescence beads are depicted as black and green dots, respectively. Single focal plane images of fluorescent beads before (b) and after (c) wavefront correction show line foci typical for strong astigmatism. Background was subtracted and the sinusoidal scan geometry was linearized. The gray scale of the images is proportional to the measured fluorescence intensity (arbitrary units).

The measured aberrations confirmed that mainly astigmatism (c_6 : $-0.276 \pm 0.006 \mu\text{m}$, in agreement to the expected astigmatism of $-0.280 \mu\text{m}$ calculated for the capillary geometry used, see Appendix D) affected the focus, whereas higher-order aberrations (the largest was c_{12} with $-0.034 \mu\text{m}$) were barely detectable.

Typically for astigmatic point-spread functions is that the intensity distribution in a xy-plane above the Gaussian focus is elongated along one direction, for a plane below the Gaussian focus, however, along the perpendicular direction (Figs. 3.8a-c). Also striking is that the fluorescence at the Gaussian focus is lower than in a distance apart from focus (Fig. 3.8b), showing that two foci are evolved. For the measured astigmatism an inter-foci distance of $3.6 \mu\text{m}$ was numerically calculated. This is consistent with the inter-foci distance of $3.4 \pm 0.2 \mu\text{m}$ measured for one bead using an image stack (Fig. 3.8c).

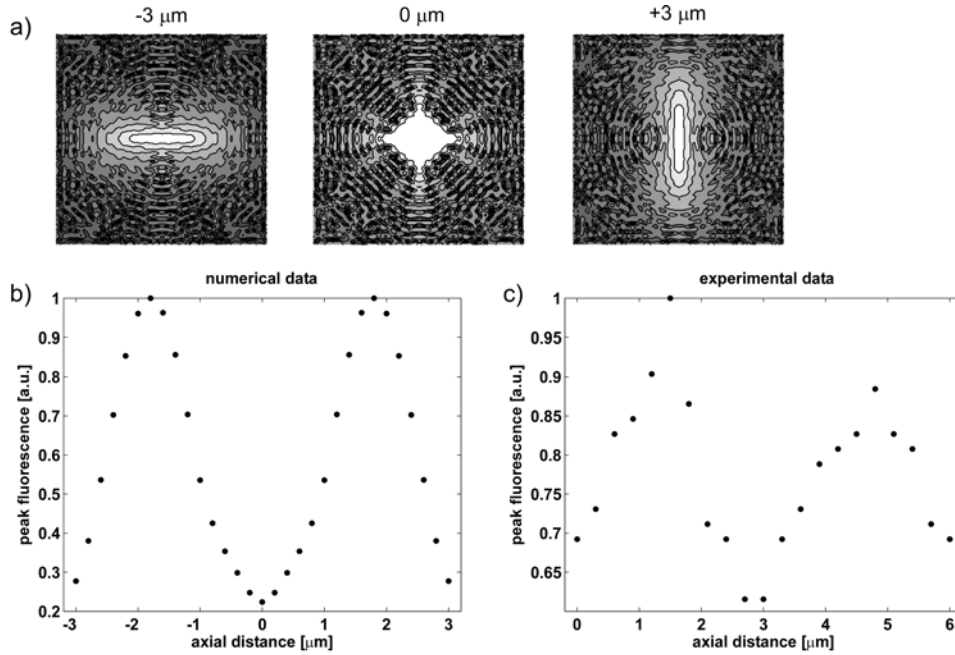
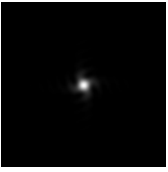


Fig. 3.8. Images (a) of an astigmatic point-spread function ($c_6 = -0.28 \mu\text{m}$) in 3 planes (section: $7.5 \mu\text{m} \times 7.5 \mu\text{m}$), perpendicular to the optical axis, in a distance of $-3 \mu\text{m}$, $0 \mu\text{m}$, and $3 \mu\text{m}$ to the Gaussian focus, calculated numerically with the Debye integral (Eq. (3.3)). The two-photon excited fluorescence intensity is on a logarithmic scale. The peak fluorescence (normalized to the maximum value) for a sequence of planes vs. axial distance was numerically calculated (b) and experimentally measured (c). For the experimental data an image stack with 40 images, spaced by $0.3 \mu\text{m}$ was taken. The axial distance in (c) starts with the first image of the stack.



When wavefront correction was started, stabilizing (to within 0.02 μm) after 5 iterations (Fig. 3.4), the corrected image showed a 6-fold improvement in the peak fluorescence and a clear increase in resolution (Figs. 3.7b,c).

In image stacks taken with the corrected wavefront the lateral widths (full width at half maximum) of bead images (using the brightest beads) were $0.66 \pm 0.05 \mu\text{m}$ and $0.57 \pm 0.05 \mu\text{m}$ for y- and x-directions, respectively, not significantly different from values from samples without distorting elements ($0.62 \pm 0.05 \mu\text{m}$ and $0.53 \pm 0.05 \mu\text{m}$). The discrepancy to the theoretical values for the lateral focus size (numerically calculated for Gaussian profile: 0.40 μm and 0.39 μm ; see also Eq. (1.1): $\Delta_{xy} = 0.39 \mu\text{m}$ for uniform illumination) is likely due to residual Brownian motion of the fluorescent beads.

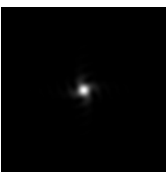
For a similar sample where the capillary was filled with a “uniformly” fluorescent sample (see below), the fluorescence (Eq. (3.3)) was 2 times higher after wavefront correction was applied. This is roughly consistent with the numerically calculated value of a factor of 2.5 for the fluorescence increase, taking into account the measured astigmatism (c_6 : $-0.332 \pm 0.006 \mu\text{m}$, slightly lower than the theoretical expectation of $-0.35 \mu\text{m}$ for the capillary geometry used).

Sample preparation

The capillary with fluorescent beads (270 μm outer diameter, 24 μm wall thickness, measured under a stereomicroscope) was produced from a larger capillary (1 mm outer diameter with 100 μm wall thickness, Hilgenberg) on a micropipette puller (P-2000, Sutter Instrument Company). The capillary was filled with scattering beads (110 nm diameter, 6 per μm^3 , Polysciences, 00876) and fluorescent beads (93 nm, 0.2 per μm^3 , yellow-green FluorSpheres, Invitrogen, F8803) immobilized in agarose (1% low-melting point A9414, Sigma). The illumination focus was located in the center of the capillary.

The capillary surrounding a “uniformly” fluorescent scattering sample had an outer diameter of 300 μm and a wall thickness of 30 μm . The sample contained scattering beads (110 nm diameter, 6 per μm^3 , Polysciences, 00876) embedded in agarose (1%

low-melting point A9414, Sigma) and also contained 100 μM fluorescein (fluorescein-sodium salt 46960, Fluka). The illumination focus was located in a depth of about 200 μm .



3.5 Correction of zebrafish-induced distortions

As a final demonstration the feasibility of CGWS-based wavefront correction in a living biological specimen is presented. To this end, the developing olfactory bulb in transgenic *dlx4/6::GFP* zebrafish larvae (*Danio rerio*, Fig. 3.9a, [Zerucha et al., 2000; Ghanem et al., 2003]) was imaged. In this transgenic line GFP is expressed in a subset of GABAergic interneurons of the olfactory bulb, i.e. granule cells and periglomerular cells [Li et al., 2005]. Without correction the image resolution was severely compromised by distortions (Fig. 3.9c).

When correcting the aberrations introduced by the live specimen (focus depth of 50 μm) mainly astigmatism ($c_5 = -0.082 \mu\text{m}$; $c_6 = -0.306 \mu\text{m}$) and coma ($c_7 = 0.000 \mu\text{m}$; $c_8 = -0.079 \mu\text{m}$) were found (Fig. 3.9b). These values were corrected for the aberrations induced by optical elements alone. The residual aberration (0.065 μm , after 5 iterations) was not limited by measurement error but by several of the DM drive voltages having reached their limits. Even though the correction was done for the center point of the image, almost uniform improvements in image resolution and signal size were found over the whole 34 μm x 34 μm field of view (Figs. 3.9c,d), indicating that most of the wavefront aberrations are due to refractive index inhomogeneities located substantially above the focal plane. This suggests skin and cartilage overlying the brain as culprits. Experiments carried out in a fixed zebrafish larva showed similar results (data not shown).

To measure functional signals in a living wild-type zebrafish, the blood flow in the forebrain was imaged. At a focus depth of 200 μm again mainly astigmatism ($c_5 = -0.024 \mu\text{m}$, $c_6 = 0.254 \mu\text{m}$, total 0.336 μm) was found. Again, correction (to a final error of 0.095 μm after 3 iterations) was limited by the deformable mirror. The fluorescence signal from the labelled blood plasma vs. time, measured at a single spot at the center of a blood vessel (extracted from line scans through a blood vessel, Fig. 3.9e), was improved almost twofold by wavefront correction (Fig. 3.9f).

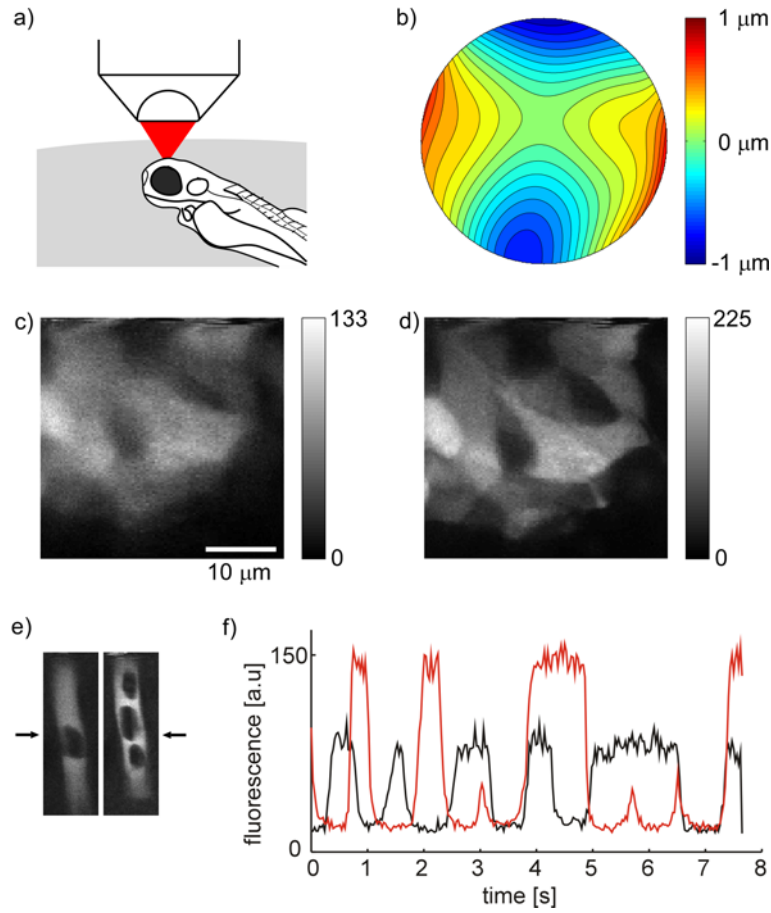
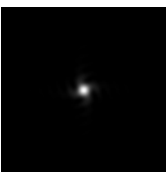


Fig. 3.9. Adaptive wavefront-correction in a living zebrafish. Orientation (a) of the zebrafish larva during imaging in the forebrain in 50 μm depth. The wavefront aberrations (contour lines are spaced by 0.1 μm) as measured by CGWS are introduced by upper tissue layers (b). Single focal plane images were recorded without (c) and with (d) correction (correction parameters determined while focussed on the center of the image). Background was subtracted and sinusoidal scan motion was linearized for display. Single focal-plane images (e) of blood vessels in the forebrain (depth 200 μm) were recorded without (left) and with correction (right). Dark regions inside the blood vessel are blood cells. Blood flow measurements (f) using line scans (positions as indicated by arrows in (e)). Plotted are the center pixel intensities as a function of time (black: without correction, red: with correction). The scale bar in (c) applies to (d) and (e) also. The gray scale of the images is proportional to the measured fluorescence intensity (arbitrary units).

Zebrafish preparation

For imaging experiments, larvae (day 3-6 post fertilization) were anesthetized by immersion in 0.16 mg/ml MS-222 (A5040, Sigma-Aldrich) and embedded in 2% low-gelling agarose (A0701, Sigma-Aldrich) with an inclination angle of the roll axis of



about 20° for better optical access [Spath et al., 1977; Li et al., 2005]. To suppress pigment formation, embryos were treated with 0.003% N-phenylthiourea (P7629, Sigma-Aldrich) starting at 10 - 20h after fertilization. Spawning and raising of zebrafish larvae was performed following standard procedures [Westerfield, 2000].

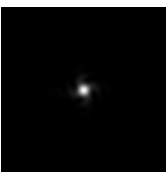
To visualize the blood plasma of zebrafish larvae 5 % (w/v) fluorescein-isothiocyanate-labeled dextran (FITC-dextran, M_r : 40 000; FD-40S, Sigma-Aldrich) in zebrafish Ringer's solution was administered to the cardiovascular system: anesthetized larvae were placed sidewise under a stereomicroscope; a glass pipette was inserted into either the heart ventricle or the yolk sac and 2-3 boluses of dye were ejected by an air pressure. Strong labelling of the cardiovascular system was observed in most animals shortly after injection under a fluorescence stereomicroscope. Individual fluorescing larvae were mounted in agarose for two-photon imaging and wavefront correction.

3.6 Discussion

It was shown that closed-loop CGWS-based wavefront correction can be applied to two-photon microscopy and allows the restoration of an almost diffraction-limited focus and hence an increase in image resolution and fluorescence signal (see section 3.3 and 3.4). Most importantly, imaging in a living biological specimen is substantially enhanced by adaptive wavefront correction (see section 3.5). It was shown that the fluorescence for “uniformly” stained samples and the more sensitive peak fluorescence can be improved significantly.

In the current implementation the speed of correction is limited mainly by the time needed to reconstruct numerically the wavefront in the virtual Shack-Hartmann sensor. The ultimate physical speed limit depends on the number of sample arm photons within the coherence gate, assuming that the number of averages needed to overcome speckle noise can be acquired quickly enough. The number of photons available depends on the length of the coherence gate (CG), focus depth in the sample, tissue properties (in particular backscattering efficiency) and, of course, on the intensity of the illumination light. Ideally, wavefront measurement, correction, and fluorescence imaging would occur pixel by pixel, either simultaneously or tightly interleaved. Under typical two-photon in-vivo imaging conditions at least a few mW, i.e. $\approx 10^{16}$ photons/s, of average laser power at the focus are needed. Of those about 10 % are scattered within the slice selected by the CG (22 μm for a coherence length of 58 μm at a mean free path (MFP) of 200 μm). However, of those 10^{15} photons/s only 1 % (calculated using the Henyey-Greenstein scattering function for an anisotropy factor of 0.95 [Henyey et al., 1941]) are scattered in a direction that falls into the objective's acceptance cone. Scattering on the way out, at a depth of, say, 5 MFPs, leads to a further 100-fold reduction so that in the end roughly 10^{11} photons/s are left for the CGWS. Since 10^5 photons are sufficient to measure the wavefront to $\lambda/50$, even when using the inefficient vSHS, a single wavefront measurement can be performed in about 1 microsecond (see section 2.3, for 441 lenses of the vSHS). Thus, wavefront measurements are not limited by the available light, even at pixel rates as large as 1 MHz.

While at least 16 measurements at different focus positions are needed to reduce speckle noise to below $\lambda/50$ (see section 2.4.3), the photons needed for a particular



precision can be spread out over different focus positions, sensibly in such a way that the shot-noise error exceeds the speckle error, which occurs when the number of photons in the sample arm for one interferogram is lower than about 10^3 (for a vSHS of our parameters, see section 2.2.1). The need to average out the speckle error is thus not limiting in speed as long as changes of focus positions can occur fast enough (for example, by an electro-optical deflector [Khayim et al., 2001]) and camera frame rates are fast enough.

For the photon-flux given above the appropriate frame rate would be about 60 MHz (16 positions times 4 images for each interferogram every microsecond), which is still above sustained camera readout rates currently available. However, since the number of parameters needed to set the DM is much smaller than the number of camera pixels on-chip processing [Monteiro et al., 2005] might ultimately provide correction parameters at MHz update-rates. Currently available deformable mirrors or spatial phase modulators are still considerably slower.

While it may not be necessary, as imaging in zebrafish (Fig. 3.9) shows, to provide pixel-by-pixel correction, it would still be desirable to correct quickly enough to follow those physiological processes that significantly affect the refractive index (for example, pulsatile blood flow) and thus cause varying wavefront distortion.

In conclusion, adaptive wavefront correction based on coherence-gated wavefront sensing should allow fast correction to study physiological processes in a variety of specimens with high spatial resolution and high contrast.



4 Summary and outlook

The need for high-resolution and quantitative microscopy has led to the combination of adaptive optics and light microscopy, in particular, confocal and multi-photon microscopy. The methods used so far to implement adaptive optics have been based on the excitation of fluorescence light and, thus, are interrelated to tissue damage through photobleaching and phototoxicity.

CGWS-based wavefront correction uses backscattered light instead and needs only a small number of photons to close the wavefront correction loop. It has been shown in this thesis, that CGWS measures the distortions, introduced by the specimen and optical elements, with high accuracy, only limited by photon and speckle noise. Although CGWS relies on the coherent property of light, the speckle-averaged wavefront of the coherence-gated backscattered light can be considered to be the incoherent superposition of spherical wavelets emitted from each scatterer within the coherence volume and then propagating back to the objective through distorting inhomogeneities of the tissue.

For several distortion-containing samples, including a living zebrafish, wavefront correction, based on CGWS, has been demonstrated to improve the resolution, fluorescence signal and, thus, the contrast of a two-photon microscope substantially. It has been estimated that the physical limit of CGWS-based wavefront correction allows restoring a diffraction-limited focus within biological specimens while simultaneously imaging by 2-photon microscopy. Only the current technical limits of wavefront correction elements and cameras limit the maximum achievable speed of wavefront correction.

Since aberrations have a particularly detrimental effect on the focus quality in high-resolution microscopy an important area of application of CGWS-based wavefront correction, besides two-photon and confocal microscopy, might be modern super-resolution techniques such as stimulated emission depletion (STED) fluorescence [Hell, 2003] and structured illumination [Neil et al., 1997] microscopy. Furthermore, the lateral focus size in high-resolution optical coherence tomography (OCT [Huang et al., 1991]) might be improved.

CGWS-based wavefront correction, as described in this thesis, can still be improved, in particular, regarding the speed of wavefront correction with current technology.

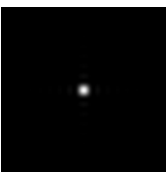
In terms of the optical setup one major drawback of the current setup is the quite slow scanning of the specimen with a translation stage. Typically, for two-photon microscopy galvanometer-driven mirrors or acousto-optic deflectors are employed for fast imaging [Iyer et al., 2006]. Both types can, in principle, be implemented using a further telescope in the sample arm.

For faster wavefront sensing the use of two cameras at both output ports of the beam splitter BSC1 (Fig. 2.2), which combines backscattered sample and reference light, in combination with a 2-step algorithm for phase shifting interferometry (PSI) might increase photon utilization and thus enhance the speed. Even the use of four cameras without temporal phase shifting is possible [Rhoadarmer, 2004].

In the current setup the interference contrast is still below what it should be, mainly due to back-reflections of lenses and objective. By using a pinhole at the focus of one of the telescopes in the sample arm these back-reflections can be partially filtered. Further, the pinhole can be utilized to reject multiply scattered light, which presumably allows deeper probing depth for CGWS. However, if the size of the pinhole is comparable to the focus size (see section 2.7), the wavefront would be spatially filtered, introducing a bias in the CGWS-measured wavefront.

The choice of a laser source for CGWS is determined by the coherence length of the emitted light. While the coherence length for the current setup is 50 μm , a shorter coherence length would be preferable: first, the spatial coherence length of the coherence-gated backscattered light becomes longer and the absolute speckle error is less; second, aberrations close to the focus can be sensed more accurately since then the extent of the coherence volume is smaller. However, for a shorter coherence length the amount of coherence-gated backscattered light is lower and thus photon noise rises. Using a higher power for the illumination light, the photon noise for CGWS-measured wavefronts can be reduced again.

Furthermore, the number of sublenses of the vSHS and the number of detector pixels have to be adjusted to match the expected wavefront aberrations and the speckle size, respectively. To minimize the wavefront error the number of sublenses is always a compromise between sufficient sampling of the wavefront and a sufficient reduction in photon noise (see section 2.3). The necessary pixel resolution of the camera for CGWS depends on the speckle size of the coherence-gated electric field. The speckle size should be sampled by at least 2 pixels in each dimension. With respect to photon noise the performance of the vSHS is not optimal and can be probably replaced by the



deterministic phase unwrapping of Volkov et al. (2003) or the virtual modal wavefront sensor [Lauterbach et al., 2006]. However the virtual modal wavefront sensor may not be able to deal with speckle noise (unpublished data).

At the end, two points on wavefront correction by CGWS in biological specimens shall be mentioned that need to be addressed in the future. First, for the described wavefront correction only the potential phase of the measured coherence-gated wavefront is reconstructed by the vSHS but not the vortex phase (see section 3.2). Therefore, investigations for various biological specimens should be carried on whether a correction of the vortex phase in addition can increase the performance of a two-photon microscope. If it is beneficial, a method needs to be developed to separate the turbulence-induced vortex phase and that part of the vortex phase that is due to the coherent superposition of coherence-gated backscattered light (see section 3.2).

Second, the question of how large the aberrations in various biological tissues are has to be addressed also. Preliminary investigations in different types of tissue [Kam et al., 2001; Schwertner et al., 2004] have shown that focus quality can be enhanced substantially when adaptive wavefront correction is applied. Further, experiments in this thesis on zebrafish demonstrated the significant increase in resolution after CGWS-based wavefront correction was applied.

Appendix A Zernike polynomials

Zernike polynomials up to the 6th radial order (nomenclature set out by Noll, 1976):

| | |
|---|---------------------------------------|
| $Z_1 = 1$ | piston |
| $Z_2 = 2 r \cos(\theta)$ | x-tilt |
| $Z_3 = 2 r \sin(\theta)$ | y-tilt |
| $Z_4 = \sqrt{3} (2r^2 - 1)$ | defocus |
| $Z_5 = \sqrt{6} r^2 \sin(2\theta)$ | 45° astigmatism |
| $Z_6 = \sqrt{6} r^2 \cos(2\theta)$ | 90° astigmatism |
| $Z_7 = \sqrt{8} (3r^3 - 2r) \sin(2\theta)$ | coma along x |
| $Z_8 = \sqrt{8} (3r^3 - 2r) \cos(2\theta)$ | coma along y |
| $Z_9 = \sqrt{8} r^3 \sin(3\theta)$ | |
| $Z_{10} = \sqrt{8} r^3 \cos(3\theta)$ | |
| $Z_{11} = \sqrt{5} (6r^4 - 6r^2 + 1)$ | 3rd order spherical |
| $Z_{12} = \sqrt{10} (4r^4 - 3r^2) \cos(2\theta)$ | |
| $Z_{13} = \sqrt{10} (4r^4 - 3r^2) \sin(2\theta)$ | |
| $Z_{14} = \sqrt{10} r^4 \cos(4\theta)$ | |
| $Z_{15} = \sqrt{10} r^4 \sin(4\theta)$ | |
| $Z_{16} = \sqrt{12} (10r^5 - 12r^3 + 3r) \cos(\theta)$ | |
| $Z_{17} = \sqrt{12} (10r^5 - 12r^3 + 3r) \sin(\theta)$ | |
| $Z_{18} = \sqrt{12} (5r^5 - 4r^3) \cos(3\theta)$ | |
| $Z_{19} = \sqrt{12} (5r^5 - 4r^3) \sin(3\theta)$ | |
| $Z_{20} = \sqrt{12} r^5 \cos(5\theta)$ | |
| $Z_{21} = \sqrt{12} r^5 \sin(5\theta)$ | |
| $Z_{22} = \sqrt{7} (20r^6 - 30r^4 + 12r^2 - 1)$ | 5rd order spherical |
| $Z_{23} = \sqrt{14} (15r^6 - 20r^4 + 6r^2) \cos(2\theta)$ | |
| $Z_{24} = \sqrt{14} (15r^6 - 20r^4 + 6r^2) \sin(2\theta)$ | |
| $Z_{25} = \sqrt{14} (6r^6 - 5r^4) \cos(4\theta)$ | |
| $Z_{26} = \sqrt{14} (6r^6 - 5r^4) \sin(4\theta)$ | |
| $Z_{27} = \sqrt{14} r^6 \cos(6\theta)$ | |
| $Z_{28} = \sqrt{14} r^6 \sin(6\theta)$ | |

Appendix B Computer-controlled setup

All relevant parts of the optical setup for iterative wavefront correction and imaging by two-photon microscopy are automatically controlled by a desktop computer (Pentium 4, 2.8 GHz, Fig. B1).

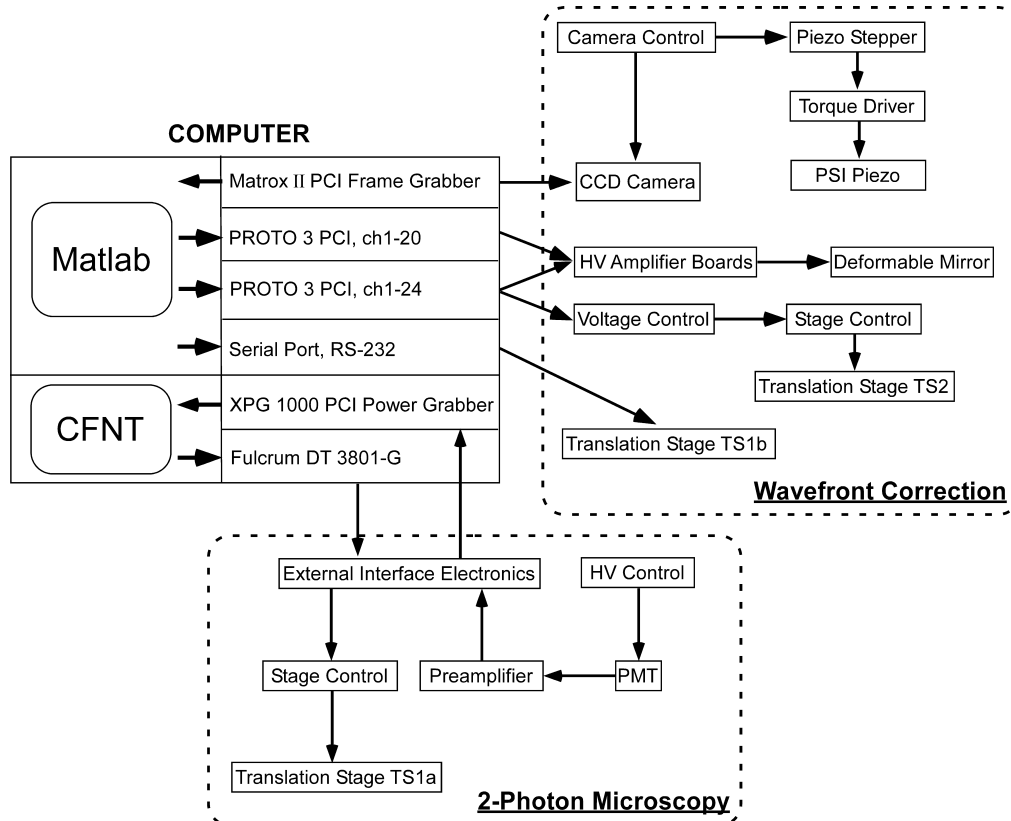


Fig. B1. Computer-controlled setup for automatic wavefront correction and imaging by two-photon microscopy. For the optical elements (TS1a, TS1b, TS2, PMT, CCD Camera and DM) used here see Fig. 2.2.

For two-photon microscopy the fluorescence signal collected by the photo multiplier tube (PMT, mounted on a socket assembly providing the high voltage, C6270, Hamamatsu), whose sensitivity can be adjusted by the high-voltage (HV) control, is fed to a custom-designed external interface digitization electronics after it is pre-amplified. The digital outputs from that system are processed via the XPG-1000 Power Grabber board by a program called CFNT. The voltage signals as well as the necessary synchronization signals are generated on another plug-in board (Fulcrum DT3801-G).

Since CFNT was originally written to drive a fast galvanometer-driven scan mirror, some fixed parameters were changed to control the translation stage TS1a for scanning the specimen. For scanning in x-direction a sinusoidal signal with a period of 30 ms was applied, where only for half of the period fluorescence was recorded. A sawtooth signal with a period of 3.8 s was applied to the y-direction to record a two dimensional image. It was checked that the amplitude of the signals in x- and y-direction are the same by detecting asymmetries among images, e.g. of fluorescent beads, recorded for an interchange of the voltage signals driving the translation stage. For an absolute calibration of the size of the recorded images the fact was used that the translation stage TS1a is mounted onto an already calibrated xyz-stage (TS1b, Sutter Instruments), which is used for coarse displacements of the specimen. The voltage amplitudes are controlled by the zoom factor (defined parameter for CFNT), for which a factor of 16 corresponds to an image size of 6 μm by 6 μm . An independent interferometric calibration with a controllable tip/tilt mirror, on which the deformable mirror was mounted, confirmed the former calibration.

The iterative wavefront correction, comprising devices for CGWS and wavefront correction, are controlled by Matlab (The MathWorks, Inc.). Interferograms recorded with the video camera are read in via the Meteor II frame grabber board. The frame clock of 60 Hz is provided by a camera control box, which provides also the clock for the piezo stepper. This device generates the necessary phase steps of $\lambda/4$ for each full-frame according to the RS-170 standard (for further details see [Feierabend, 2004]). To calibrate the fine adjustment of the piezo stepper several quadruplets of interferograms with a mirror sample were recorded and, thereby, the mean phase step for each pixel of the camera within the aperture was calculated (see Carré algorithm, [Malacara, 1992]). If the mean phase step was $\lambda/4$, the piezo stepper was correctly tuned.

For CGWS the recorded interferograms were processed by the vSHS, implemented as a Matlab code, and then the drive voltages for the 37 electrodes of the DM were determined. Via two PCI cards (PROTO 3, both have nominally 20 channels, but one card is slightly changed to provide 4 further channels) and two amplifier boards (maximum output power 300 V) the drive voltages were applied to the DM. Since 4 further channels were available that were not needed for the control of the DM further automatization was possible. Therefore, also the piezo-driven translation stage TS2,

which adjusts the length of the reference arm to correct for a measured defocus, was computer-controlled.

Appendix C Propagation of polarized light in the sample arm

For CGWS the interference of reference and sample light in terms of polarization is considered by the function $W_{Pol}^{(k)} = \mathbf{p}_{Ref}^* \cdot \mathbf{p}_S^{(k)}$ (see Eq. (2.6)), where \mathbf{p}_{Ref} is the polarization of the reference light and $\mathbf{p}_S^{(k)}$ the polarization of light backscattered at a scatterer k .

In this appendix it will be shown how the polarization in the sample arm changes under refraction due to a generic objective and by Mie scattering within the sample. To keep it simple, the refraction by the objective is described by a prism [Mansuripur, 1986; Rohrbach et al., 2002].

First, the light rays were traced through the sample arm and for each change of direction a new local basis $(\mathbf{e}_g, \mathbf{e}_\varphi, \mathbf{e}_r)$ was defined (Fig. C1) in relation to fixed global basis $(\mathbf{e}_x, \mathbf{e}_y, \mathbf{e}_z)$ with $\mathbf{e}_x \times \mathbf{e}_y = \mathbf{e}_z$. For each local basis was $\mathbf{e}_g^{(i)} \times \mathbf{e}_\varphi^{(i)} = \mathbf{e}_r^{(i)}$, where $\mathbf{e}_g^{(i)}$ lay in the plane spanned up by two adjacent directions of propagating. An exception is basis 1, which is the connection from the local basis to the global one.

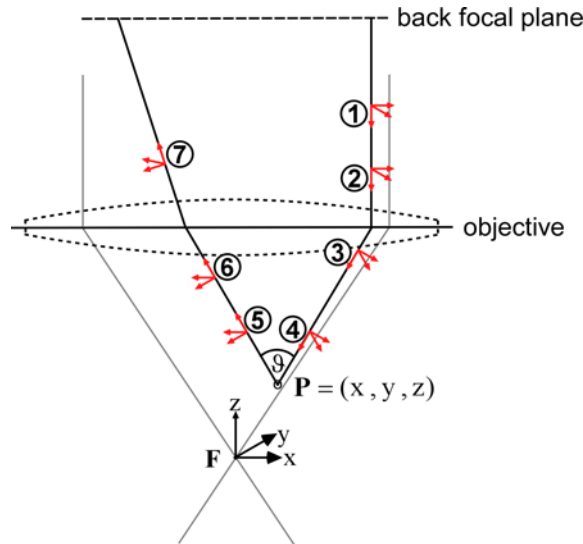


Fig. C1. Propagation of the polarization through sample arm. For each step the local basis is depicted in red. The global basis is shown at the focus. The scattering angle is θ .

Basis 1: for the incoming light rays

$$\mathbf{e}_r^{(1)} = -\mathbf{e}_z$$

$$\mathbf{e}_\phi^{(1)} = -\mathbf{e}_y$$

$$\mathbf{e}_g^{(1)} = \mathbf{e}_x$$

Basis 2: rotation of $\mathbf{e}_g^{(1)}$ into the plane of refraction (spanned up by $\mathbf{e}_r^{(1)}$ and $\mathbf{e}_r^{(3)}$)

$$\mathbf{e}_r^{(2)} = \mathbf{e}_r^{(1)}$$

$$\mathbf{e}_\phi^{(2)} = \mathbf{e}_\phi^{(3)}$$

$$\mathbf{e}_g^{(2)} = \frac{\mathbf{e}_\phi^{(2)} \times \mathbf{e}_r^{(2)}}{|\mathbf{e}_\phi^{(2)} \times \mathbf{e}_r^{(2)}|}$$

Basis 3: after passing the objective (scatterer at P(x,y,z))

$$\mathbf{e}_r^{(3)} = \frac{-\text{sgn}(z)}{\sqrt{x^2 + y^2 + z^2}} (x \cdot \mathbf{e}_x + y \cdot \mathbf{e}_y + z \cdot \mathbf{e}_z)$$

$$\mathbf{e}_\phi^{(3)} = \frac{\mathbf{e}_r^{(1)} \times \mathbf{e}_r^{(3)}}{|\mathbf{e}_r^{(1)} \times \mathbf{e}_r^{(3)}|}$$

$$\mathbf{e}_g^{(3)} = \frac{\mathbf{e}_\phi^{(3)} \times \mathbf{e}_r^{(3)}}{|\mathbf{e}_\phi^{(3)} \times \mathbf{e}_r^{(3)}|}$$

Basis 4: rotation of $\mathbf{e}_g^{(3)}$ into the scattering plane (spanned up by $\mathbf{e}_r^{(3)}$ and $\mathbf{e}_r^{(5)}$)

$$\mathbf{e}_r^{(4)} = \mathbf{e}_r^{(3)}$$

$$\mathbf{e}_\phi^{(4)} = \frac{\mathbf{e}_r^{(4)} \times \mathbf{e}_r^{(5)}}{|\mathbf{e}_r^{(4)} \times \mathbf{e}_r^{(5)}|}$$

$$\mathbf{e}_g^{(4)} = \frac{\mathbf{e}_\phi^{(4)} \times \mathbf{e}_r^{(4)}}{|\mathbf{e}_\phi^{(4)} \times \mathbf{e}_r^{(4)}|}$$

Basis 5: after scattering in the direction \mathbf{w}

$$\mathbf{e}_r^{(5)} = w_x \cdot \mathbf{e}_x + w_y \cdot \mathbf{e}_y + w_z \cdot \mathbf{e}_z$$

$$\mathbf{e}_\phi^{(5)} = \mathbf{e}_\phi^{(4)}$$

$$\mathbf{e}_g^{(5)} = \frac{\mathbf{e}_\phi^{(5)} \times \mathbf{e}_r^{(5)}}{|\mathbf{e}_\phi^{(5)} \times \mathbf{e}_r^{(5)}|}$$

Basis 6: rotation of $\mathbf{e}_g^{(5)}$ into the plane of refraction (spanned up by $\mathbf{e}_r^{(5)}$ and $\mathbf{e}_r^{(7)}$)

$$\mathbf{e}_r^{(6)} = \mathbf{e}_r^{(5)}$$

$$\mathbf{e}_\phi^{(6)} = \mathbf{e}_\phi^{(7)}$$

$$\mathbf{e}_g^{(6)} = \frac{\mathbf{e}_\phi^{(6)} \times \mathbf{e}_r^{(6)}}{|\mathbf{e}_\phi^{(6)} \times \mathbf{e}_r^{(6)}|}$$

Basis 7: after passing the objective on the way back (f_{back} is the back focal length)

$$\mathbf{e}_r^{(7)} = (x - \frac{z}{w_z} w_x) \cdot \mathbf{e}_x + (y - \frac{z}{w_z} w_y) \cdot \mathbf{e}_y + f_{back} \cdot \mathbf{e}_z$$

$$\mathbf{e}_\phi^{(7)} = \frac{\mathbf{e}_r^{(5)} \times \mathbf{e}_r^{(7)}}{|\mathbf{e}_r^{(5)} \times \mathbf{e}_r^{(7)}|}$$

$$\mathbf{e}_g^{(7)} = \frac{\mathbf{e}_\phi^{(7)} \times \mathbf{e}_r^{(7)}}{|\mathbf{e}_\phi^{(7)} \times \mathbf{e}_r^{(7)}|}$$

In the next step, the polarization, described by a two dimensional vector $\begin{pmatrix} a \\ b \end{pmatrix}$, is

traced for each change of the local basis (Jones formalism, [Hecht, 1990]). The polarization of the incoming light, expressed in the global basis, is

$\mathbf{p}_{ini} = a_{ini} \cdot \mathbf{e}_x + b_{ini} \cdot \mathbf{e}_y$, which is the same as the polarization of the reference light

\mathbf{p}_{Ref} .

Global Basis \rightarrow Basis 1: Transformation into local basis

$$\begin{pmatrix} a_1 \\ b_1 \end{pmatrix} = \begin{pmatrix} 1 & 0 \\ 0 & -1 \end{pmatrix} \cdot \begin{pmatrix} a_{ini} \\ b_{ini} \end{pmatrix} \text{ with } \mathbf{p}_{ini} = a_{ini} \cdot \mathbf{e}_x + b_{ini} \cdot \mathbf{e}_y \text{ and } \mathbf{p}_k^{(1)} = a_1 \cdot \mathbf{e}_g^{(1)} + b_1 \cdot \mathbf{e}_\phi^{(1)}$$

Basis 1 → Basis 2: Rotation into plane of refraction

$$\begin{pmatrix} a_2 \\ b_2 \end{pmatrix} = \begin{pmatrix} \cos(\beta) & \sin(\beta) \\ -\sin(\beta) & \cos(\beta) \end{pmatrix} \cdot \begin{pmatrix} a_1 \\ b_1 \end{pmatrix} \quad \text{with } \cos(\beta) = \mathbf{e}_g^{(2)} \cdot \mathbf{e}_g^{(1)} \text{ and } \sin(\beta) = \mathbf{e}_g^{(2)} \cdot \mathbf{e}_\varphi^{(1)}$$

Basis 2 → Basis 3: Change due to objective [Mansuripur, 1986]

$$\begin{pmatrix} a_3 \\ b_3 \end{pmatrix} = \begin{pmatrix} 1 & 0 \\ 0 & 1 \end{pmatrix} \cdot \begin{pmatrix} a_2 \\ b_2 \end{pmatrix}$$

Basis 3 → Basis 4: Rotation into scattering plane

$$\begin{pmatrix} a_4 \\ b_4 \end{pmatrix} = \begin{pmatrix} \cos(\varphi) & \sin(\varphi) \\ -\sin(\varphi) & \cos(\varphi) \end{pmatrix} \cdot \begin{pmatrix} a_3 \\ b_3 \end{pmatrix} \quad \text{with } \cos(\varphi) = \mathbf{e}_g^{(4)} \cdot \mathbf{e}_g^{(3)} \text{ and } \sin(\varphi) = \mathbf{e}_g^{(4)} \cdot \mathbf{e}_\varphi^{(3)}$$

Basis 4 → Basis 5: Mie scattering functions $S_1(\mathcal{G})$ and $S_2(\mathcal{G})$ [Bohren, 1983]

$$\begin{pmatrix} a_5 \\ b_5 \end{pmatrix} = \begin{pmatrix} S_2(\mathcal{G}) & 0 \\ 0 & S_1(\mathcal{G}) \end{pmatrix} \cdot \begin{pmatrix} a_4 \\ b_4 \end{pmatrix} \quad \text{with } \cos(\mathcal{G}) = \mathbf{e}_r^{(4)} \cdot \mathbf{e}_r^{(5)}$$

Basis 5 → Basis 6: Rotation into plane of refraction

$$\begin{pmatrix} a_6 \\ b_6 \end{pmatrix} = \begin{pmatrix} \cos(\varepsilon) & \sin(\varepsilon) \\ -\sin(\varepsilon) & \cos(\varepsilon) \end{pmatrix} \cdot \begin{pmatrix} a_5 \\ b_5 \end{pmatrix} \quad \text{with } \cos(\varepsilon) = \mathbf{e}_g^{(6)} \cdot \mathbf{e}_g^{(5)} \text{ and } \sin(\varepsilon) = \mathbf{e}_g^{(6)} \cdot \mathbf{e}_\varphi^{(5)}$$

Basis 6 → Basis 7: Change due to objective [Mansuripur, 1986]

$$\begin{pmatrix} a_7 \\ b_7 \end{pmatrix} = \begin{pmatrix} 1 & 0 \\ 0 & 1 \end{pmatrix} \cdot \begin{pmatrix} a_6 \\ b_6 \end{pmatrix}$$

Basis 7 → Global Basis

$$\begin{pmatrix} a_f \\ b_f \end{pmatrix} = \begin{pmatrix} \vec{e}_g^{(7)} \cdot \vec{e}_x & \vec{e}_\phi^{(7)} \cdot \vec{e}_x \\ \vec{e}_g^{(7)} \cdot \vec{e}_y & \vec{e}_\phi^{(7)} \cdot \vec{e}_y \end{pmatrix} \cdot \begin{pmatrix} a_7 \\ b_7 \end{pmatrix} \text{ with } \mathbf{p}_S^{(k)} = a_f \cdot \mathbf{e}_x + b_f \cdot \mathbf{e}_y$$

Since a_f and b_f are related to a_{ini} and b_{ini} , the polarization weight $W_{Pol}^{(k)} = \mathbf{p}_{Ref}^* \cdot \mathbf{p}_S^{(k)}$ can be calculated for each scattered light ray.

Appendix D Glass capillary induced astigmatism

If the focus is placed at the center of the capillary in a cross-section perpendicular to the capillary axis, no refraction occurs but in a cross section parallel to the axis, the light rays are refracted and the focus is displaced downwards (Fig. 3.7). The displacement V is

$$V = D \frac{\sin(\alpha - \beta)}{\sin(\alpha) \cos(\beta)},$$

where D is the wall thickness of the capillary, α the angle of incidence and β the angle of refraction. Using Snell's law β can be replaced by

$$\beta = \arcsin\left(\frac{n_w}{n_g} \sin(\alpha)\right),$$

where n_w and n_g are the refractive indices of water and glass, respectively. The focus displacement V corresponds to a shift in the measured Zernike defocus Δc_4 of [Feierabend, 2004]

$$\Delta c_4 = \frac{R^2}{4\sqrt{3} n_w f^2} V.$$

The radius of the aperture is denoted by R and the back focal length of the objective is f . Both cross sections along the x- and y-axis through an astigmatic wavefront with Zernike mode c_6 show two equally but opposite curvatures, which correspond to a Zernike defocus

$$c_4 = \pm \frac{\sqrt{6}}{2\sqrt{3}} c_6|_{x,y}$$

Thus, the expected astigmatism due to a focus displacement V in one cross-section through the capillary but not in the other yields

$$c_6 = \frac{1}{\sqrt{2}} \Delta c_4 = D \frac{R^2}{4\sqrt{6} n_w f^2} \frac{\sin(\alpha - \beta)}{\sin(\alpha) \cos(\beta)}.$$

For an objective (63x, 0.9W) and a wall thickness of 24 μm ($n_G=1.51$) the expected Zernike coefficient for astigmatism is $c_6 = 0.28 \mu\text{m}$.

5 Literature

- Aksenov, V., Banakh, V., et al. (1998). **"Potential and vortex features of optical speckle fields and visualization of wave-front singularities"**, Applied Optics **37**(21): 4536-4540.
- Apostol, A. and Dogariu, A. (2005). **"Non-Gaussian statistics of optical near-fields"**, Physical Review E **72**(2).
- Babcock, H. W. (1953). **"The possibility of compensating astronomical seeing"**, Publications of the Astronomical Society of the Pacific **65**: 229-236.
- Barchers, J. D., Fried, D. L., et al. (2002). **"Evaluation of the performance of Hartmann sensors in strong scintillation"**, Applied Optics **41**(6): 1012-1021.
- Beckers, J. M. (1988). **Increasing the size of the isoplanatic patch with multiconjugate adaptive optics**. Very Large Telescopes and their Instrumentation, ESO Conference and Workshop Proceedings, Garching, Germany.
- Beuthan, J., Minet, O., et al. (1996). **"The spatial variation of the refractive index in biological cells"**, Physics in Medicine and Biology **41**(3): 369-382.
- Bohren, C. F., Huffmann, D. R. (1983). **Absorption and Scattering by Small Particles**, John Wiley & Sons, Inc.
- Booth, M. J. (2006). **"Wave front sensor-less adaptive optics: a model-based approach using sphere packings"**, Optics Express **14**(4): 1339-1352.
- Booth, M. J., Neil, M. A. A., et al. (2002). **"Adaptive aberration correction in a confocal microscope"**, Proceedings of the National Academy of Sciences of the United States of America **99**(9): 5788-5792.
- Booth, M. J., Schwertner, M., et al. (2005). **"Specimen-induced aberrations and adaptive optics for microscopy"**, Proceedings of SPIE - the International Society for Optical Engineering **5894** (Advanced Wavefront Control: Methods, Devices and Applications III, edited by Mark T. Gruneisen, John D. Gonglewski, Michael K. Giles).
- Booth, M. J., Schwertner, M., et al. (2006). **"Predictive aberration correction for multilayer optical data storage"**, Applied Physics Letters **88**(3).
- Born, M. and Wolf, E. (1999). **Principles of Optics**. Cambridge, U.K., Cambridge University Press.
- Buffington, A., Crawford, F. S., et al. (1977). **"1st Observatory Results with an Image-Sharpening Telescope"**, Journal of the Optical Society of America **67**(3): 304-305.
- Chen, C. W. and Zebker, H. A. (2000). **"Network approaches to two-dimensional phase unwrapping: intractability and two new algorithms"**, Journal of the Optical Society of America A **17**(3): 401-414.
- Cicchi, R., Pavone, F. S., et al. (2005). **"Contrast and depth enhancement in two-photon microscopy of human skin ex vivo by use of optical clearing agents"**, Optics Express **13**(7): 2337-2344.

- Cubalchini, R. (1979). **"Modal Wavefront Estimation from Phase Derivative Measurements"**, Journal of the Optical Society of America **69**(7): 973-977.
- Denk, W., Strickler, J. H., et al. (1990). **"Two-Photon Laser Scanning Fluorescence Microscopy"**, Science **248**(4951): 73-76.
- Denk, W. and Svoboda, K. (1997). **"Photon upmanship: Why multiphoton imaging is more than a gimmick"**, Neuron **18**(3): 351-357.
- Diaspro, A., Federici, F., et al. (2002). **"Influence of refractive-index mismatch in high-resolution three-dimensional confocal microscopy"**, Applied Optics **41**(4): 685-690.
- Dreher, A. W., Bille, J. F., et al. (1989). **"Active Optical Depth Resolution Improvement of the Laser Tomographic Scanner"**, Applied Optics **28**(4): 804-808.
- Drexler, W. (2004). **"Ultrahigh-resolution optical coherence tomography"**, Journal of Biomedical Optics **9**(1): 47-74.
- Drezek, R., Dunn, A., et al. (1999). **"Light scattering from cells: finite-difference time-domain simulations and goniometric measurements"**, Applied Optics **38**(16): 3651-3661.
- Dunn, A. (1997). **"Light Scattering Properties of Cells"**, University of Texas, Austin.
- Feierabend, M. (2004). **"Coherence-gated wave-front sensing in strongly scattering samples"**, University of Heidelberg.
- Feierabend, M., Rueckel, M., et al. (2004). **"Coherence-gated wave-front sensing in strongly scattering samples"**, Optics Letters **29**(19): 2255-2257.
- Fercher, A. F., Drexler, W., et al. (2003). **"Optical coherence tomography - principles and applications"**, Reports on Progress in Physics **66**(2): 239-303.
- Fernandez, E. J. and Artal, P. (2003). **"Membrane deformable mirror for adaptive optics: performance limits in visual optics"**, Optics Express **11**(9): 1056-1069.
- Fried, D. L. (1998). **"Branch point problem in adaptive optics"**, Journal of the Optical Society of America A **15**(10): 2759-2768.
- Fried, D. L. and Vaughn, J. L. (1992). **"Branch Cuts in the Phase Function"**, Applied Optics **31**(15): 2865-2882.
- Fujii, H. and Asakura, T. (1974). **"Effect of Surface-Roughness on Statistical Distribution of Image Speckle Intensity"**, Optics Communications **11**(1): 35-38.
- Gens, R. (2003). **"Two-dimensional phase unwrapping for radar interferometry: developments and new challenges"**, International Journal of Remote Sensing **24**(4): 703-710.
- Gerth, K. (2005). **Ernst Abbe: Scientist, Entrepreneur, Social Reformer**. Jena - Quedlinburg, Verlag Dr. Bussert & Stadeler.
- Ghanem, N., Jarinova, O., et al. (2003). **"Regulatory roles of conserved intergenic domains in vertebrate Dlx bigene clusters"**, Genome Res **13**(4): 533-43.

- Ghiglia, D. C., Mastin, G. A., et al. (1987). "**Cellular-Automata Method for Phase Unwrapping**", Journal of the Optical Society of America A **4**(1): 267-280.
- Gibson, S. F. and Lanni, F. (1991). "**Experimental Test of an Analytical Model of Aberration in an Oil-Immersion Objective Lens Used in 3-Dimensional Light-Microscopy**", Journal of the Optical Society of America A **8**(10): 1601-1613.
- Gill, P. E., Murray, W., Wright, M.H. (1995). **Practical optimization**. San Diego, Academic Press, Inc.
- Goodman, J. W. (1975). "**Dependence of Image Speckle Contrast on Surface-Roughness**", Optics Communications **14**(3): 324-327.
- Goodman, J. W. (1976). "**Some Fundamental Properties of Speckle**", Journal of the Optical Society of America **66**(11): 1145-1150.
- Goodman, J. W. (2000). **Statistical Optics**. New York, John Wiley and Sons.
- Goodman, J. W. (2005). **Speckle Phenomena in Optics: Theory and Applications Version 5.0**, preliminary version of published book.
- Göppert-Mayer, M. (1931). "**Über Elementarakte mit zwei Quantensprüngen**", Annalen der Physik **9**: 273-294.
- Hardy, J. W. (1978). "**Active Optics - New Technology for Control of Light**", Proceedings of the IEEE **66**(6): 651-697.
- Hardy, J. W. (1998). **Adaptive Optics For Astronomical Telescopes**. Oxford University Press.
- Hecht, E. (1990). **Optics**. Reading, Massachusetts, Addison-Wesley Publishing Company.
- Hell, S. W. (2003). "**Toward fluorescence nanoscopy**", Nature Biotechnology **21**(11): 1347-1355.
- Helmchen, F. and Denk, W. (2005). "**Deep tissue two-photon microscopy**", Nature Methods **2**(12): 932-940.
- Helmchen, F. and Waters, J. (2002). "**Ca²⁺ imaging in the mammalian brain in vivo**", European Journal of Pharmacology **447**(2-3): 119-129.
- Heney, L. G. and Greenstein, J. L. (1941). "**Diffuse radiation in the galaxy**", Astrophysical Journal **93**(1): 70-83.
- Hsu, W. Y. and Barakat, R. (1994). "**Stratton-Chu Vectorial Diffraction of Electromagnetic-Fields by Apertures with Application to Small-Fresnel-Number Systems**", Journal of the Optical Society of America A **11**(2): 623-629.
- Huang, D., Swanson, E. A., et al. (1991). "**Optical Coherence Tomography**", Science **254**(5035): 1178-1181.
- Iyer, V., Hoogland, T. M., et al. (2006). "**Fast functional imaging of single neurons using random-access multiphoton (RAMP) microscopy**", J Neurophysiol **95**(1): 535-45.

- Kam, Z., Hanser, B., et al. (2001). "**Computational adaptive optics for live three-dimensional biological imaging**", Proceedings of the National Academy of Sciences of the United States of America **98**(7): 3790-3795.
- Karamata, B., Laubscher, M., et al. (2005). "**Multiple scattering in optical coherence tomography. I. Investigation and modeling**", Journal of the Optical Society of America A **22**(7): 1369-1379.
- Khayim, T., Maruko, A., et al. (2001). "**Ultrafast unidirectional beam deflection using an electrooptic traveling phase grating with periodic domain inversion**", IEEE Journal of Quantum Electronics **37**(8): 964-969.
- Klinger, J., Martin, H., et al. (2001). "**Experiments on induced modulational instability of an incoherent optical beam**", Optics Letters **26**(5): 271-273.
- Kuehl, T. and Bock, R., et al. (2005). "**PHELIX – Status and First Experiments**", Hyperfine Interactions.
- Larichev, A. V., Ivanov, P. V., et al. (2001). "**Measurement of eye aberrations in a speckle field**", Quantum Electronics **31**(12): 1108-1112.
- Lauterbach, M. A., Ruckel, M., et al. (2006). "**Light-efficient, quantum-limited interferometric wavefront estimation by virtual mode sensing**", Optics Express **14**(9): 3700-3714.
- Li, J., Mack, J. A., et al. (2005). "**Early development of functional spatial maps in the zebrafish olfactory bulb**", Journal of Neuroscience **25**(24): 5784-5795.
- Liang, J. Z., Grimm, B., et al. (1994). "**Objective Measurement of Wave Aberrations of the Human Eye with the Use of a Hartmann-Shack Wave-Front Sensor**", Journal of the Optical Society of America A **11**(7): 1949-1957.
- Liang, J. Z., Williams, D. R., et al. (1997). "**Supernormal vision and high-resolution retinal imaging through adaptive optics**", Journal of the Optical Society of America A **14**(11): 2884-2892.
- Lu, Q., Gan, X. S., et al. (2004). "**Monte Carlo modeling of optical coherence tomography imaging through turbid media**", Applied Optics **43**(8): 1628-1637.
- Malacara, D. (1992). **Optical Shop testing**. New York, John Wiley & Sons, Inc.
- Mansuripur, M. (1986). "**Distribution of Light at and near the Focus of High-Numerical-Aperture Objectives**", Journal of the Optical Society of America A **3**(12): 2086-2093.
- Marsh, P. N., Burns, D., et al. (2003). "**Practical implementation of adaptive optics in multiphoton microscopy**", Optics Express **11**(10): 1123-1130.
- Medeck, H., Tejnil, E., et al. (1996). "**Phase-shifting point diffraction interferometer**", Optics Letters **21**(19): 1526-1528.
- Mie, G. (1908). "**Articles on the optical characteristics of turbid tubes, especially colloidal metal solutions.**" Annalen der Physik **25**(3): 377-445.
- Minsky, M. (1961). "**Microscopy Apparatus**", U.S. Patent 3013467.

- Mizrahi, A., Crowley, J. C., et al. (2004). "**High-resolution in vivo imaging of hippocampal dendrites and spines**", *Journal of Neuroscience* **24**(13): 3147-3151.
- Monteiro, D. W. L., Nirmaier, T., et al. (2005). "**Fast Hartmann-Shack wavefront sensors manufactured in standard CMOS technology**", *Sensors Journal, IEEE* **5**(5): 976-982.
- Mourant, J. R., Freyer, J. P., et al. (1998). "**Mechanisms of light scattering from biological cells relevant to noninvasive optical-tissue diagnostics**", *Applied Optics* **37**(16): 3586-3593.
- Mourant, J. R., Johnson, T. M., et al. (2002). "**Polarized angular dependent spectroscopy of epithelial cells and epithelial cell nuclei to determine the size scale of scattering structures**", *Journal of Biomedical Optics* **7**(3): 378-387.
- Neil, M. A. A., Juskaitis, R., et al. (2000). "**Adaptive aberration correction in a two-photon microscope**", *Journal of Microscopy* **200**: 105-108.
- Neil, M. A. A., Juskaitis, R., et al. (1997). "**Method of obtaining optical sectioning by using structured light in a conventional microscope**", *Optics Letters* **22**(24): 1905-1907.
- Noll, R. J. (1976). "**Zernike Polynomials and Atmospheric-Turbulence**", *Journal of the Optical Society of America* **66**(3): 207-211.
- Nye, J. F. and Berry, M. V. (1974). "**Dislocations in Wave Trains**", *Proceedings of the Royal Society of London Series A* **336**(1605): 165-190.
- Ota, T., Sugiura, T., et al. (2003). "**Enhancement of laser trapping force by spherical aberration correction using a deformable mirror**", *Japanese Journal of Applied Physics Part 2-Letters* **42**(6B): L701-L703.
- Oughstun, K. E. (1981). "**Intracavity adaptive optic compensation of phase aberrations. I: Analysis**", *Journal of the Optical Society of America* **71**(7): 862 - 872.
- Paterson, C., Munro, I., et al. (2000). "**A low cost adaptive optics system using a membrane mirror**", *Optics Express* **6**(9): 175-185.
- Piederriere, Y., Cariou, J., et al. (2004). "**Scattering through fluids: speckle size measurement and Monte Carlo simulations close to and into the multiple scattering**", *Optics Express* **12**(1): 176-188.
- Primmerman, C. A., Price, T. R., et al. (1995). "**Atmospheric-Compensation Experiments in Strong-Scintillation Conditions**", *Applied Optics* **34**(12): 2081-2088.
- Primot, J., Rousset, G., et al. (1990). "**Deconvolution from Wave-Front Sensing - a New Technique for Compensating Turbulence-Degraded Images**", *Journal of the Optical Society of America A* **7**(9): 1598-1608.
- Ragazzoni, R. (1996). "**Pupil plane wavefront sensing with an oscillating prism**", *Journal of Modern Optics* **43**(2): 289-293.
- Rhoadarmer, T. A. (2004). "**Development of self-referencing interferometer wavefront sensor**", *Proceedings of SPIE - the International Society for Optical Engineering* **5553**: 112.

- Roddiar, F. (1988). "**Curvature Sensing and Compensation - a New Concept in Adaptive Optics**", Applied Optics **27**(7): 1223-1225.
- Roggemann, M. C. and Koivunen, A. C. (2000). "**Wave-front sensing and deformable-mirror control in strong scintillation**", Journal of the Optical Society of America A **17**(5): 911-919.
- Rohrbach, A. and Stelzer, E. H. K. (2002). "**Three-dimensional position detection of optically trapped dielectric particles**", Journal of Applied Physics **91**(8): 5474-5488.
- Rueckel, M. and Denk, W. (2005). **Polarization Effects in Coherence-gated Wave-front Sensing**. Adaptive Optics: Analysis and Methods/Computational Optical Sensing and Imaging/Information Photonics/Signal Recovery and Synthesis Topical Meetings on CD-ROM (The Optical Society of America, Washington, DC, 2005), AThC4.
- Rueckel, M. and Denk, W. (2006a). **Coherence-gated wavefront sensing using a virtual Shack-Hartmann sensor**. Advanced Wavefront Control: Methods, Devices, and Applications IV, San Diego, Proceedings of SPIE.
- Rueckel, M., Mack-Bucher, J., et al. (2006b). "**Adaptive wavefront correction in two-photon microscopy using coherence-gated wavefront sensing**", submitted.
- Schmitt, J. M. (1999). "**Optical coherence tomography (OCT): A review**", IEEE Journal of Selected Topics in Quantum Electronics **5**(4): 1205-1215.
- Schmitt, J. M. and Kumar, G. (1996). "**Turbulent nature of refractive-index variations in biological tissue**", Optics Letters **21**(16): 1310-1312.
- Schmitt, J. M. and Kumar, G. (1998). "**Optical scattering properties of soft tissue: a discrete particle model**", Applied Optics **37**(13): 2788-2797.
- Schwertner, M., Booth, M. J., et al. (2004). "**Characterizing specimen induced aberrations for high NA adaptive optical microscopy**", Optics Express **12**(26): 6540-6552.
- Shack, R. V. and Platt, B. C. (1971). "**Lenticular Hartmann-screen**", Optical Sciences Center Newsletter **5**(1): 15-16.
- Sheppard, C. J. R. and Gu, M. (1991). "**Aberration Compensation in Confocal Microscopy**", Applied Optics **30**(25): 3563-3568.
- Sheppard, C. J. R. and Torok, P. (1997). "**Effects of specimen refractive index on confocal imaging**", Journal of Microscopy **185**: 366-374.
- Sherman, L., Ye, J. Y., et al. (2002). "**Adaptive correction of depth-induced aberrations in multiphoton scanning microscopy using a deformable mirror**", Journal of Microscopy **206**: 65-71.
- Shvartsman, N. and Freund, I. (1994). "**Vortices in Random Wave-Fields - Nearest-Neighbor Anticorrelations**", Physical Review Letters **72**(7): 1008-1011.
- Siegman, A. E. (1986). **Lasers**. Mill Valley, California, University Science Books.

- Späth, M. and Schweickert, W. (1977). "**Effect of Metacaine (Ms-222) on Activity of Efferent and Afferent Nerves in Teleost Lateral-Line System**", *Naunyn-Schmiedeberg's Archives of Pharmacology* **297**(1): 9-16.
- Svoboda, K., Denk, W., et al. (1997). "**In vivo dendritic calcium dynamics in neocortical pyramidal neurons**", *Nature* **385**(6612): 161-165.
- Tatarski, V. I. (1961). **Wave Propagation in a Turbulent Medium**. New York, McGraw-Hill Books.
- Theer, P., Hasan, M. T., et al. (2003). "**Two-photon imaging to a depth of 1000 μm in living brains by use of a $\text{Ti:Al}_2\text{O}_3$ regenerative amplifier**", *Optics Letters* **28**(12): 1022-1024.
- Thomas, S. (2004). "**Optimized centroid computing in a Shack-Hartmann sensor**", *Proceedings of SPIE - the International Society for Optical Engineering* **5490** (Advancements in Adaptive Optics; Domenico Bonaccini Calia, Brent L. Ellerbroek, Roberto Ragazzoni; Eds.): p. 1238-1246.
- Tuchin, V. V. (2005). "**Optical clearing of tissues and blood using the immersion method**", *Journal of Physics D-Applied Physics* **38**(15): 2497-2518.
- Tyler, G. A. (2000). "**Reconstruction and assessment of the least-squares and slope discrepancy components of the phase**", *Journal of the Optical Society of America A* **17**(10): 1828-1839.
- Uozumi, J. and Asakura, T. (1981). "**The 1st-Order Statistics of Partially Developed Non-Gaussian Speckle Patterns**", *Journal of Optics-Nouvelle Revue D Optique* **12**(3): 177-186.
- Vdovin, G. and Sarro, P. M. (1995). "**Flexible Mirror Micromachined in Silicon**", *Applied Optics* **34**(16): 2968-2972.
- Volkov, V. V. and Zhu, Y. M. (2003). "**Deterministic phase unwrapping in the presence of noise**", *Optics Letters* **28**(22): 2156-2158.
- Vorontsov, M. A. and Carhart, G. W. (2002). "**Adaptive phase distortion correction in strong speckle-modulation conditions**", *Optics Letters* **27**(24): 2155-2157.
- Vorontsov, M. A. and Kolosov, V. (2005). "**Target-in-the-loop beam control: basic considerations for analysis and wave-front sensing**", *Journal of the Optical Society of America A* **22**(1): 126-141.
- Welsh, B. M. and Gardner, C. S. (1989). "**Performance Analysis of Adaptive-Optics Systems Using Laser Guide Stars and Slope Sensors**", *Journal of the Optical Society of America A* **6**(12): 1913-1923.
- Westerfield, M. (2000). **The zebrafish book. A guide for the laboratory use of zebrafish (Danio rerio)**. Eugene, 4th ed. Edition: Univ. of Oregon Press.
- Westphal, V., Rollins, A. M., et al. (2002). "**Correction of geometric and refractive image distortions in optical coherence tomography applying Fermat's principle**", *Optics Express* **10**(9): 397-404.
- Wilson, J. D. and Foster, T. H. (2005). "**Mie theory interpretations of light scattering from intact cells**", *Optics Letters* **30**(18): 2442-2444.

- Wolf, E. and Li, Y. (1981). "**Conditions for the Validity of the Debye Integral-Representation of Focused Fields**", Optics Communications **39**(4): 205-210.
- Wright, A. J., Burns, D., et al. (2005). "**Exploration of the optimisation algorithms used in the implementation of adaptive optics in confocal and multiphoton microscopy**", Microscopy Research and Technique **67**(1): 36-44.
- Wyant, J. C. (1974). "**White-Light Extended Source Shearing Interferometer**", Applied Optics **13**(1): 200-202.
- Zerucha, T., Stuhmer, T., et al. (2000). "**A highly conserved enhancer in the Dlx5/Dlx6 intergenic region is the site of cross-regulatory interactions between Dlx genes in the embryonic forebrain**", Journal of Neuroscience **20**(2): 709-721.
- Zhu, J. J., Esteban, J. A., et al. (2000). "**Postnatal synaptic potentiation: Delivery of GluR4-containing AMPA receptors by spontaneous activity**", Nature Neuroscience **3**(11): 1098-1106.
- Zhu, L. J., Sun, P. C., et al. (1999a). "**Adaptive control of a micromachined continuous-membrane deformable mirror for aberration compensation**", Applied Optics **38**(1): 168-176.
- Zhu, L. J., Sun, P. C., et al. (1999b). "**Aberration-free dynamic focusing with a multichannel micromachined membrane deformable mirror**", Applied Optics **38**(25): 5350-5354.
- Zipfel, W. R., Williams, R. M., et al. (2003). "**Nonlinear magic: multiphoton microscopy in the biosciences**", Nature Biotechnology **21**(11): 1368-1376.

Acknowledgement

I want to express my gratitude to all people who shared the time with me during my time at the Max Planck Institute for medical research. A special thanks goes to **Prof. Winfried Denk** who guided me through my work with excellent advice. In particular, the discussions about physics were always a pleasure and opened very often a new way of thinking.

I appreciate it very much that **Prof. Josef Bille** agreed to act as a referee for my dissertation and disputation and I am also grateful to **Prof. Andreas Wolf** and **Prof. Iring Bender** for appraising the disputation.

Whenever I had to organize something **Christa Hörner-Ehm and the people from the administration** could help me and saved much of my time.

During my time as a PhD student I received very much help from **Marcus Feierabend** and **Marcel Lauterbach**. Marcus explained to me all relevant things to get started with my work and Marcus & Marcel were an enrichment not only in discussions about physics but also in social aspects.

Since I was not very skilled in biological preparations I want to thank all who helped me with my biological experiments: **Andy Migala, Monika Reichert, Maz Hasan, Stephan Meyer, Annemarie Scherbarth and Guenter Giese**. In particular, **Julia Mack-Bucher** helped me with her excellent experience with zebrafish by solving my open questions related to biology.

For questions regarding computer, electronic or mechanical problems **Michael Müller, Jürgen Tritthart and Manfred Hauswirth (and his colleagues)** had always open ears for me.

To all my lab mates **Dorine Keusters, Bernd Kuhn, Patrick Theer, Ingo Janke, Jens Dübel, Juergen Sawinski, Horatiu Fantana, Thomas Euler, Xavier Castell, Kevin Briggman and Philipp Hennig**, thank you for sharing the time with me.

Only one I have forgotten: my girlfriend **Susanne Hausselt**. She always supported me in hard times as a PhD student. Thanks to her cannot be expressed adequately.

